

“For small erections may be finished by their first architects; grand ones, true ones, ever leave the copingstone to posterity. Heaven keep me from ever completing anything. This whole book is but a draught, nay, but the draught of a draught. Oh, Time, Strength, Cash, and Patience!”

Herman Melville (Moby Dick)

**The bimolecular reactivity of gas
phase dications**

Dominic Jude Anthony Kearney

University College London

Thesis submitted for Degree of Doctor of Philosophy

2004

UMI Number: U592074

All rights reserved

INFORMATION TO ALL USERS

The quality of this reproduction is dependent upon the quality of the copy submitted.

In the unlikely event that the author did not send a complete manuscript and there are missing pages, these will be noted. Also, if material had to be removed, a note will indicate the deletion.



UMI U592074

Published by ProQuest LLC 2013. Copyright in the Dissertation held by the Author.
Microform Edition © ProQuest LLC.

All rights reserved. This work is protected against
unauthorized copying under Title 17, United States Code.



ProQuest LLC
789 East Eisenhower Parkway
P.O. Box 1346
Ann Arbor, MI 48106-1346

Publications from this thesis

Natalie Lambert, **D. Kearney**, Nikolas Kaltsoyannis and Stephen D. Price, 'The bond-forming reactions of atomic dications with neutral molecules: Formation of ArNH^+ and ArN^+ from collisions of Ar^{2+} with NH_3 ', *J. Am. Chem. Soc.*, 2004, **126**, p3658

D. Kearney and S. D. Price, 'Bond-forming and electron transfer reactions following collisions of CF_2^{2+} with H_2X ($\text{X} = \text{O}, \text{S}$)', *Phys. Chem. Chem. Phys.*, 2003, **5**, p1575

Acknowledgements

I would like to thank Alice. This thesis is as much hers as it is mine. I would also like to thank my supervisor Steve, my brother Gordon and the EPSRC for funding.

Abstract

This thesis reports the results of experiments investigating the reactivity of gas phase dications in collisions with neutral molecules at collision energies between 1 eV and 14 eV in the laboratory frame using crossed beam techniques. Product ion intensities are measured using time of flight mass spectrometry and integral reaction cross sections are extracted from raw data for the various reaction channels. Also contained within this thesis are details of the experimental apparatus and data reduction methods along with relevant theoretical aspects of the reactions.

The collision system $\text{CF}_n^{2+} + \text{H}_2\text{X}$ ($n = 1, 2$ and $\text{X} = \text{S}, \text{O}$) is shown to exhibit both dissociative and non-dissociative electron transfer reactivity which is examined using a model based on the Landau-Zener theory. Previously unobserved bond forming reactions are also observed. Mechanisms, involving a sequential process of adduct formation, charge separation and fragmentation, are proposed for these bond forming reactions.

The collision system $\text{Ar}^{2+} + \text{NH}_3$ exhibits both electron transfer and bond forming reactivity. Again, electron transfer reactivity is rationalised using the Landau-Zener theory. A mechanism is proposed for this previously unobserved bond forming reaction.

Contents

Publications	3
Acknowledgements	4
Abstract	5
Chapter 1 Introduction	9
1.1 Molecular dications, a brief history	9
1.2 Stability of molecular dications	11
1.3 Dication formation	16
1.4 Studying the character of isolated molecular dications	18
1.4.1 Ion-ion and photoion-photoion coincidence spectroscopy	18
1.4.2 Photoelectron-photoion-photoion coincidence spectroscopy	20
1.4.3 Doppler free kinetic energy release spectroscopy	22
1.4.4 Threshold photoelectron coincidence spectroscopy	23
1.5 Studying the bimolecular reactivity of dications	24
1.5.1 Experimental techniques to study the reactivity of dications	24
1.5.2 Guided ion beams	24
1.5.3 Crossed beam experiments	26
1.6 Review of collisions between dications and neutrals	26
1.7 Overview of work presented in this thesis	30
1.8 References	31
Chapter 2 Experimental	37
2.1 Overview	37
2.2 Detailed description	39
2.2.1 Generation of cations	39
2.2.2 Dication beam selection	41
2.2.3 Dication beam deceleration	44
2.2.4 Product ion mass analysis	46
2.2.5 Product ion detection	51
2.2.6 Time of flight measurement	52
2.2.7 Single collision conditions	54
2.2.8 Channeltron ion counter	58
2.3 Operational parameters	59
2.4 Conclusions	59
2.5 References	60

Chapter 3 Data reduction	61
3.1 Introduction	61
3.2 Data analysis	61
3.2.1 Determination of R_{obs}	61
3.2.2 Determination of integral reaction cross section σ'	63
3.2.3 Determination of c	70
3.3 Conclusions	74
3.4 References	75
Chapter 4 A theoretical perspective	76
4.1 Introduction	76
4.2 Reaction window model based on the Landau-Zener theory	76
4.3 Centre of mass frame	81
4.4 Collision cross section	84
4.5 Reaction cross section	86
4.6 Scattering	88
4.7 Conclusions	88
4.8 References	89
Chapter 5 $\text{CF}_2^{2+} + \text{H}_2\text{X}$ ($\text{X}=\text{O}, \text{S}$)	90
5.1 Introduction	90
5.2 Results	91
5.2.1 Assignment of product ions	91
5.2.2 CF_2^{2+} and H_2O	92
5.2.3 $\text{CF}_2^{2+} + \text{H}_2\text{S}$	93
5.3 Determination of integral reaction cross sections	94
5.4 Bond forming reactions	105
5.5 Conclusions	107
5.6 References	108
Chapter 6 $\text{CF}_3^{2+} + \text{H}_2\text{X}$ ($\text{X} = \text{O}, \text{S}$)	110
6.1 Introduction	110
6.2 Results	112
6.2.1 Ion identities	112
6.2.2 $\text{CF}_3^{2+} + \text{H}_2\text{O}$	112
6.2.3 $\text{CF}_3^{2+} + \text{H}_2\text{S}$	114
6.3 Determination of integral cross sections	115

6.4 Discussion	121
6.4.1 Landau-Zener calculations	121
6.4.2 Formation of CF_n^+ from $\text{CF}_3^{2+} + \text{H}_2\text{O}$	127
6.4.3 Formation of H_2O^+ fragments from $\text{CF}_3^{2+} + \text{H}_2\text{O}$	129
6.4.4 Formation of CF_n^+ from $\text{CF}_3^{2+} + \text{H}_2\text{S}$	130
6.4.5 Formation of H_2S^+ fragments from $\text{CF}_3^{2+} + \text{H}_2\text{S}$	132
6.4.6 Bond forming reaction	133
6.4.7 Neutral loss	136
6.5 Conclusions	137
6.6 References	138
Chapter 7 $\text{Ar}^{2+} + \text{NH}_3$	140
7.1 Introduction	140
7.2 Electron transfer reactivity results and discussion	141
7.2.1 Electron transfer reactivity	142
7.3 Bond forming reactions results and discussion	154
7.3.1 Computational results	157
7.4 Conclusions	161
7.5 References	163
Chapter 8 Further Work	166
References	167
Appendix	168

Chapter 1

Introduction

1.1 Molecular dications, a brief history

This thesis describes experiments performed to study the reactions which occur between doubly charged positive ions (dications) and neutral molecules in the gas phase. The majority of the work described here is concerned with reactions of small molecular dications reacting with small neutral molecules, although some work has also been carried out on atomic dications.

Molecular dications, being highly energetic species due to the two like charges in close proximity, possess very different properties to corresponding monocations.^{1,2}

In solution, dications, such as $\text{Ca}(\text{H}_2\text{O})_6^{2+}$, may be stabilised by solvation effects of the liquid. However, in the gas phase, no such stabilisation occurs. In isolation, because of the two like charges present within the ion, gas phase molecular dications commonly decay via unimolecular dissociation to form two singly charged fragments. Therefore, molecular dications in the gas phase often possess lifetimes which make effective study very difficult. As a result, information regarding their characteristics is sparse compared to that of monocations. However, there have been a number of research groups investigating the properties of such dicationic species and the amount of research being carried out has increased steadily over the last few years.³⁻¹⁸ This increase in research has been fuelled, in part, by the fact that the properties of gas phase dications, long thought to be of no real interest outside the specialised field of ion chemistry, have been shown to be important in other areas of physical chemistry.¹⁹⁻²¹ For example, it is thought that double ionisation of small molecules can play an important role in reactions occurring in the ionosphere of

some planets, including earth.²² Also, the advance in experimental and theoretical techniques has made possible the study of these short lived species.^{10,23-36}

The first recorded observation of a molecular dication was in the 1930s, when CO^{2+} was detected by mass spectrometry.³⁷ However, from then until the 1980s, dications were not considered of scientific importance, being more of a curiosity than worthy of investigation in their own right. So, while much progress was made in understanding the properties and reactivity of monocations, no real work was carried out on dicationic species. However, in the 1980s several experimental and theoretical groups began to investigate the properties of molecular dications.³⁸⁻⁴³ This work was, at first, mainly concerned with the structure, stability and lifetimes of dications in isolation. For example, it has been shown that O_2^{2+} has a deep potential well which may support many vibrational levels.⁴⁴⁻⁴⁶ Also, CO^{2+} , when trapped in a storage ring, can live for longer than one second.⁴ Theoretical studies have shown that the molecular dication CF_3^{2+} , previously calculated to possess a highly symmetric planar structure of D_{3h} symmetry,⁴⁷ in fact possesses C_{2v} symmetry.^{40,42} More recently, experiments have been performed to investigate the bimolecular reactivity, that is interactions with other species, of molecular dications. These experiments usually involved collisions at high energy, in the keV range.⁴⁸⁻⁵⁶ Later, experiments were carried out to investigate reactions between dications and neutral species at low collision energy, in the eV range.^{57,58} These low energy experiments have resulted in the detection of bond forming complexes.⁵⁹⁻⁶¹ Theoretical calculations are often performed to complement these experimental studies.^{61,62} As a result of these experiments, a much clearer picture has emerged, of the properties of molecular dications in low lying electronic states.

In this thesis, Chapters Two, Three and Four discuss the experimental and theoretical approach used to probe the bimolecular reactivity of dications at low collision energy. Chapters Five, Six and Seven describe the results of experiments carried out on the bimolecular reactivity of dications.

In order to understand the reactions described in this thesis, it is necessary to understand the stability of molecular dications and how the variation in their lifetimes arises. The next section in this chapter explains how certain electronic states of some molecular dications may possess an energy barrier to charge separation and so have lifetimes on a timescale which will allow isolation of the dication for crossed beam experiments to be performed.

1.2 Stability of molecular dications

Most molecular dications are thermodynamically unstable with respect to dissociation to two monocations. Therefore, as one would expect, most molecular dications immediately fragment to form two positively charged ions.⁶³ The stability of a molecular dication depends on the relative positions of two potential energy surfaces, one representing a purely repulsive state and the other representing an attractive state.

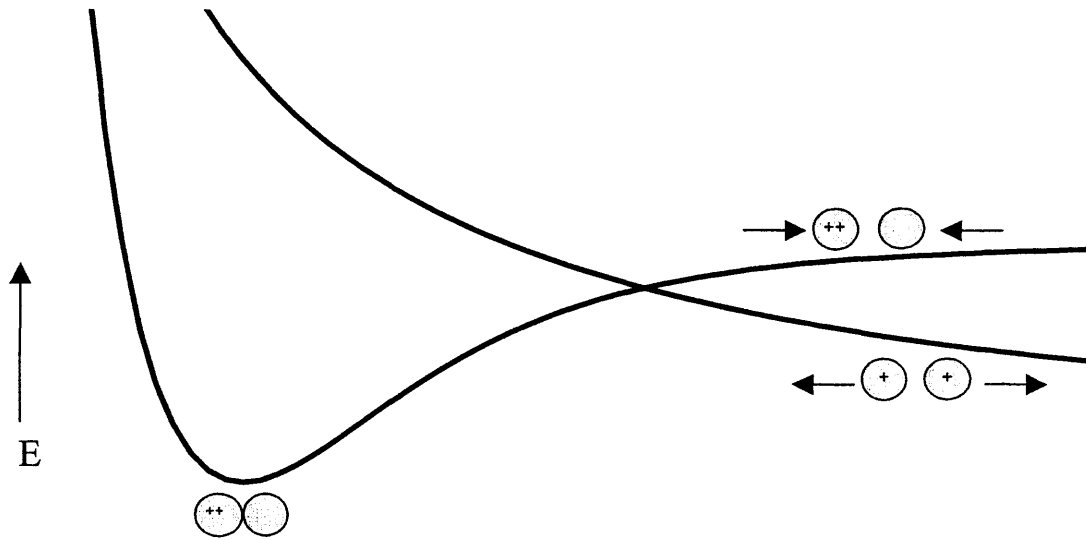


Figure 1.1a A schematic potential energy curves for a stable diatomic molecular dication.

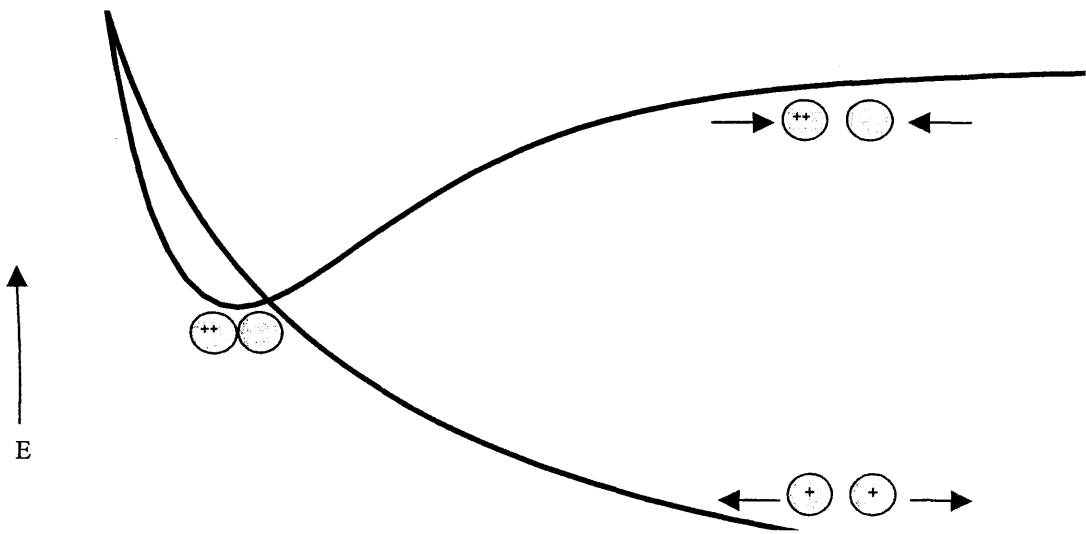


Figure 1.1b A schematic potential energy curves for an unstable diatomic molecular dication.

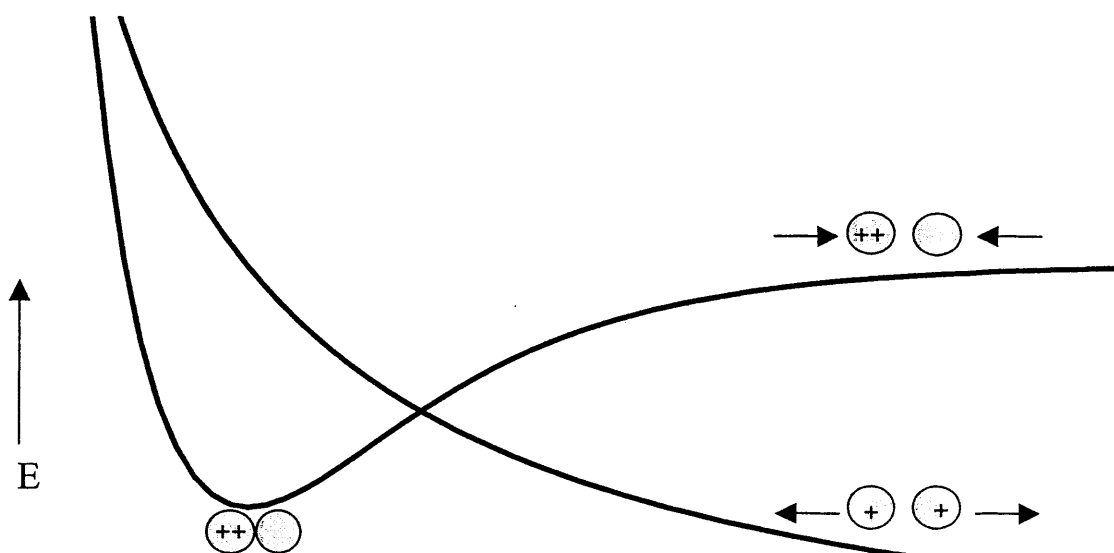


Figure 1.1c A Schematic potential energy curves for a metastable diatomic molecular dication.

Figure 1.1 shows three scenarios for a hypothetical molecular dication. As mentioned, the stability of a molecular dication depends on the relative energetic positions of the diabatic potential energy surfaces corresponding to the doubly charged fragment and neutral fragment (attractive state), and the two singly charged fragments (repulsive state). Figure 1.1a shows a thermodynamically stable dication where the dication lies lower in energy than the asymptote for charge separation. In this situation, only very high vibrational levels of the bound molecular dication may undergo curve crossing to the dissociative state. Conversely, figure 1.1b shows a thermodynamically unstable dication. In this situation, the asymptote for charge separation lies well below the energy of the dication. In addition, the position at which the dissociative potential energy surface crosses the potential energy surface for the associative state is such that predissociation may occur for very low vibrational levels, making the dication unstable. Figure 1.1c illustrates a case where the asymptote for charge separation (dissociation) lies energetically below the energy of the dication. However, the crossing point of the two potential energy surfaces is in a position where only higher vibrational levels of the dication may cross over to the

dissociative surface. This scenario illustrated in Figure 1.1c yields a metastable state where the bound state of the dication lies energetically above the charge separation asymptote but there exists, a barrier to charge separation.

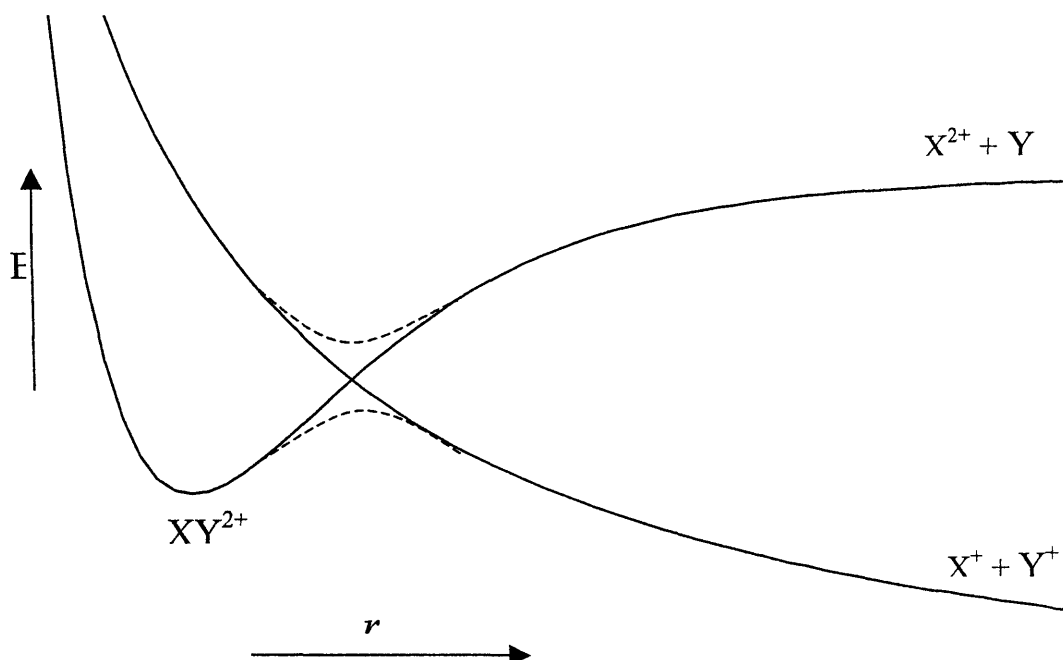


Figure 1.2 Schematic representation of how a metastable dication state may arise as a result of the avoided crossing (dashed line) between two potential energy curves

The form of the potential energy surface for a metastable dication is thought to arise as a result of an avoided crossing between these two potential energy surfaces (Figure 1.2). Again, the first surface corresponds to a state converging at large interspecies separation to a dicationic fragment and a neutral fragment ($X^{2+} + Y$) and the second surface corresponds to a purely repulsive state, converging at large interspecies separation to two monocations ($X^{+} + Y^{+}$). Figure 1.3 shows the adiabatic potential energy surface, resulting from the avoided crossing illustrated in Figure 1.2, with an energy barrier to charge separation.

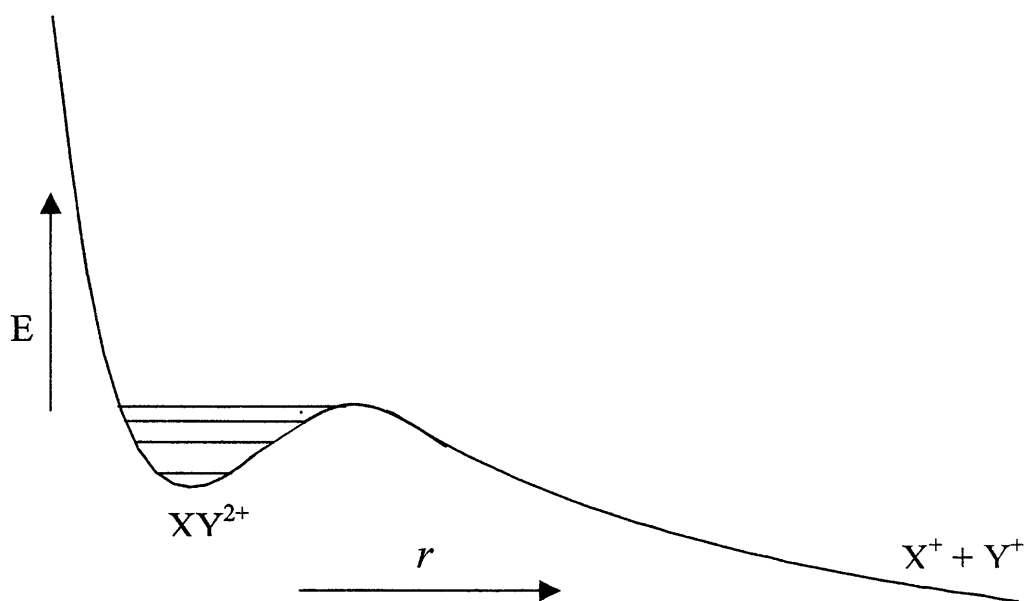


Figure 1.3 The metastable state of a dication which arises as a result of an avoided crossing.

In all cases of dicationic dissociation, the two singly charged fragments depart with a considerable release of kinetic energy due to the Coulombic repulsion of the two positive charges. The kinetic energy released in such a charge separation is usually of the order of 7 eV (675 kJmol^{-1}).

Unstable molecular dications have life-times in the sub nanosecond range and are too short lived to be isolated.^{32,64} However, dications such as CO^{2+} have been observed using mass spectrometry where the ions must exist for longer than $1 \mu\text{s}$ in order to be detected. Therefore, as discussed above, some molecular dications must possess at least one metastable state, which is sufficiently long-lived for the dication to be detected. The potential well of such metastable molecular dications may be of sufficient depth to support many vibrational levels.⁴⁵ The lifetime of a metastable dication will depend heavily on the degree of vibrational excitation it possesses. Higher vibrational states of a metastable dication may tunnel through the barrier to charge separation whereas dications in lower vibrational levels will be trapped in the potential well. Storage ring experiments have shown that low lying vibrational states of some dications may exist for more than 1s.⁴ As the charge separation portion of

the metastable dication's potential energy surface varies approximately with r^{-1} , the barrier to charge separation becomes wide at large values of r and low vibrational excitation.

Another explanation for the metastability of molecular dications has been proposed by Senekowitsch *et al.*⁶⁵ They suggest that the potential energy of F_2^{2+} may be explained by taking the chemical binding potential of the isoelectronic O_2 and simply adding a Coulomb repulsion potential. They also suggest that a metastable state will arise if the chemical binding potential is sufficient to overcome the Coulomb repulsion between the two positive charges. This theory holds as a result of the similarities in the electronic structure of F_2^{2+} and O_2 . However, this theory is not sufficient to explain the existence of some metastable dications such as HCl^{2+} where both charges are on the same atom.¹⁵

1.3 Dication formation

Dications can be formed by double ionisation of a suitable precursor gas. For example, two electrons may be removed from CF_4 to form CF_4^{2+} . However, CF_4^{2+} is an unstable ion and quickly fragments to yield, among other products, CF_2^{2+} and CF_3^{2+} . Double ionisation of a precursor gas may be achieved by electron impact ionisation. Electron impact ionisation involves bombarding the precursor gas with electrons of sufficiently high energy to remove two electrons from the neutral species.

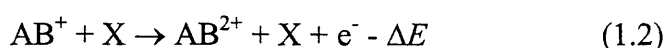


where X may be a molecule or atom. This double ionisation process occurs on a timescale where the reaction $X \rightarrow X^{2+}$ proceeds via a vertical transition. Therefore, if

a particular dication is not accessible via a vertical transition from a corresponding neutral, it will be difficult to form using electron impact ionisation.

Electron impact ionisation often produces ions in excited electronic states and, in the case of molecular product ions, with a broad distribution of vibrational energies.

Doubly charged ions may also be formed by charge stripping.² Charge stripping involves an electron being removed from a monocation, to form a dication, during a collision with a neutral. This mechanism takes the form



where ΔE is the kinetic energy of the projectile, AB^+ , required for ionisation to form AB^{2+} . The translational energy spectrum of the doubly charged product, AB^{2+} , gives the energy required for the process



If the incident beam consists of AB^+ in a variety of vibronic states, a series of peaks will be present in the translational energy spectrum of AB^{2+} , each corresponding to a different value of ΔE .

The charge stripping method yields the difference between the first and second ionisation energies of a molecule, AB . Therefore, a value for the single ionisation energy of a molecule, $AB \rightarrow AB^+$ must be determined by some other method such as photoelectron spectroscopy. The vertical ionisation energy of CS^+ going to CS^{2+} has been measured, by charge stripping, to be 22.0 ± 0.9 eV.⁶⁶ This measured ionisation energy is in good agreement with the value of 21.3 eV calculated using *ab initio* techniques.⁶⁶

Another method for double ionisation is photoionisation. Photoionisation is usually achieved with a laser,^{67,68} a discharge lamp^{9,30-32} or using synchrotron radiation^{33,34,69} and takes the form



Photoionisation using a He discharge yields more doubly charged species than electron impact with electrons of corresponding energy.³⁰ Also, by knowing the energy of the incident photon, the energy deposition in the target molecule is better quantified than for Electron Impact ionisation.

1.4 Studying the character of isolated molecular dications

The properties of molecular dications may be investigated using a variety of techniques. Most of these techniques usually involve formation of short lived molecular dications followed by the detection of the dissociation products in coincidence using time of flight mass spectrometry. These coincidence experiments can reveal information on the double ionisation process and on the electronic structure of the dication. This section gives a brief account of some of these coincidence techniques.

1.4.1 Ion-ion and photoion-photoion coincidence spectroscopy

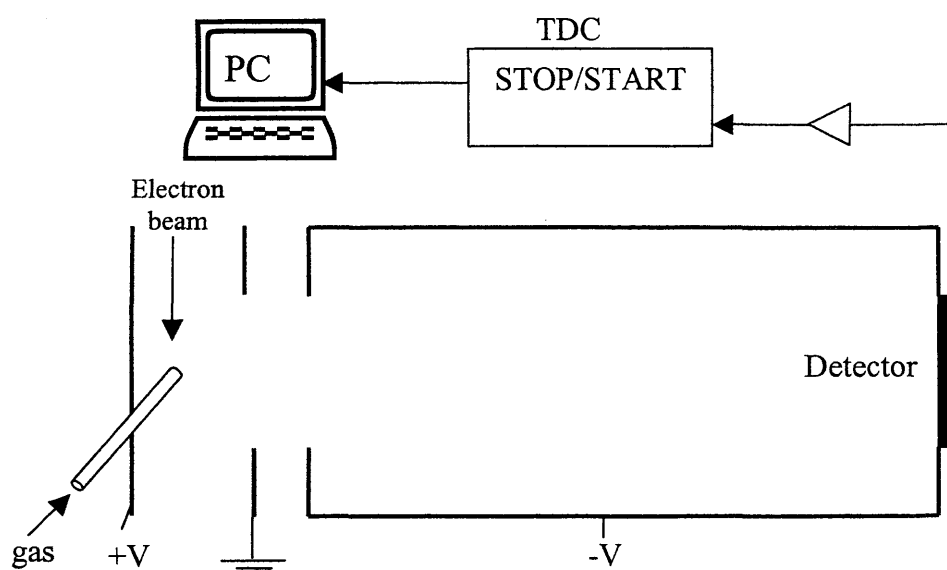
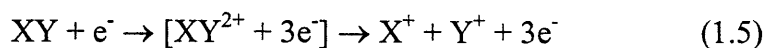
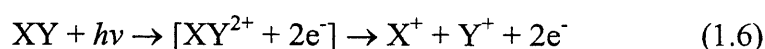


Figure 1.4. A diagram of an ion-ion coincidence spectrometer.⁷⁰

Ion-ion coincidence spectroscopy measures the difference in flight times of two singly charged ion fragments using time of flight mass spectrometry.⁷⁰⁻⁷² The ions are formed by electron impact ionisation in the case of ion-ion coincidence spectroscopy (Figure 1.4), and the process is usually of the form



In photoion- photoion coincidence spectroscopy, doubly charged ions are formed by photoionisation.^{31,73,74} The process usually takes the form



By measuring the difference in flight times of the two fragments X^+ and Y^+ formed from dissociative double ionisation, the kinetic energy release of the process may be determined. By detecting X^+ and Y^+ in coincidence, it is possible to distinguish between these ions formed from a double ionisation event and the equivalent ions formed as a result of single ionisation as the ions X^+ and Y^+ are formed from the same double ionisation event.

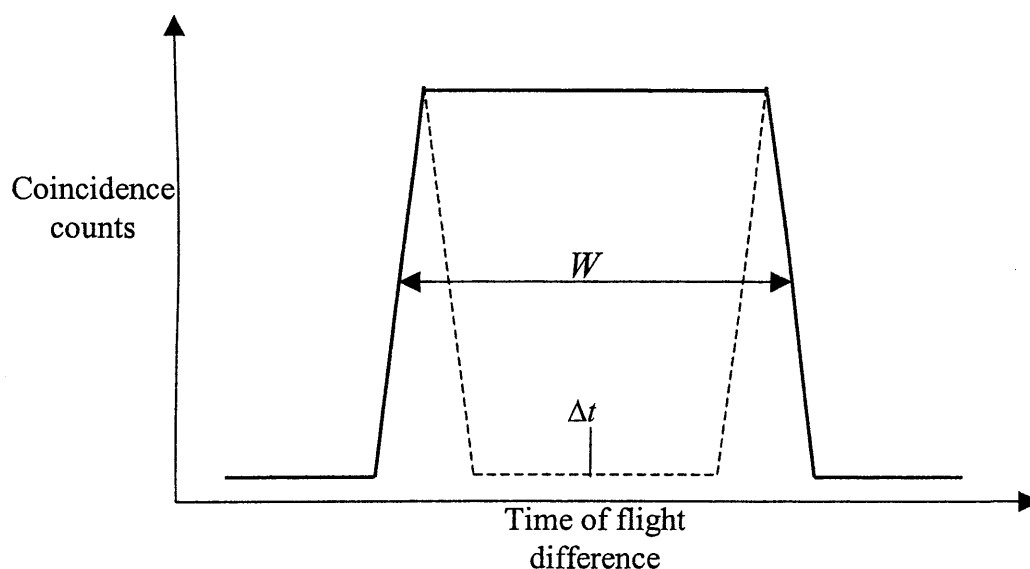


Figure 1.5. A schematic representation of an ion- ion coincidence spectrum. The dashed line is the peak shape expected under high angular discrimination.

Figure 1.5 shows a peak due to coincidences of a pair of ions. The peak is centred about a time of flight difference Δt , which is the time of flight difference the ions would have if they were formed with no initial kinetic energy. As the time of flight of an ion is proportional to the square root of the ion mass, Δt is proportional to the difference between the square roots of the ion masses. The kinetic energy release experienced by the two monocations during dication dissociation may be determined from the width of the coincidence peak W . The width of the coincidence peak arises as a result of the direction, with respect to the axis of the spectrometer, of the initial impulse imparted onto each product monocation during dication dissociation. The dashed line in figure 1.5 shows the expected peak shape under high angular discrimination.

1.4.2 Photoelectron-photoion-photoion coincidence spectroscopy

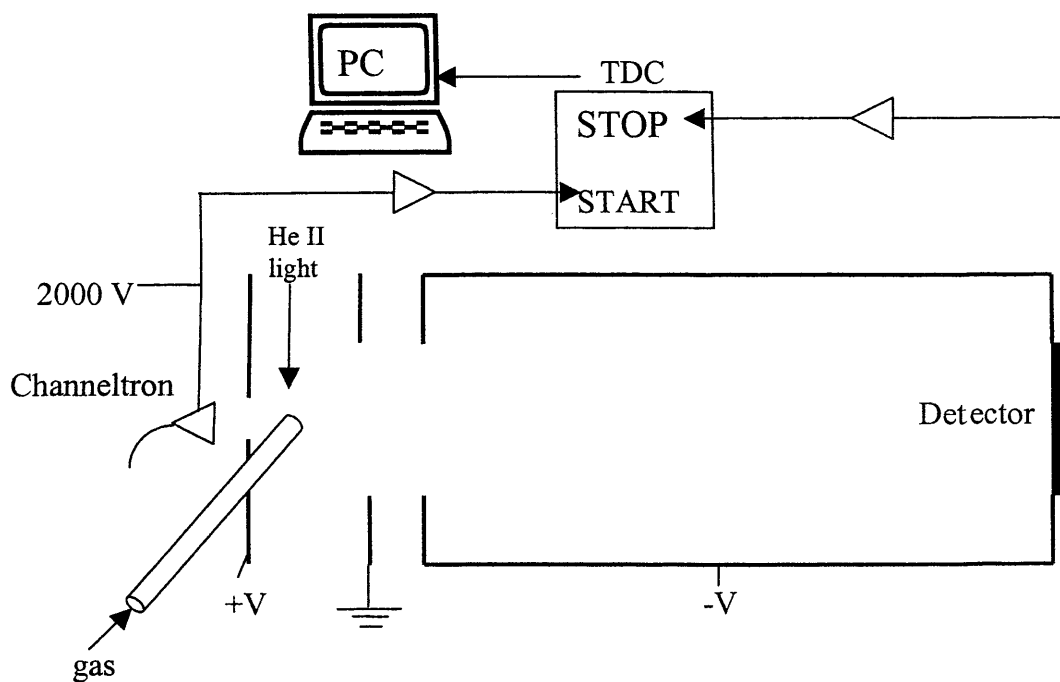


Figure 1.6. A typical design of a photoelectron-photoion-photoion coincidence spectrometer

Photoelectron-photoion-photoion coincidence spectroscopy (PEPIPICO) involves detecting three charged particles in coincidence.^{75,76} A photoelectron, ejected as a result of a double ionisation event is detected along with two singly charged ions formed from the unimolecular dissociation of a molecular dication in a dissociative state. A typical design of a PEPIPICO apparatus is shown in figure 1.6. This apparatus uses a time of flight mass spectrometer (TOFMS) based on the Wiley McLaren⁷⁷ two field design. The detection of a photoelectron, ejected on photoionisation, gives the START signal for the time of flight. The detection of a photoion gives the STOP signal. By detecting the photoelectron, the exact time of dication formation may be determined allowing the absolute flight times of the ion fragments to be determined accurately. By measuring the flight times of each ion, PEPIPICO allows the distinction between two different dissociation channels where pairs of ions are the same mass. For example, in previous studies on the double ionisation of SO₂ using PIPICO, the fragmentation channels



could not be distinguished from the fragmentation channel



The lack of distinction between fragmentation channels arises because PIPICO only yields information regarding the difference in flight times of two ions detected in coincidence. However, since the differences in flight times for the two product ions shown in equations (1.7) and (1.8) are both zero, these channels cannot be differentiated using PIPICO. Using PEPIPICO, it has been shown that SO₂²⁺ fragmenting to O₂⁺ + S⁺ is the dominant dissociation channel compared to SO₂²⁺ dissociating to yield O⁺ + O⁺ + S.

1.4.3 Doppler Free Kinetic Energy Release Spectroscopy⁷⁸

Techniques, which measure the kinetic energy release upon fragmentation of doubly charged ions, such as those described above, give little information regarding dissociation channels due to poor resolution caused by Doppler broadening in the kinetic energy distribution of the fragments.

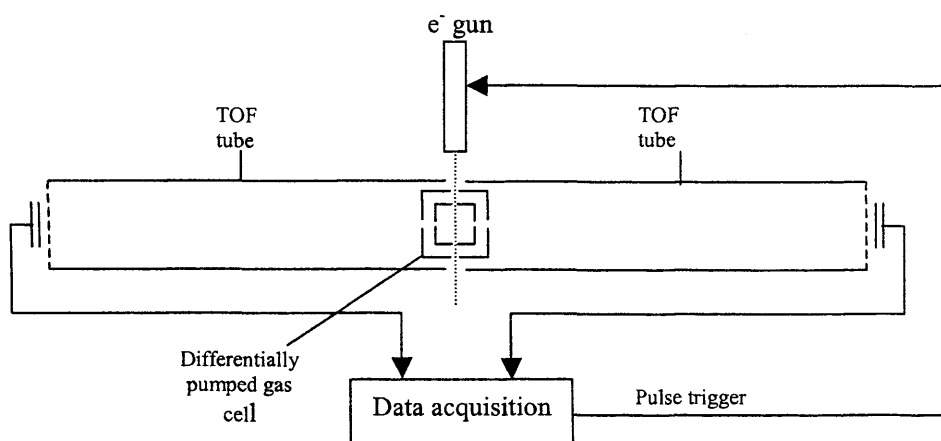


Figure 1.7. Experimental set-up for DFKERS. Two TOF tubes allows energies of the two dissociation products to be measured independently but in coincidence.

These previous coincidence techniques use only one channel for energy analysis and the second pulse simply as a coincidence requirement. For example, CO^{2+} dissociating with a kinetic energy release of 8 eV produces two ions with kinetic energies of 4.57 eV and 3.43 eV. The line broadening caused by the Doppler effect at 293 K is 0.73 eV. By eliminating this Doppler broadening, higher resolution spectra may be acquired. Energy measurements are achieved by using two separate time of flight tubes and detecting both fragments independently but in coincidence as shown in figure 1.7.

By measuring the energies of both dissociation fragments, the centre of mass kinetic energy may be eliminated. The kinetic energy release of a dication AB^{2+} dissociating to A^+ and B^+ is then given by

$$E = E_A + E_B - \frac{[\sqrt{E_A m_A} - \sqrt{E_B m_B}]^2}{m_A + m_B} \quad (1.9)$$

where E_A and E_B are the kinetic energies of the monocations fragments A^+ and B^+ and m_A and m_B are their masses.

1.4.4 Threshold Photoelectrons Coincidence Spectroscopy⁷⁹

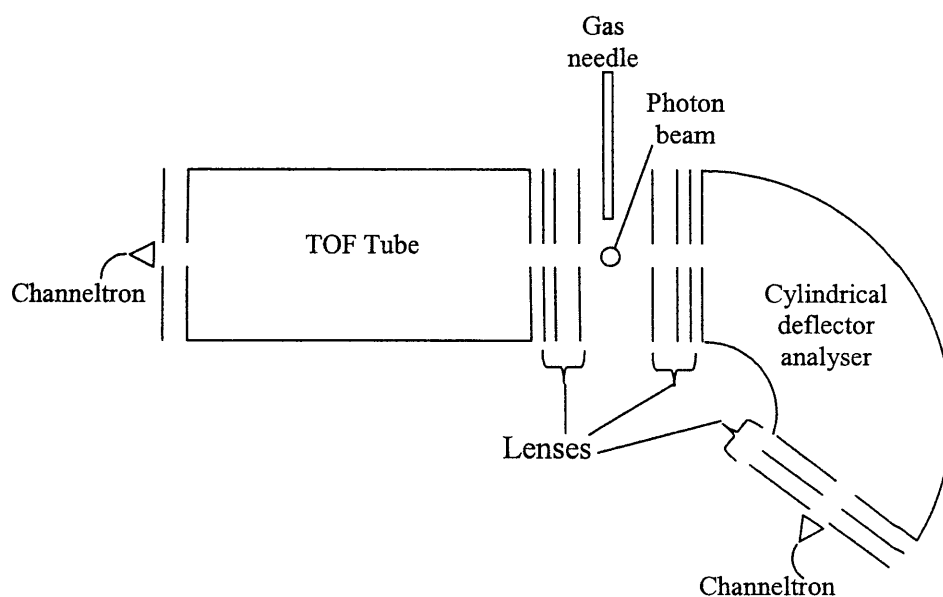


Figure 1.8. A threshold photoelectron coincidence spectrometer.

Threshold photoelectrons coincidence spectroscopy (TPEsCO) involves detecting two, essentially zero energy, photoelectrons in coincidence. These photoelectrons are ejected from the molecule as the energy of the scanned ionising photon goes through the threshold of a vibronic state of a particular dication. The experimental apparatus used by Hall *et al.*⁸⁰ is shown in figure 1.8. This experiment uses a time of flight mass spectrometer coupled with a cylindrical deflector analyser. The electrical fields in the ion-molecule interaction region are such that, at threshold, the electron intensity is divided between the two analysers. The photoelectrons are detected within a few meV of their formation. A TPEsCO spectrum is able to resolve vibrational levels of a particular electronic state of a molecular dication and can offer

much information about the vibrational structure. For example, vibrational constants may be determined as well as accurate values for double ionisation potentials.

1.5 Studying the bimolecular reactivity of dications

1.5.1 Experimental techniques to study the reactivity of dications

As mentioned, molecular dications are usually short-lived species. Therefore, if the reactivity between these dications and other species is to be studied, experiments are limited to investigating relatively long-lived states. It is necessary to manipulate these dications effectively in order to study collisions. One of the most effective methods of manipulating ions is with guided ion beams.

1.5.2 Guided ion beams

Ions are formed by some ionisation method such as electron impact or photoionisation. Dications are isolated and inhomogeneous electric fields are used to confine, focus and transport the ions. Ion guides such as octapoles may guide the ions as well as serve as a collision cell. These electric fields may be used to accelerate or decelerate the ions to the required collision energy before encounters with the collision partner. By varying the collision energy of the ion beam, a picture of how the product ion yield varies with collision energy may be obtained. The product ions are then mass analysed by a quadrupole mass filter before they are detected.⁸¹

Ions in an electric field that changes rapidly, such as those generated by octapoles or quadrupoles, are held in a “pseudopotential” which is flat near the middle but rises steeply near the electrodes.⁸² By altering the frequency and amplitude of the alternating field, a pseudopotential well may be created whose depth is greater than

the kinetic energy of the ions within the electrode structure. An example of a quadrupole ion guide and the electric field created are shown in figure 1.9. Such ion guides are often used as the collision region for ion molecule reactions.^{81,83,84} If the well depth within the collision region of an ion-neutral collision experiment is greater than the kinetic energy release experienced by, say, coulombic explosion of a dissociating dication, all product ions will be trapped within the electric field and may be transported out of the ion guide and detected. By trapping and detecting all of the product ions, accurate total cross sections for ion- molecule reactions may be determined.

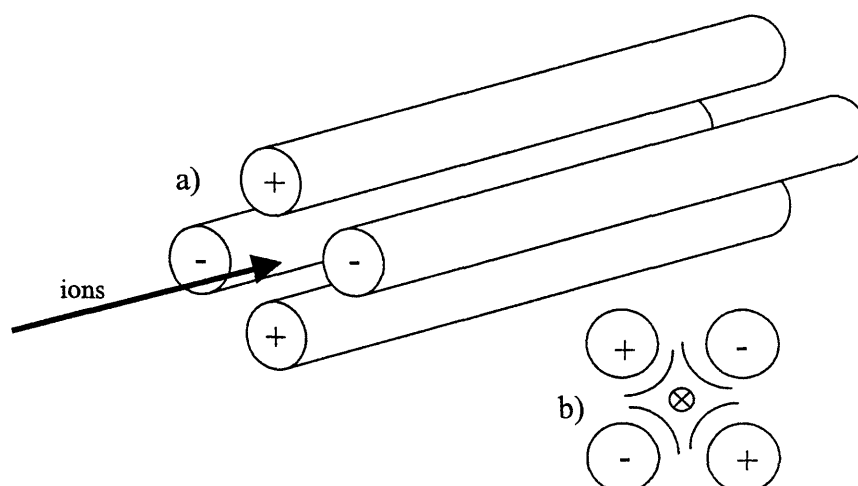


Figure 1.9 A quadrupole ion guide (a) and the electric field generated by the guide (b). Switching the potentials on the rods at high frequency (rf) creates a pseudopotential well in the centre along the axis of the ion guide.

Bassi and co-workers⁸¹ have used ion guide methodology to investigate ion-molecule reactions. They use electron impact ionisation to create ions. Selection of the primary ion beam is achieved by a 90° magnetic sector. The beam is then focused into an octapole radio frequency ion guide which is surrounded by a collision cell where they encounter the neutral collision partner. The ion guide focuses the product ions to a quadrupole mass analyser, after which they are detected by a conventional electron multiplier detector. This method has proved successful for

measuring the cross section of a particular ion-molecule reaction channel as a function of collision energy.

1.5.3 Crossed beam experiments

Ions are formed by electron impact, photon impact or charge stripping ionisation as described in section 1.3. The ions are collimated and the dication is isolated by some mass spectrometric technique such as a quadrupole mass filter⁴³ or velocity filter.⁵⁷ The pure dication beam is then decelerated to the required collision energy before intersecting, at right angle, the beam of the collision partner. Products formed as a result of these collisions are mass analysed, usually by a time of flight mass spectrometer or a quadrupole mass spectrometer, and detected.

Angularly resolved crossed beam experiments are achieved by rotating the detector about the collision point. By rotating the detector in this way, ion intensity may be determined as a function of angle.⁸⁵

Scattering angles may also be determined by using a position sensitive detector. In position sensitive coincidence spectroscopy, ions are detected in coincidence and the velocity vectors of the two detected ions are determined.⁸⁶ These velocity vectors allow information to be gained on the electronic states of the reacting species and the products formed. Details of reaction mechanisms may also be obtained in this way.

1.6 Review of collisions between dications and neutrals

The processes, which occur as a result of a collision between a dication and a neutral, depend heavily on the identity of the dication, the identity of the neutral, and the energy at which the collision occurs. It has been shown previously that these processes are of three main types.⁸⁷ The first, energy transfer, involves a proportion

of the collision energy being used in breaking chemical bonds. Energy transfer may be divided into two classes: collision induced charge separation (CICS), where some of the collision energy is used to overcome the energy barrier to charge separation in the dication



and collision induced neutral loss (CINL),^{88,89} where some of the collision energy is used to cause dication to dissociate to a dication and a neutral fragment.



The second type of process which may occur, as a result of a dication neutral collision, is electron transfer. That is a single electron moving from the neutral to the dication during the collision. Again, this type of process may be one of two classes. Non-dissociative electron transfer, where no fragmentation of the monocationic products occurs



Similarly, an electron may transfer with fragmentation of one or both of the monocationic products



The third type of bimolecular process is a chemical, or bond forming, reaction. A bond forming reaction involves formation or rearrangement of chemical bonds.



These bond-forming processes often have very small cross sections and usually only occur at very low collision energies. It is these bond-forming reactions which have prompted the study of low energy collisions described in this thesis.

As mentioned, early experiments investigating the properties of dications have concentrated on dications as isolated species. However, later experiments have been

performed to study the consequences of collisions between dications and neutral species. Early collision experiments were performed at high collision energies in conventional mass spectrometers. High energy collisions of atomic dications with neutrals^{90,91} and molecular dications with neutrals^{48,50,51,54,56} show electron transfer, from the neutral to the dication, and collision induced dissociation dominate. However, to investigate more chemically realistic situations, collisions were performed at much lower energies (< 100 eV). These low energy collisions again, showed electron transfer reactivity to dominate, with two singly charged products being formed.^{58,59,92} In the cases where one or both of the colliding species contain more than one atom, dissociative electron transfer, where the product monocations fragment soon after the reaction has occurred, was often observed. In 1986, bond-forming reactions were identified following collisions between transition metal dications and alkanes, for example^{93,94}



Later, the molecular oxygen dication was seen to react with NO to yield NO_2^+ and O^+ .⁹⁵ Chemical reactions between molecular dications and neutrals are now an active area for research. Bond forming reactions often have very small cross sections compared to electron transfer reactions, usually less than about 5%. An example of an early study of chemical reactivity is that carried out by Price and co-workers.⁹⁶ The bimolecular reactivity of 44 molecular dication/neutral collision systems revealed a large proportion to exhibit bond-forming reactivity. Following this study, many papers have been published reporting bond-forming reactions following collisions between molecular dications and neutral species.^{23,24,59,85,97,98} In particular, many examples of the formation of a doubly charged adduct following collisions

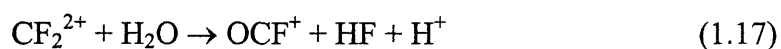
between both atomic dications with neutrals and molecular dications with neutrals have been reported.^{83,84}

For example



As well as adducts being formed, bond formation may occur as a result of direct abstraction of an atom from one colliding species to another. Hydride transfer has been reported following collisions between CF_2^{2+} and H_2 (D_2) forming HCF_2^+ (DCF_2^+).^{24,98} Following these hydride abstraction studies, work was carried out on the effects of isotopes on the product ion yields. For example, intermolecular isotope effects where CF_2^{2+} was collided with H_2 and D_2 ²⁴ and intramolecular isotope effects, where CF_2^{2+} was collided with HD .⁹⁹ Collisions of CF_2^{2+} with HD showed a strong preference for the formation of DCF_2^+ over HCF^+ . Statistical effects accounted for this preference.

Angularly resolved studies, where the post collision scattering angles are determined, have shown electron transfer to be dominated by forward scattering of the monocations derived from the dication.⁸⁵ Scattering experiments carried out by Mrazek *et al.*⁸⁵ have provided mechanistic details of the reactions of $\text{CO}_2^{2+} + \text{D}_2$ for both bond forming and electron transfer processes. Angularly resolved experiments have also been carried out using coincidence techniques.⁸⁶ These experiments allow knowledge of exactly which ionic products are formed together, by detecting products in coincidence. From these experiments, mechanisms of reactions have been determined. For example, it has been shown that the process



proceeds via charge separation, losing H^+ , then neutral loss of HF in a sequential mechanism.¹⁰⁰ These findings have been confirmed by *ab initio* calculations.⁶² By

determining the velocity vectors of the product ions in the centre of mass frame, details have been obtained regarding the electronic states of the reactant dications.

1.7 Overview of work presented in this thesis

This thesis describes the results of experiments, carried out on a crossed beam apparatus, to study the reactions which occur when dications collide with neutral molecules. In previous experiments, CF_2^{2+} colliding with H_2 was seen to yield the product ion HCF_2^+ .²⁴ This reaction was thought to involve the abstraction of a hydride ion H^- by the dication. Here, experiments have been performed to replicate previous experiments where we replace H^- with OH^- . Therefore, CF_2^{2+} has been studied in collisions with H_2O .⁵⁹ Following these experiments, which reveal a new bond forming process, forming OCF^+ , H_2O was replaced with H_2S and, later, CF_2^{2+} was replaced with CF_3^{2+} . It will be shown that the formation of OCF^+ and SCF^+ do not proceed via a direct abstraction of the relevant anion but instead involve a more complicated mechanism with complex formation, bond rearrangement and fragmentation of the adduct. Finally, in an attempt to find further bond forming processes, the reaction $\text{Ar}^{2+} + \text{NH}_3$ has been studied.⁶⁰ This is shown to possess interesting bond forming reactivity where two products are detected, one a fragment of the other.

Contained within the first part of this thesis, are detailed descriptions of experimental procedures, data reduction methods and theoretical background. The later section of this thesis contains details of results obtained along with conclusions drawn from those results.

1.8 References

- 1 M. Larsson, *Com. Atom. Molec. Phys.* **29** (1993) 39
- 2 D. Mathur, *Phys. Rep.* **225** (1993) 193-272
- 3 S. Hsieh and J. H. D. Eland, *J. Chem. Phys.* **103** (1995) 1006-1012
- 4 L. H. Andersen, J. H. Posthumus, O. Vahtras, H. Agren, N. Elander, A. Nunez, A. Scrinzi, M. Natiello and M. Larsson, *Phys. Rev. Lett.* **71** (1993) 1812-1815
- 5 M. Hochlaf, R. I. Hall, F. Penent, H. Kjeldsen, P. Lablanquie, M. Lavollee and J. H. D. Eland, *Chem. Phys.* **207** (1996) 159-165
- 6 D. Mathur, L. H. Andersen, P. Hvelplund, D. Kella and C. P. Safvan, *J. Phys. B-Atom. Molec. Opt. Phys.* **28** (1995) 3415-3426
- 7 L. E. Dejarne, R. G. Cooks and T. Ast, *Org. Mass Spectrom.* **27** (1992) 667-676
- 8 P. G. Fournier, J. H. D. Eland, P. Millie, S. Svensson, S. D. Price, J. Fournier, G. Comtet, B. Wannberg, L. Karlsson, P. Baltzer, A. Kaddouri and U. Gelius, *J. Chem. Phys.* **89** (1988) 3553-3564
- 9 S. Leach, J. H. D. Eland and S. D. Price, *J. Phys. Chem.* **93** (1989) 7583-7593
- 10 M. Lundqvist, D. Edvardsson, P. Baltzer, M. Larsson and B. Wannberg, *J. Phys. B-Atom. Molec. Opt. Phys.* **29** (1996) 499-514
- 11 R. I. Hall, L. Avaldi, G. Dawber, A. G. McConkey, M. A. Macdonald and G. C. King, *Chem. Phys.* **187** (1994) 125-135
- 12 A. S. Mullin, D. M. Szaflarski, K. Yokoyama, G. Gerber and W. C. Lineberger, *J. Chem. Phys.* **96** (1992) 3636-3648
- 13 S. D. Price, Y. Y. Lee, M. Manning and S. R. Leone, *Chem. Phys.* **190** (1995) 123-130
- 14 J. C. Severs, W. J. Griffiths, F. M. Harris, S. R. Andrews and D. E. Parry, *J. Chem. Soc.-Faraday Trans.* **92** (1996) 3293-3298
- 15 F. R. Bennett and I. R. McNab, *Chem. Phys. Lett.* **251** (1996) 405-412
- 16 P. A. Hatherly, M. Stankiewicz, L. J. Frasinski, K. Codling and M. A. Macdonald, *Chem. Phys. Lett.* **159** (1989) 355-360
- 17 T. Weiske, W. Koch and H. Schwarz, *J. Am. Chem. Soc.* **115** (1993) 6312-6316

- 18 W. Koch, B. Liu, T. Weiske, C. B. Lebrilla, T. Drewello and H. Schwarz, *Chem. Phys. Lett.* **142** (1987) 147-152
- 19 S. Leach, *J. Electron Spec. Rel. Phenom.* **41** (1986) 427
- 20 A. Leger and L. d'Hendecourt, *Astron. Astrophys.* **146** (1985) 81
- 21 L. J. Allamandola, A. Tielens, G and J. R. Barker, *J. Astrophys.* **290** (1985) L25
- 22 S. Prasad and D. R. Furman, *J. Geophys. Res.* **80** (1975) 1360
- 23 Z. Dolejssek, M. Farnik and Z. Herman, *Chem. Phys. Lett.* **235** (1995) 99-104
- 24 K. A. Newson and S. D. Price, *Chem. Phys. Lett.* **269** (1997) 93-98
- 25 S. D. Price, S. A. Rogers and S. R. Leone, *J. Chem. Phys.* **98** (1993) 9455-9465
- 26 H. R. Koslowski, H. Lebius, V. Staemmler, R. Fink, K. Wiesemann and B. A. Huber, *J. Phys. B-Atom. Molec. Opt. Phys.* **24** (1991) 5023-5034
- 27 J. D. C. Jones, A. S. M. Raouf, D. G. Lister, K. Birkenshaw and N. D. Twiddy, *Chem. Phys. Lett.* **78** (1980) 75
- 28 X. D. Zhou, A. D. Shukla, R. E. Tosh and J. H. Futrell, *Int. J. Mass Spectrom. Ion Proc.* **160** (1997) 49
- 29 A. Ehbrecht, N. Mustafa, C. Ottinger and Z. Herman, *J. Chem. Phys.* **105** (1996) 9833-9846
- 30 B. P. Tsai and J. H. D. Eland, *I. J. Mass Spectrom. Ion Proc.* **36** (1980) 143
- 31 D. M. Curtis and J. H. D. Eland, *Int. J. Mass Spectrom. Ion Proc.* **63** (1985) 241-264
- 32 J. H. D. Eland, *Chem. Phys. Lett.* **203** (1993) 353-362
- 33 P. Millie, I. Nenner, P. Archirel, P. Lablanquie, P. Fournier and J. H. D. Eland, *J. Chem. Phys.* **84** (1986) 1259-1269
- 34 E. Ruhl, S. D. Price and S. Leach, *J. Phys. Chem.* **93** (1989) 6312-6321
- 35 T. Masuoka and I. Koyano, *J. Chem. Phys.* **95** (1991) 909-917
- 36 E. Y. Kamber, K. Akgungor, C. P. Safvan and D. Mathur, *Chem. Phys. Lett.* **258** (1996) 336-341
- 37 R. Conrad, *Physik. Z.* **31** (1930) 888

- 38 J. Hrusak, Z. Herman and S. Iwata, *Int. J. Mass Spectrom.* **192** (1999) 165-171
- 39 J. Hrusak, Z. Herman, N. Sandig and W. Koch, *Int. J. Mass Spectrom.* **201** (2000) 269-275
- 40 J. Hrusak, N. Sandig and W. Koch, *Int. J. Mass Spectrom.* **187** (1999) 701-706
- 41 N. Kaltsoyannis and S. D. Price, *Chem. Phys. Lett.* **313** (1999) 679-684
- 42 N. Tafadar, N. Kaltsoyannis and S. D. Price, *Int. J. Mass Spectrom.* **192** (1999) 205-214
- 43 S. A. Rogers, S. D. Price and S. R. Leone, *J. Chem. Phys.* **98** (1993) 280-289
- 44 M. Larsson, P. Baltzer, S. Svensson, B. Wannberg, N. Martensson, A. N. Debrito, N. Correia, M. P. Keane, M. Carlssongothe and L. Karlsson, *J. Phys. B-Atom. Molec. Opt. Phys.* **23** (1990) 1175-1195
- 45 R. I. Hall, G. Dawber, A. Mcconkey, M. A. Macdonald and G. C. King, *Phys. Rev. Lett.* **68** (1992) 2751-2754
- 46 G. Parlant, J. Senekowitsch, S. V. Oneil and D. R. Yarkony, *J. Chem. Phys.* **94** (1991) 7208-7211
- 47 J. M. De La Vega and E. San Fabian, *Int. J. Quant. Chem.* **52** (1994) 947
- 48 Z. Herman, P. Jonathan, A. G. Brenton and J. H. Beynon, *Chem. Phys. Lett.* **141** (1987) 433-442
- 49 C. J. Reid, F. M. Harris and J. H. Beynon, *Int. J. Mass Spectrom. Ion Processes.* **82** (1988) 151-162
- 50 C. J. Reid, J. A. Ballantine and F. M. Harris, *Int. J. Mass Spectrom. Ion Processes.* **93** (1989) 23-47
- 51 D. Mathur, R. G. Kingston, F. M. Harris, A. G. Brenton and J. H. Beynon, *J. Phys. B-Atom. Molec. Opt. Phys.* **20** (1987) 1811-1822
- 52 V. Krishnamurthi, K. Nagesha, V. R. Marathe and D. Mathur, *Phys. Rev. A.* **44** (1991) 5460-5467
- 53 J. M. Curtis and R. K. Boyd, *J. Chem. Phys.* **80** (1984) 1150-1161
- 54 K. Vekey, A. G. Brenton and J. H. Beynon, *J. Phys. Chem.* **90** (1986) 3569-3577

- 55 M. Hamdan and A. G. Brenton, *J. Phys. B-Atom. Molec. Opt. Phys.* **22** (1989) L 45-1 50
- 56 R. Susic, L. Lu, D. E. Riederer, D. Zigon, R. G. Cooks and T. Ast, *Org. Mass Spectrom.* **27** (1992) 769-776
- 57 S. D. Price, *J. Chem. Soc. Faraday Trans.* **93** (1997) 2451-2460
- 58 Z. Herman, *Int. Rev. Phys. Chem.* **15** (1996) 299-324
- 59 D. Kearney and S. D. Price, *Phys. Chem. Chem. Phys.* **5** (2003) 1575-1583
- 60 N. Lambert, D. Kearney, N. Kaltsoyannis and S. D. Price, *J. Am. Chem. Soc.* **126** (2004) 3658-3663
- 61 D. Ascenzi, P. Franceschi, P. Tosi, D. Bassi, M. Kaczorowska and J. N. Harvey, *J. Chem. Phys.* **118** (2003) 2159-2163
- 62 N. Lambert, N. Kaltsoyannis and S. D. Price, *J. Chem. Phys.* **119** (2003) 1421-1425
- 63 P. Kush, A. Hustrulid and J. T. Tate, *phys. Rev.* **54** (1938) 1037
- 64 G. Roberts and A. H. Zewail, *J. Phys. Chem.* **95** (1986) 1259
- 65 J. Senekowitsch and S. Oneil, *J. Chem. Phys.* **95** (1991) 1847-1851
- 66 V. Krishnamurthi, M. Krishnamurthy, V. A. Mrarathe and J. Mathur, *J. Phys. B.* **25** (1992) 5149
- 67 B. Ernstberger, H. Krause, A. Kiermeier and H. J. JNeusser, *J. Chem. Phys.* **92** (1990) 5285
- 68 Z. Fang and V. H. S. Kwong, *Phys. Rev. A.* **55** (1997) 55
- 69 T. Masuka, *J. Chem. Phys.* **98** (1993) 6989
- 70 K. A. Newson and S. D. Price, *Int. J. Mass Spectrom. Ion Proc.* **153** (1996) 151-159
- 71 K. E. McCulloh, T. E. Sharp and H. M. Rosenstock, *J. Chem. Phys.* **42** (1965) 3501
- 72 B. Brehm and d. Frenes, *Int. J. Mass Spectrom. Ion Proc.* **26** (1978) 251
- 73 G. Dujardin, S. Leach, O. Dutuit, P. M. Guyon and M. Richardviard, *Chem. Phys.* **88** (1984) 339
- 74 N. J. Mason, *J. Chem. Phys.* **98** (1993) 1750-1751

- 75 L. J. Frasinski, M. Stankiewicz, K. J. Randall, P. A. Hatherly and K. Codling, *J. Phys. B-Atom. Molec. Opt. Phys.* **19** (1986) L819
- 76 J. H. D. Eland, F. S. Wort and R. N. Royds, *J. Electron Spec. Rel. Phenom.* **41** (1986) 297-309
- 77 W. C. Wiley and I. H. McLaren, *Rev. Sci. Instr.* **26** (1955) 1150
- 78 M. Lundqvist, P. Baltzer, D. Edvardsson, L. Karlsson and B. Wannberg, *Phys. Rev. Lett.* **75** (1995) 1058
- 79 A. G. McConkey, G. Dawber, L. Avaldi, M. A. Macdonald, G. C. King and R. I. Hall, *J. Phys. B-Atom. Molec. Opt. Phys.* **27** (1994) 271-282
- 80 R. Hall, A. McConkey, L. Avaldi, M. A. Macdonald and G. C. King, *J. Phys. B.* **25** (1992) 411
- 81 D. Bassi and P. Tosi, *J. Vac. Sci. Technol. A.* **16** (1998) 114-122
- 82 J. M. Farrar and W. H. Saunders, *Techniques for the study of ion-molecule reactions*, (1988)
- 83 P. Tosi, R. Correale, W. L. Lu, S. Falcinelli and D. Bassi, *Phys. Rev. Lett.* **82** (1999) 450-452
- 84 P. Tosi, W. Y. Lu, R. Correale and D. Bassi, *Chem. Phys. Lett.* **310** (1999) 180-182
- 85 L. Mrazek, J. Zabka, Z. Dolejssek, J. Hrusak and Z. Herman, *J. Phys. Chem. A.* **104** (2000) 7294-7303
- 86 W. P. Hu, S. M. Harper and S. D. Price, *Meas. Sci. Technol.* **13** (2002) 1512-1522
- 87 S. D. Price, *Phys. Chem. Chem. Phys.* **5** (2003) 1717
- 88 S. D. Price, M. Manning and S. R. Leone, *Chem. Phys. Lett.* **214** (1993) 553-558
- 89 Y. Y. Lee, S. R. Leone, P. H. Champkin, N. Kaltsoyannis and S. D. Price, *J. Chem. Phys.* **106** (1997) 7981-7994
- 90 B. Hird and S. P. Ali, *J. Phys. B-Atom. Molec. Opt. Phys.* **14** (1981) 267-280
- 91 U. Jellen-Wutte, J. Schweinzer, W. Vanek and H. Winter, *J. Phys. B-Atom. Molec. Opt. Phys.* **18** (1985) L779
- 92 N. Tafadar, D. Kearney and S. D. Price, *J. Chem. Phys.* **115** (2001) 8819
- 93 L. M. Roth and B. S. Freiser, *Mass Spectrom. Rev.* **10** (1991) 303-328

- 94 R. Tonkyn and J. C. Weisshaar, *J Am. Chem. Soc.* **108** (1986) 7128-7130
- 95 B. K. Chatterjee and R. Johnsen, *J. Chem. Phys.* **91** (1989) 1378-1379
- 96 S. D. Price, M. Manning and S. R. Leone, *J. Am. Chem. Soc.* **116** (1994) 8673-8680
- 97 P. B. Armentrout, *Acs Symposium Series.* **502** (1992) 194-209
- 98 Z. Herman, J. Zabka, Z. Dolejssek and M. Farnik, *Int. J. Mass Spectrom.* **192** (1999) 191-203
- 99 K. A. Newson and S. D. Price, *Chem. Phys. Lett.* **294** (1998) 223-228
- 100 S. M. Harper, W. P. Hu and S. D. Price, *J. Chem. Phys.* **121** (2004) Proof Copy

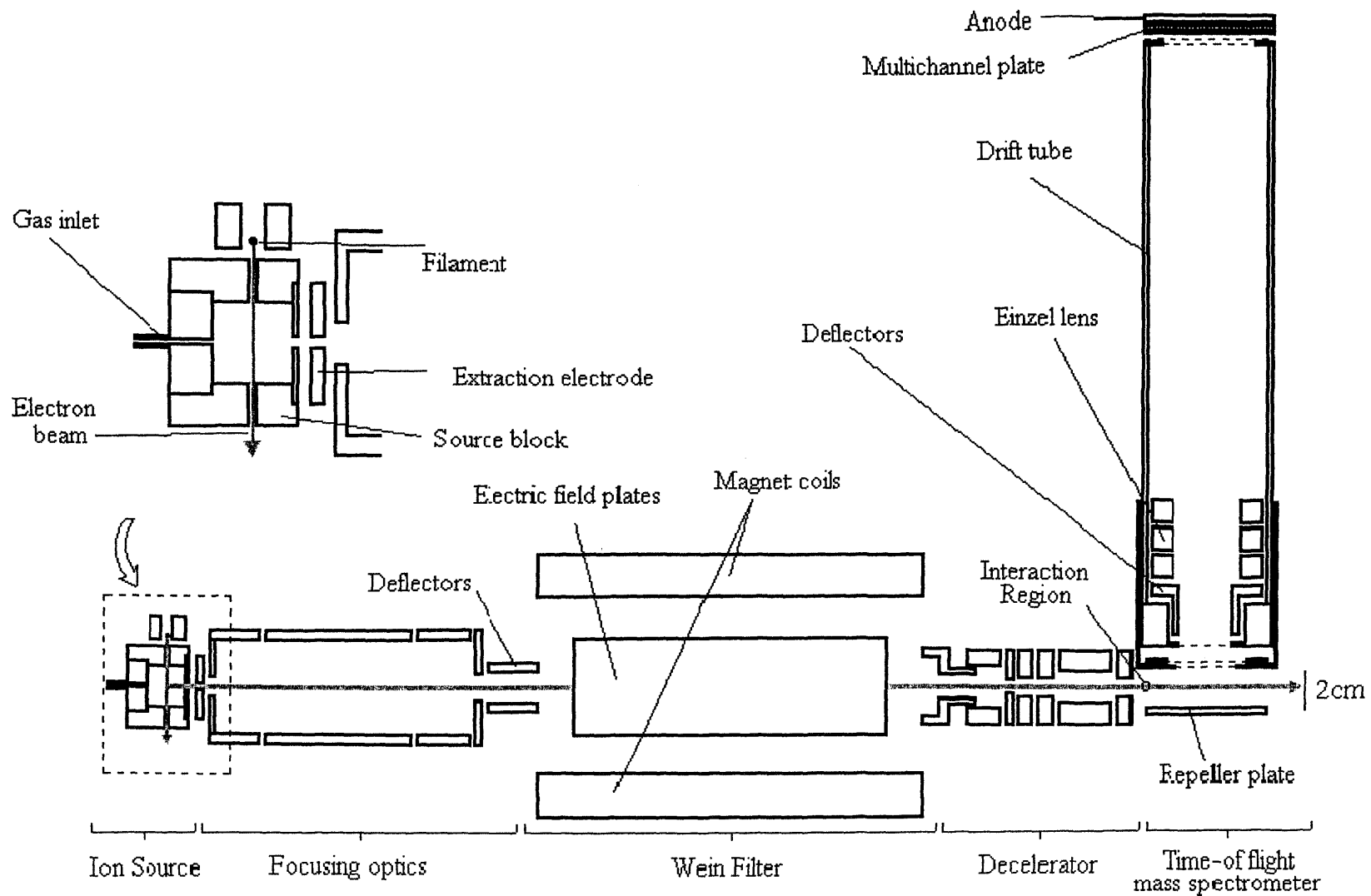
Chapter 2

Experimental

2.1 Overview

The object of this project is to study the reactivity of molecular dications with neutral molecules. To date, most work has concentrated on collisions at relatively high energies.¹⁻⁹ The work described in this report is concerned with much lower collision energies (<15 eV in the laboratory frame). At lower collision energies the colliding species should have more time for processes such as bond forming reactions to occur, as the interaction time will be longer, the interaction time being the amount of time that the collision partners are in close enough proximity for a reaction to take place. To this end, an instrument has been designed and built (figure 2.1) which allows crossed beam collision reactions to be carried out at low collision energies. This experiment uses electron-impact (EI) ionisation of a suitable precursor gas to produce a mixture of monocations and dications. These ions are then extracted from the source, focused and accelerated to form an isoenergetic beam. A velocity filter is employed to reject all but the dications of interest from the extracted beam. The dications are decelerated to the required collision energy before encounters with the neutral collision partner occur in the source region of a time of flight mass spectrometer (TOFMS). The TOFMS is used to identify and quantify the product ions produced in these collisions.

Figure 2.1 Experimental apparatus setup



2.2 Detailed description

2.2.1 Generation of cations

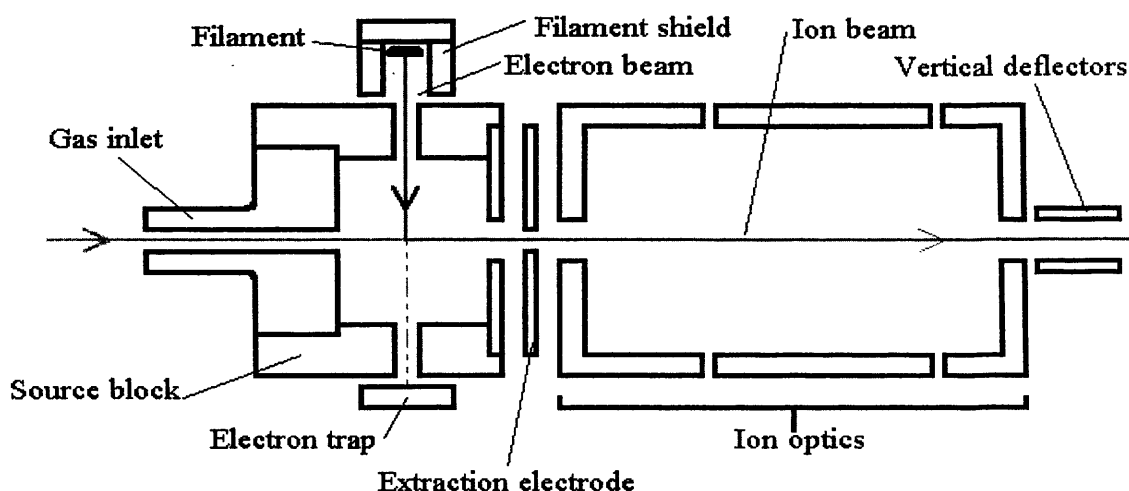


Figure 2.2 Electron impact ionisation source and focusing optics

The precursor gas, from which the dications are to be generated, is introduced into the EI source (figure 2.2). This EI source is of a stainless steel construction to withstand the harsh ionisation plasma created when the precursor gas is ionised. Ionisation is achieved using a beam of 100 eV electrons created by passing a 3.7 A current through a thermionic tungsten filament. A filament shield directs the electrons into the source block and an electron trap regulates the filament current so that a constant rate of ion production is maintained. The electron emission current generated is 10 μA . The resultant electron beam intersects a perpendicularly orientated jet of the precursor gas. This precursor gas reaches the source block via a PTFE tube. Newly formed ions are extracted from the ionisation source by an extraction electrode. The EI source is maintained at sufficiently high pressure for a good supply of ions to be achieved. However, the pressure is maintained low enough that collision-induced dissociation of the newly formed dications, caused by collisions with other species present in the ionisation source, is minimised. This pressure in the EI source is typically 4×10^{-6} mbar. In single collision conditions, the

number of desired dications formed is proportional to the precursor gas pressure inside the ionisation source. Indeed, a proportional increase in the dication current is observed as the ionisation source pressure is raised. However, there is a certain threshold above which the increase in dication current is not proportional to source pressure. At higher source pressures, collision induced dissociation of the newly formed dications within the EI source decreases the number of dications available for the collision experiment causing the dication yield to decrease as the pressure becomes sufficiently high to allow reactions such as



In addition to the reduction in dication current, collisions between the newly formed dications and other species present in the ionisation source may increase the number of other ions being formed within the ionisation source and so being extracted from the source. The likelihood of impurity ions passing through into the collision region and so contaminating the mass spectrum will therefore increase.

The electron beam passing through the source block is only a few millimetres in width. As a result, the ions formed in the narrow electron beam are all formed in the same region in the source block and so are formed at close to a uniform electrical potential. Therefore, the potential energy spread of the ion beam is only about 0.5 eV. This energy spread is determined by using one of the ion optics as a retarding field analyser.

The ions are all extracted to the same energy by the extraction electrode. If the ionising region were larger, the kinetic energy spread of the beam would be much greater. After extraction from the source by the extraction electrode to a kinetic energy of 200q eV, the ions are focused by a number of electrostatic optics and a

pair of vertical deflecting plates. These electrostatic optics serve to collimate the ion beam. The ions are then directed into the velocity filter.

2.2.2 Dication beam selection

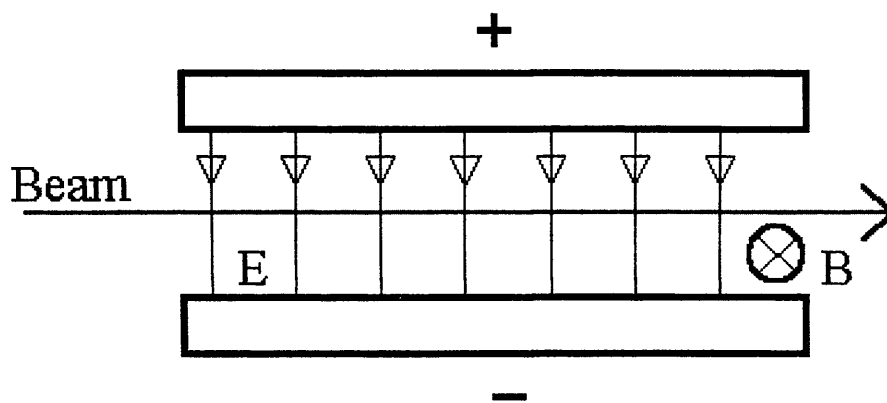


Figure 2.3a Electric field component of the velocity filter

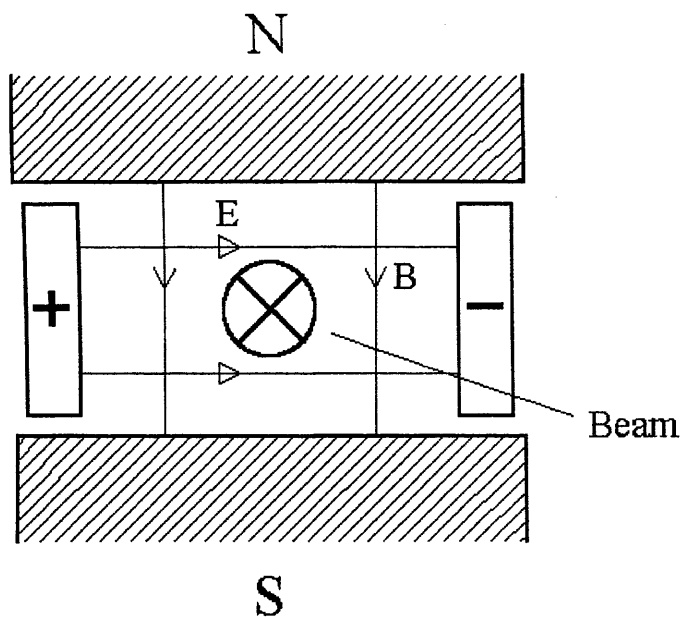


Figure 2.3b Magnetic field component of the velocity filter

The ion beam leaving the ionisation source region and passing through the various electrostatic optics is made up of a mixture of parent and fragment ions. These ions include monocations and dications derived from both the original precursor gas and any traces of impurity gases including, but not exclusively, N_2 , O_2 and CO_2 . In most

circumstances, the desired dication will account for only a small fraction of the total ion beam at this point. It is therefore necessary to extract the desired dications from this ion beam. A pure dication beam is vital to the success of this crossed beam experiment as many of the other ions formed within the EI source may well be indistinguishable from the product ions formed following collisions between the dications and neutral collision partners. A pure dication beam is achieved by means of a Colutron velocity filter¹⁰ based on the Wien filter.^{11,12} This velocity filter is made up of an electric field (E) (figure 2.3a) and a magnetic field (B) (figure 2.3b) set up perpendicularly to each other.

The force (F_E) acting on the ion due to the electric field is simply the product of the charge (q) and the field strength (E)

$$F_E = qE \quad (2.2)$$

This force acts in the direction of the electric field.

The force (F_B) acting on the ion as a result of the magnetic field is given by the product of the charge (q), the magnetic flux density (B) and the velocity (v) of the ion

$$F_B = Bqv \quad (2.3)$$

This force is perpendicular to the direction of the magnetic flux. These forces are opposed and any ion will be deflected out of the beam if the forces are not equal.

$$qE = Bqv \quad (2.4)$$

This equality of forces will occur for an ion velocity where

$$v = E / B \quad (2.5)$$

If all the ions are accelerated to the same energy by a uniform potential then

$$v = \sqrt{\left(\frac{2qV}{m}\right)} \quad (2.6)$$

$$\therefore \frac{E}{B} = \sqrt{\left(\frac{2qV}{m}\right)} \quad (2.7)$$

$$\text{and } m = \frac{2qVB^2}{E^2} \quad (2.8)$$

This shows that for certain values of B and E , any ion not of a given mass will be deflected out of the ion beam. For convenience, the magnetic field is kept constant and the electric field is varied as constant heating and cooling of the electromagnet may damage the magnet coils.

The natural focusing effects of these crossed electric and magnetic fields means that dications in the centre of the beam will be unaffected by the fields. However, dications towards the edges of the beam will be drawn to a central focal point beyond the velocity filter. Shim plates placed between the electrostatic plates compensate for this effect. The potential on these shim plates are biased with respect to the electrostatic plates potential and may be adjusted by a potentiometer. The overall effect is to make the electric field weaker at the positive electrostatic plate. The electric field shape produced compensates for the focusing properties of the velocity filter.

In previous experiments by other groups, mass selection of the dication beam has been achieved using a quadrapole mass spectrometer (QMS).¹³⁻¹⁶ A QMS is satisfactory for higher collision energies (>40 eV). However, the ions possess a transverse velocity while travelling through the QMS, caused by the oscillating electric field associated with quadrapole ion selection. The decelerating optic used in our experiments is only capable of decelerating the ions in the longitudinal direction. Therefore, if a QMS is used, ions will still possess a significant transverse velocity which will cause an unacceptably high divergence of the dication beam at our low

collision energies. The scope of this work is collision energies below 15 eV in the laboratory frame so the velocity filter described here is most appropriate.

2.2.3 Dication beam deceleration

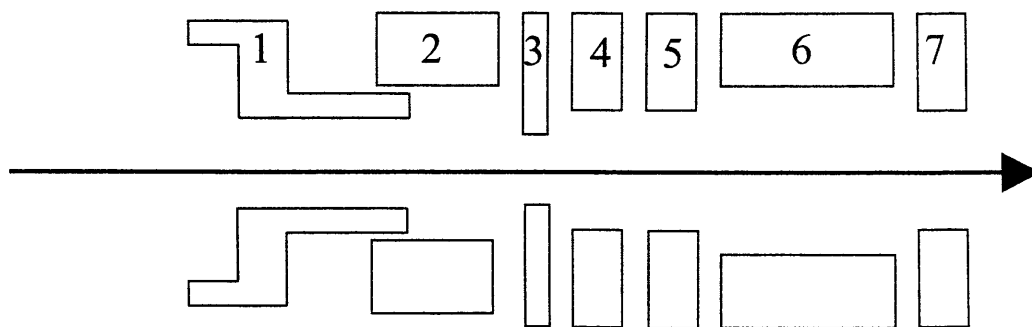


Figure 2.4 Decelerator optics

Molecular dications, being short-lived species, must be accelerated down the instrument to the interaction region as quickly as possible. On exiting the velocity filter, the pure dication beam possesses a relatively high kinetic energy. This kinetic energy of $200q$ eV must be reduced in order for the dications to collide with the neutral molecules at the required, low energy. The high energy with which the dications pass through, and then exit the velocity filter means that the dications reach the interaction region quickly. Dications are often very short-lived species with lifetimes of microseconds or even less. By accelerating the dications to a high velocity then decelerating them to the required collision energy, we reduce the transit time between formation and interaction with the neutral collision partner. By reducing the transit time, we minimise the number of dications lost as a result of unimolecular dissociation. The scope of these collision experiments is limited to low energy collision reactions. That is typically less than 15 eV in the laboratory frame. Therefore, the pure dication beam must be decelerated to the required collision energy before interactions take place.

The desired collision energy is set by a commercial decelerator (figure 2.4). This decelerator is made up of six focusing lenses (2-7) and a base (1). The first two (2 and 3) are maintained at the same potential as the beam (-200 V) while the third and fourth (4 and 5) are set to a lower potential which may be adjusted using potentiometers. The sixth lens (7) is set to ground. This gradual change in potential slows the beam down in a stepwise fashion. The deceleration process causes a high level of divergence of the beam because it is only able to reduce its longitudinal velocity. To rectify this beam divergence, an Einzel lens (6) is employed to refocus the ions before the encounter with their neutral collision partner. The Einzel lens is made of three electrically isolated cylinders. The two outer cylinders are held at ground potential and the inner cylinder is held at a higher potential. The potential on the inner cylinder may be adjusted using a potentiometer. By adjusting the potential on the centre cylinder, it is possible to vary the position of the focal point. Figures 2.5a and 2.5b show Simion¹⁷ diagrams of how an Einzel lens may focus ions.

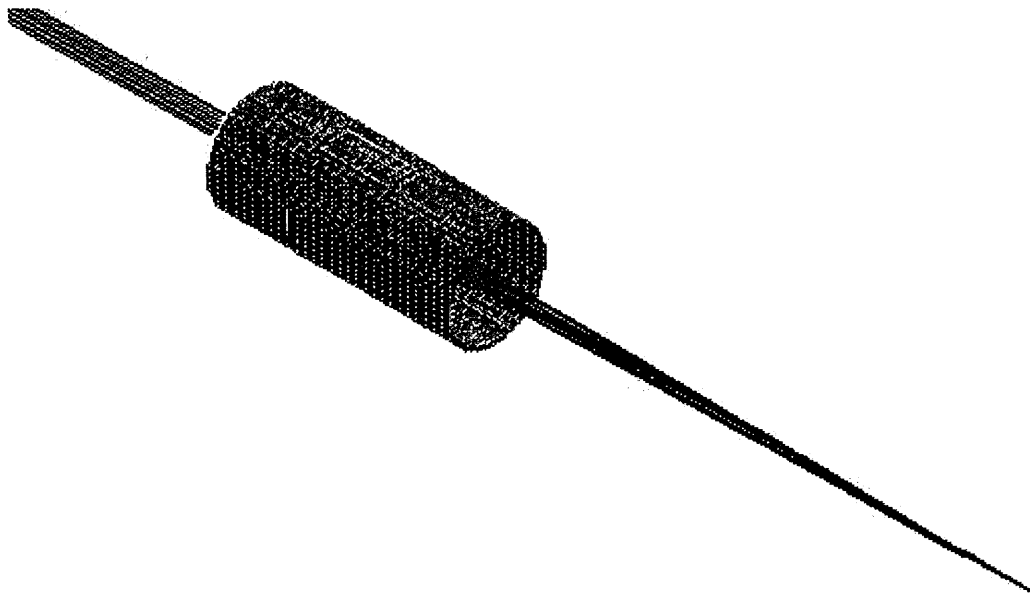


Figure 2.5a A Simion diagram of an Einzel lens.

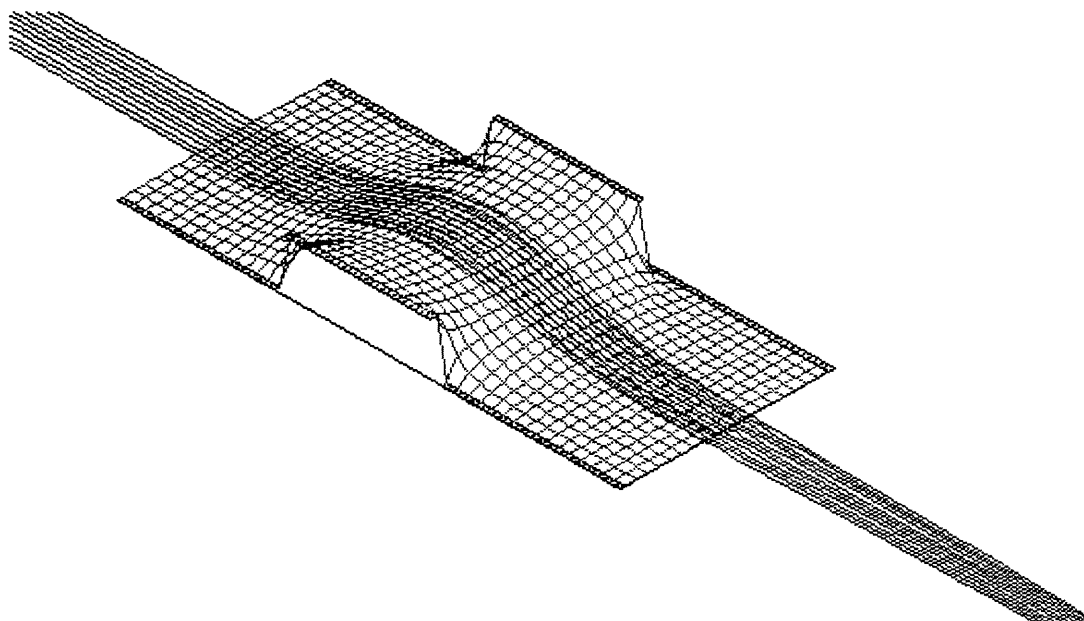


Figure 2.5b A Simion potential energy diagram of an Einzel lens. The “saddle” nature of the lens focuses the ions to a point.

2.2.4 Product ion mass analysis

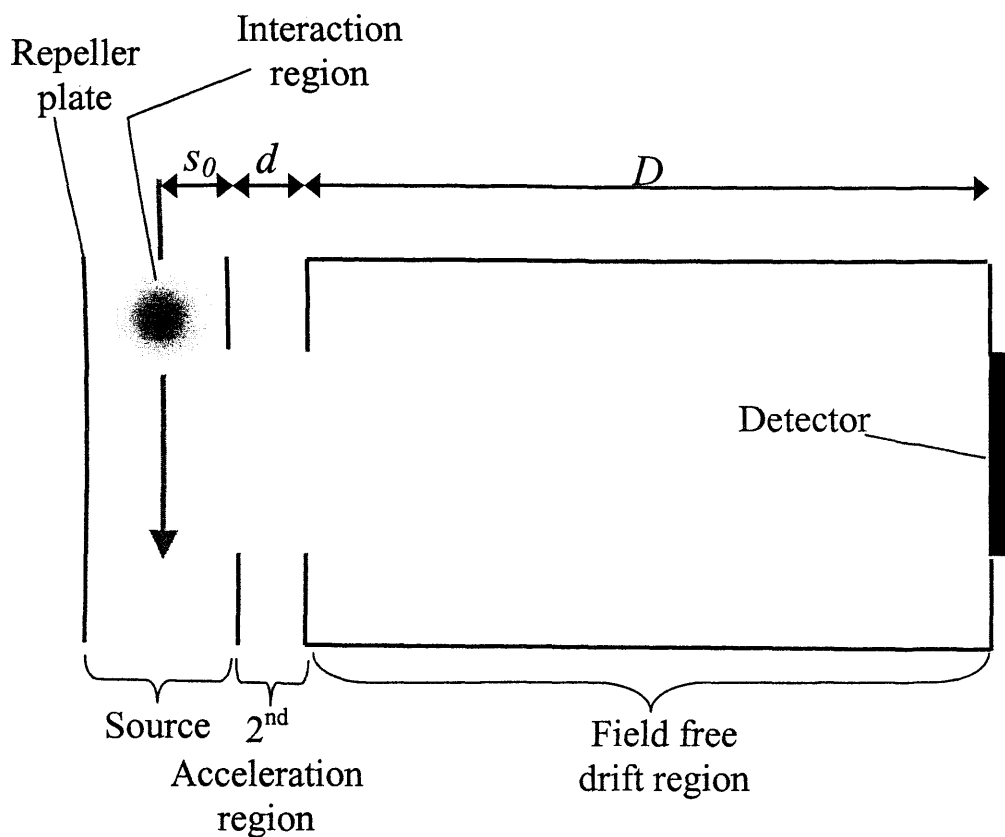


Figure 2.6 Time of flight mass analyser

Once the dication beam has been decelerated to the required collision energy by the decelerator assembly, the reactant dications enter the source region of the time of flight mass spectrometer (TOFMS) shown in figure 2.6. The TOFMS source region also serves as a collision region where dications and neutrals interact. The dication beam intersects an effusive jet of the neutral collision partner. Product ions formed as a result of these collisions, as well as unreacted dications are periodically extracted from the TOFMS source. Extraction from the source is achieved by pulsing a positive potential on a repeller plate (Figure 2.6). The ions are then accelerated through a second acceleration region before reaching the field free drift zone, after which they are detected.

Time of flight mass spectrometry relies on the principle that two ions of different masses, accelerated to the same kinetic energy, will possess different final velocities. This difference in their final velocities means that, over a given distance, their times of flight will be different. It is shown in the appendix of this thesis that, using simple electrostatics and Newtonian mechanics, the time of flight (τ_{tof}) of an ion of mass m in a series of electric fields is given by

$$\tau_{tof} = k\sqrt{m} + c \quad (2.9)$$

where k and c are constants. k relates to the internal dimensions of the mass spectrometer and the electric fields used. c relates to the electronic timing delays of the TOFMS.

In time of flight mass spectrometry, ions are all detected simultaneously allowing many complete mass spectra to be collected each second. In addition to this advantage over other types of mass spectrometry, time of flight mass spectrometry is a relatively simple technique which, unlike other types of mass spectrometry, does not require the fine alignment of expensive equipment.

The TOFMS used in the experiments described in this thesis is of a standard Wiley-McLaren¹⁸ two-field design with first order space focusing. The TOFMS source region is twice the length of the second acceleration region. As mentioned, collisions between the reactant dications and the neutral collision gas occur in the source region. Following these collisions, a repeller plate (figure 2.6) is periodically pulsed from 0 V to + 400 V at a frequency of 50 kHz. This pulse creates an electric field in the source region which extracts the collision product ions and any unreacted reactant dications out of the source region, through the second acceleration region where they are further accelerated, and into the field free drift zone. In the field free drift zone, ions possessing different masses, having different final velocities and so different flight times, separate out before impinging onto the MCP detector. The source region, the second acceleration region and the field free drift zone are assigned lengths of $2S_0$, d and D respectively.

As mentioned, the TOFMS employed in these crossed beam collision experiments possesses first order focusing properties. A brief outline of the general principle of this focusing follows.

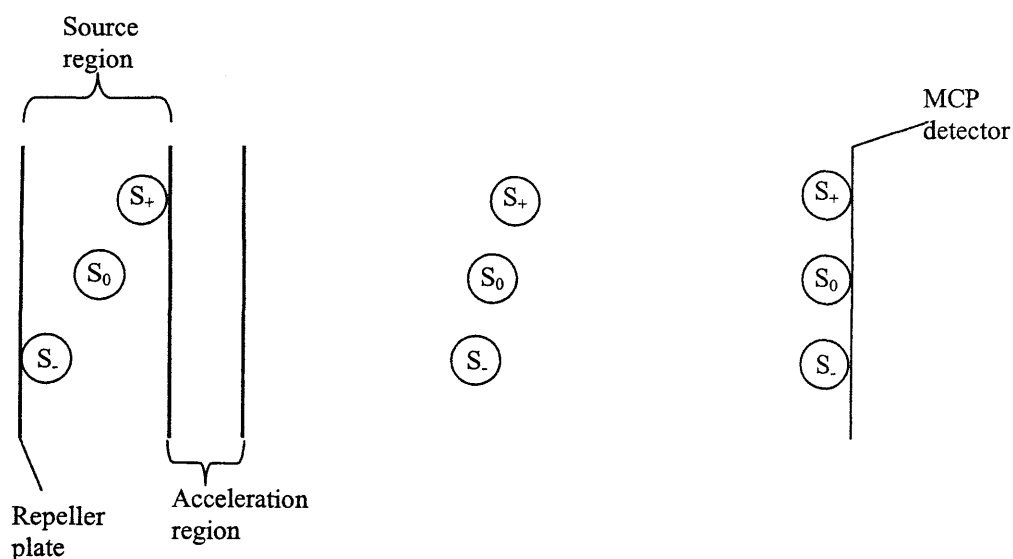


Figure 2.7 schematic representation of first order spatial focusing in a two field time of flight mass spectrometer

Ions being extracted from the source of the TOF by the electric field may have some spatial distribution about the centre of the source. If we consider three ions of equal mass and charge being formed in the TOFMS source with a spatial distribution along the axis of the TOFMS, as shown in figure 2.7, one ion S_0 formed in the centre of the source, a second ion S_- formed slightly further away from the TOFMS detector, and a third S_+ , formed slightly forward towards the TOFMS detector. When the repeller plate is pulsed to +400 V, the field created in the source region will cause the three identical ions to be accelerated towards the detector. However, The spatial distribution of the three ions will result in ion S_+ , being closer to the detector, having a “head start” over ions S_0 and S_- . Similarly, ion S_0 will have a head start over S_- . However, ion S_0 will experience the force created by electric field from the repeller plate pulse for a greater amount of time than that of S_+ . Similarly, S_- will experience the electric field for longer than S_0 . As a result of the differences in these electric field times, on entering the field free drift zone, S_- will have the highest velocity, S_0 will have an intermediate velocity and S_+ will be travelling slowest. Some distance along the field free drift zone, the ions initially further back from the detector will “catch up” with the ion initially closest to the detector. This point along the drift zone is known as the primary focal point. If the detector is placed at this focal point, then ions formed with an initial spatial distribution along the axis of the TOFMS will reach the detector simultaneously and so have equivalent flight times. That is, that there is no variation in τ_{tof} with initial position about the centre of the TOF source region s_0 .

$$\left[\frac{d\tau_{tof}}{ds} \right]_{s=s_0} = 0 \quad (2.10)$$

If these conditions are applied to the expression for the total flight time of an ion in a two field TOFMS, we have

$$D = 2sk^{3/2} \left[1 - \frac{1}{k + k^{1/2}} \frac{d}{s} \right] \quad (2.11)$$

$$k = \left[\frac{sE_s + dE_d}{sE_s} \right] \quad (2.12)$$

where E_s and E_d are the strengths of the electric fields in the source and accelerating regions respectively and k relates to the electric fields in the source and second accelerating region. In practice, space focusing may be achieved by adjusting the ratio of the electric fields E_d and E_s . All ion peaks within the mass spectrum will have a finite width corresponding to a range of ion flight times. This width arises because ions being formed over a range of positions in source region, even with good first order focusing, will increase peak width. Further complications arise as the ions in the TOF source region may have different initial velocities along the axis of the TOFMS. Ions experiencing the extraction field whilst travelling away from the MCP detector will have a certain ‘turn around’ time. That is, the time required for the electric field to change the direction of the ion’s motion. Also, ions with initial kinetic energy in the direction on the detector will have a final velocity in the field free drift zone greater than an ion with no initial kinetic energy. This initial kinetic energy distribution along the axis of the TOFMS will further increase the width of the peak in the mass spectrum.

A grid, held at 2.5 V, is positioned between the grounded acceleration grid and the drift tube grid to prevent stray ions from entering the acceleration region when the repeller plate is at ground potential.

2.2.5 Product ion detection

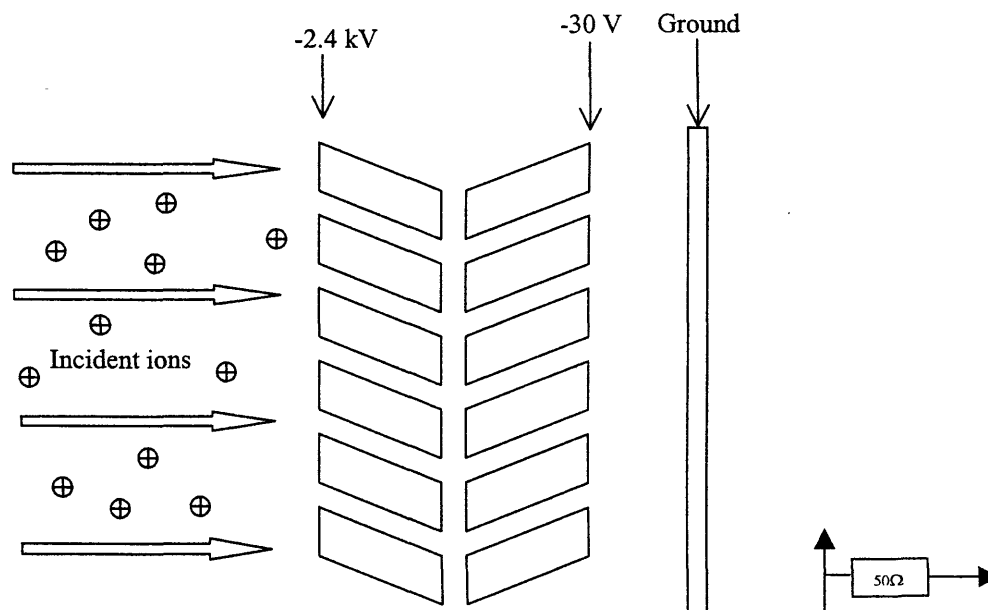


Figure 2.8 Microchannel plate detector

The detector positioned at the end of the flight tube of the TOFMS is a multichannel plate detector and works by amplifying a signal given by the arrival of an ion. The multichannel plate detector (figure 2.8) consists of two multichannel plates positioned one behind the other. The channels within the plates are angled with respect to the incident ions so that when an ion enters the channel it will strike the walls of that channel thereby ejecting secondary electrons. This process is illustrated in figure 2.9.

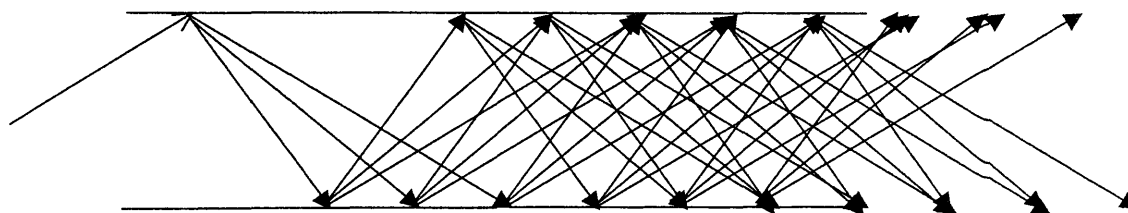


Figure 2.9 Schematic of a single channel in the microchannel plate detector. The first arrow represents the incident ion.

The result of this cascade in electrons from a single ion striking the detector is a large increase in current at the end of the channel. The electrons are drawn through the plates by the potential difference applied to the plates. The momentarily large electron current is amplified and discriminated by a constant fraction discriminator (CFD). This electron current “spike” is counted as one ion arrival. One ion arrival can generate more than 10^6 electrons. Ion arrivals are counted, converted to flight times and added to a histogram to build up a complete mass spectrum. This process is detailed below.

2.2.6 Time of flight measurements

The time of flight is determined by the difference in time of a start signal, given by a pulse of the accelerating potential and the stop signal triggered by the ion’s arrival at the detector. Since the difference in flight times of successive ions may be $<10^{-7}$ s, fast electronics are required. The advantages of this technique are that a complete mass spectrum is obtained for each pulse and that many mass spectra may be obtained every second allowing for more statistically significant results.

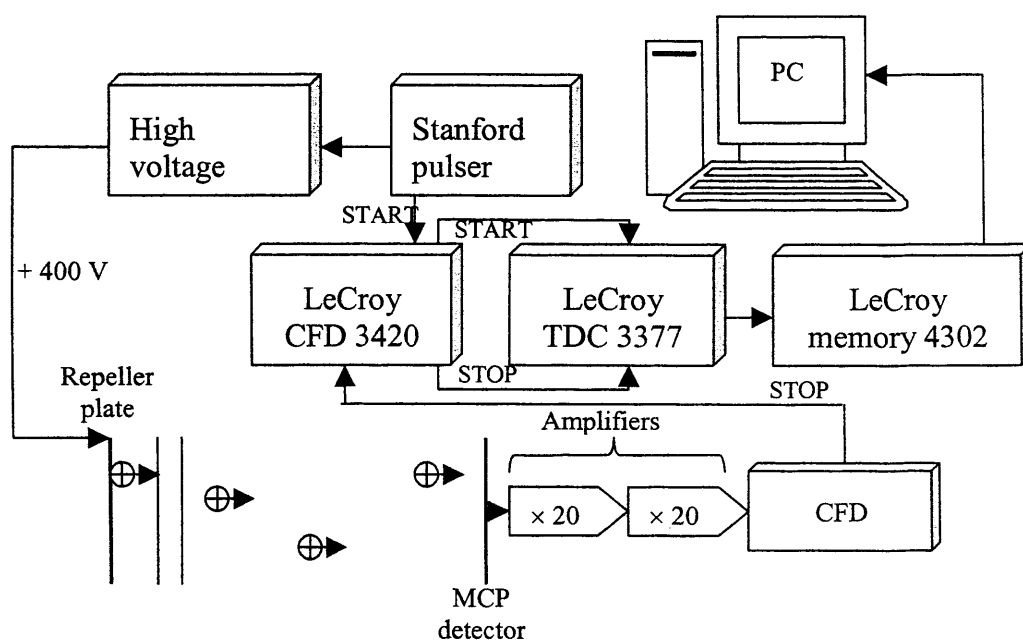


Figure 2.10 The TOFMS timing electronics.

Figure 2.10 shows schematically the electronic design of the crossed beam apparatus. The time of flight of an ion is measured by timing the difference between a START signal given when the ion is accelerated from the source and a STOP signal given when the ion reaches the detector at the end of the flight tube. When the pulse generator (Stanford) issues a pulse to the high voltage switch, + 400 V is applied to the repeller plate. This voltage causes an electric field which accelerates the ion out of the source. When the voltage is applied, the pulser sends a START signal to the Lecroy time to digital converter (TDC) via a Lecroy constant fraction discriminator (CFD). The CFD converts the pulse from the pulser to an ECL signal. The TDC then starts the timing cycle. This START signal is delayed slightly so that any RF noise generated by the high voltage applied to the repeller plate will not be detected. When the ion reaches the detector, a signal is sent from the MCP detector, amplified and discriminated and a STOP signal is sent to the TDC via the Lecroy CFD ending the timing cycle. The difference between the START and STOP signals

gives the time of flight of the ion. These times are stored in the Lecroy memory module. Once this memory module has accumulated 16 K of data, the ion's flight times are downloaded to a PC. A memory module is used to allow fast acquisition and transfer of data to the PC. Each memory download is termed one cycle. A mass spectrum is typically run for 1000 cycles. Each ion is allocated a channel number (from 1 to 1000) according to its flight time. Any ion having a flight time 0-6 ns is placed into channel 1, any having a flight time 6-12 is placed into channel number 2. This continues to channel number 1000. The range of ion flight times for each channel may be determined by the user. The complete mass spectrum is built up as a histogram, with each detected ion's flight time added in this way. A complete mass spectrum is typically run for about 5×10^6 ion counts. The software used to collect and process the accumulated data has been specially constructed in Visual Basic. The output file of a mass spectrum takes the form of a list of two columns, the first corresponds to ion channel number, and the second is the number of detected ions corresponding to that particular channel number. Channel number and flight time may easily be transposed to mass to charge ratio by equation (2.9). For example, a known gas may be introduced into the system. Using two peaks of known mass m and flight time τ_{tof} , it is a simple case of solving a simultaneous equation to determine c and k . These values of c and k may then be used to calculate the masses of unknown peaks in a new mass spectrum.

2.2.7 Single Collision Conditions

When interactions occur between the reactant dication and its neutral collision partner, it is important to ensure that any product formed is the result of a single collision. If the neutral collision gas is maintained at too high a pressure, it is likely

that multiple collisions will occur. A multiple collision is considered as occurring if an ion undergoes two or more collisions between the times of entering the source region and reaching the MCP detector. These multiple interactions could unnecessarily complicate a mass spectrum, as a product formed from multiple collisions may be the same as a product formed from a single collision. If the pressure is such that single collisions occur, then the intensity of any product ion peak should vary linearly with neutral collision gas pressure.

Experiments were carried out to ensure that the pressure was maintained within the single collision range. CF_3^{2+} was collided with H_2O at H_2O pressures of 2×10^{-6} torr, 4×10^{-6} torr, 6×10^{-6} torr and 8×10^{-6} torr. Background subtraction of the CF_2^+ peak ($m/z = 50$) was performed and then impurity ion subtraction of the spectrum carried out in the usual way (discussed in Chapter 3). The resultant, corrected spectrum was normalised to the CF_3^{2+} peak ($m/z = 34.5$). The relative intensity of the CF_2^+ peak was then plotted against H_2O pressure (Figure 2.11)

From Figure 2.11, it is clear that single collision conditions are maintained as the plot shows that a linear relationship between the neutral target gas pressure and the ion signal relative intensity. Under single collision conditions, the intensity of the product ion signal should be proportional to the H_2O pressure. We also expect that under single collision conditions, the product ion intensity will be proportional to the dication flux density.

$$I_{prod} \propto P_{\text{H}_2\text{O}} I_{\text{CF}_3^{2+}} \quad (2.13)$$

Since the dication current is not precisely constant, to remove any effects from its variation, we normalise the product ion yield to the dication current in the spectra. Normalising in this way gives relative ion intensities which can count across

experiments carried out for different durations and with different dication counts. By normalising, from equation (2.13) we get

$$\frac{I_{prod}}{I_{CF_3^{2+}}} \propto P_{H_2O} \quad (2.14)$$

So we would expect a graph of $I_{prod}/I_{dication}$ vs $P_{neutral}$ to be linear if single collision conditions are valid assuming that only a small number of the reactant dications react, during collisions with H_2O . Under single collision conditions, this is the case.

Experiments are typically carried out at an H_2O pressure of 4×10^{-6} Torr.

Further experiments were carried out to test the effect of variations in the pressure of the dication precursor gas in the electron impact source. For this, CF_2^{2+} was collided with H_2O at CF_4 pressures of 4, 6, and 8×10^{-6} mbar. The relative intensity of the CF_2^+ peak (normalised to the CF_2^{2+} peak) was plotted against CF_4 gas pressure (figure 2.12).

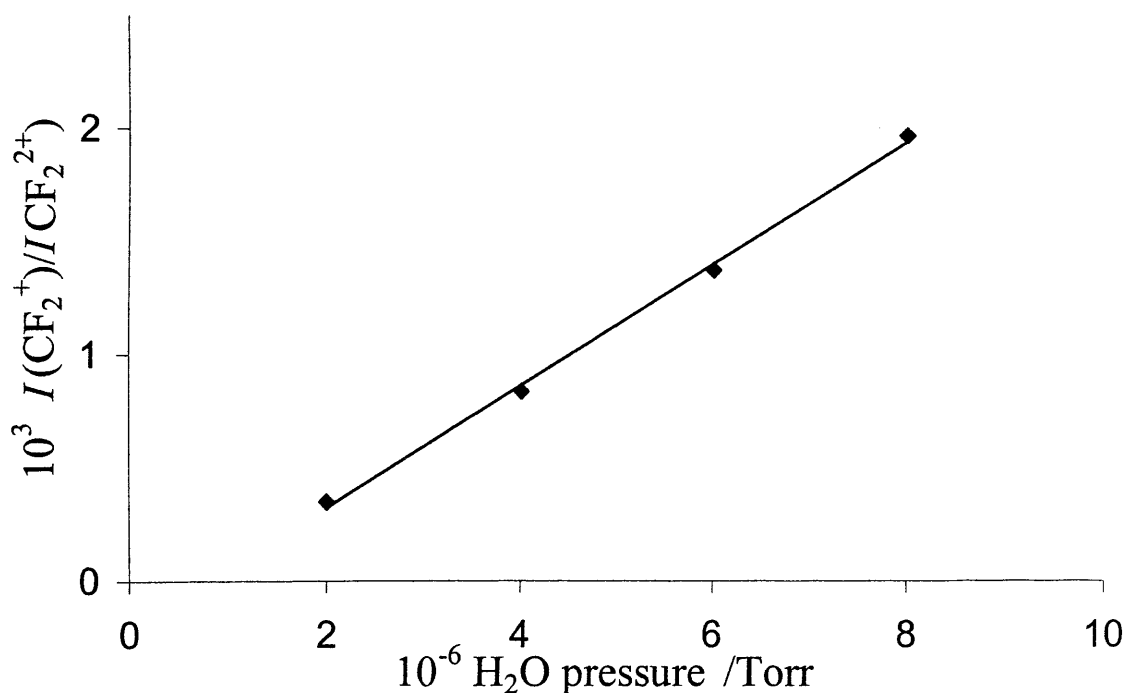


Figure 2.11 The variation of (CF_2^+/CF_2^{2+}) with neutral collision gas pressure

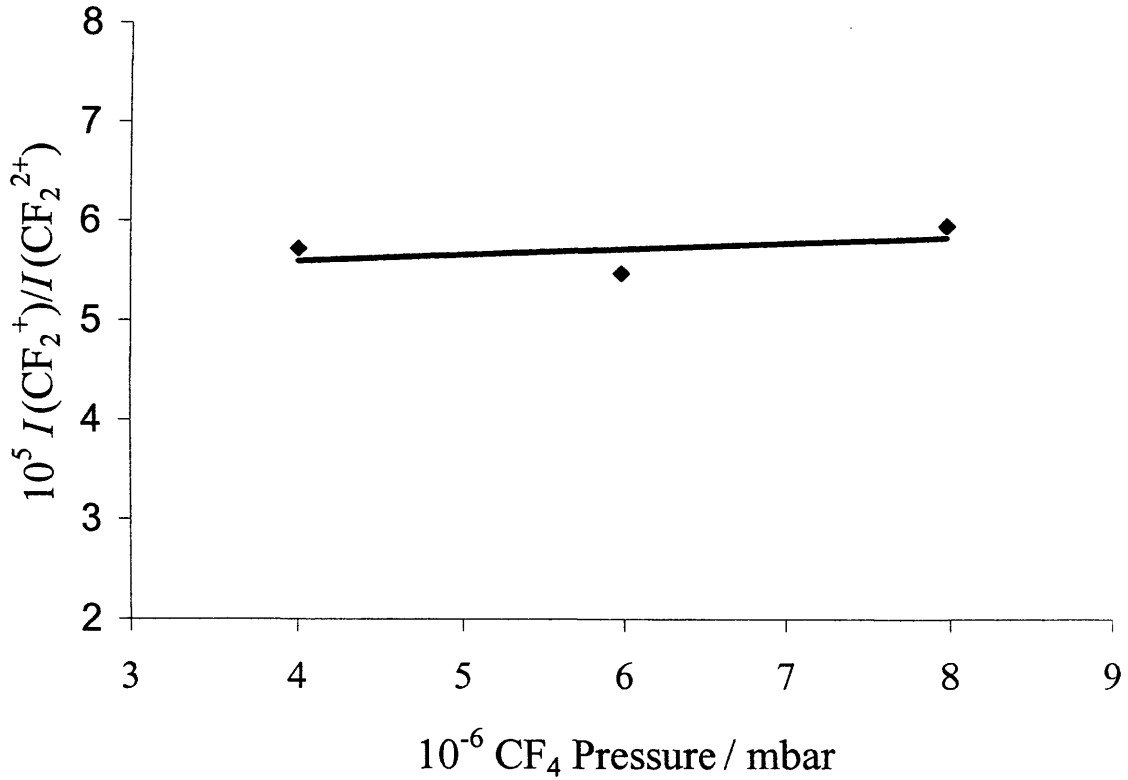


Figure 2.12 The variation of $(\text{CF}_2^+/\text{CF}_2^{2+})$ with dication precursor gas pressure

From figure 2.12, it is clear that product ion relative intensity is independent of source gas pressure. This is because

$$I_{\text{CF}_2^+} \propto P_{\text{H}_2\text{O}} I_{\text{CF}_3^{2+}} \quad (2.15)$$

$$I_{\text{CF}_3^{2+}} = k P_{\text{CF}_4} \quad (2.16)$$

$$I_{\text{CF}_2^+} = k' P_{\text{H}_2\text{O}} P_{\text{CF}_4} \quad (2.17)$$

$$\frac{I_{\text{CF}_2^+}}{I_{\text{CF}_3^{2+}}} = \frac{P_{\text{H}_2\text{O}} P_{\text{CF}_4} k'}{P_{\text{CF}_4} k} \quad (2.18)$$

$$\frac{I_{\text{CF}_2^+}}{I_{\text{CF}_3^{2+}}} = P_{\text{H}_2\text{O}} \frac{k'}{k} \quad (2.19)$$

Therefore, the relative intensity of the CF_2^+ signal should be proportional to the H_2O pressure, not the CF_4 pressure, as is observed.

2.2.8 Channeltron ion counter

In order to extract integral reaction cross sections (σ) from our raw data, which is one of the objectives of this project, it is necessary to accurately quantify the reactant dication current. However, at the high dication currents utilised in these experiments, certain saturation effects have been observed at the constant fraction discriminator (CFD). Saturation of the CFD occurs because there is a dead time of 70 ns after an ion has been counted, during which, if another ion arrives, it will not be counted. The probability that two dications will arrive within 70 ns of each other is only significant because the dication beam is pulsed towards the MCP detector and only affects the reactant dications because they are much more abundant. This 70 ns dead time means that some of the unreacted reactant dications arriving at the MCP detector will not be counted. Therefore, it was deemed necessary to find another method by which to measure the dication beam current.

In the line of the dication beam, perpendicular to the axis of the TOFMS, we positioned a channeltron detector. This channeltron has been incorporated into the crossed beam instrument in order to measure accurately the dication beam current. With the voltages on the TOFMS turned off, the ion beam passes through the TOFMS source and is focused into the channeltron detector by an electrostatic optic. Because there is a constant stream of dications (not pulsed), the probability of two ions reaching the channeltron within 70 ns of each other is negligible.

When this method was used to accurately quantify the reactant dication beam, it was found that charging at the mountings around the channeltron caused the count rate to

fluctuate in an erratic manner. This effect could not be eliminated. It was therefore necessary to find an alternative method by which to accurately count the unreacted reactant dications. This new, more successful, method is described in detail in Chapter 3 and involves precisely determining what proportion of the dications are not counted at a given dication current and adjusting our data processing methodology accordingly.

2.3 Operational parameters

Experiments are carried out at a rigidly maintained target gas pressure, typically 4.0×10^{-6} Torr. Table 2.13 gives a list of operational parameters.

Parameter	Typical Value
Laboratory frame collision energies	1-15 eV
Repeller plate pulse frequency	50 kHz
Precursor gas pressure	4×10^{-6} mbar
Neutral collision gas pressure	4×10^{-6} torr
EI electron energy	100 eV
Repeller plate potential	0 to +400 V
Field free drift zone potential	-1230 V
MCP detector front plate	-2400 V
MCP detector rear plate	+40 V
EI extraction electrode potential	-200 V
EI filament current	3.7 A
Electromagnet current	2.2 A

2.4 Conclusions

A detailed description of the cross beam time of flight apparatus has been given. All experiments are carried out under single collision conditions. A discussion of how the raw data obtained from these experiments is given in Chapter 3.

2.5 References

- 1 Z. Herman, P. Jonathan, A. G. Brenton and J. H. Beynon, *Chem. Phys. Lett.* **141** (1987) 433-442
- 2 C. J. Reid, J. A. Ballantine and F. M. Harris, *Int. J. Mass Spectrom. Ion Processes.* **93** (1989) 23-47
- 3 D. Mathur, R. G. Kingston, F. M. Harris, A. G. Brenton and J. H. Beynon, *J. Phys. B-Atom. Molec. Opt. Phys.* **20** (1987) 1811-1822
- 4 V. Krishnamurthi, K. Nagesha, V. R. Marathe and D. Mathur, *Phys. Rev. A.* **44** (1991) 5460-5467
- 5 C. J. Reid, F. M. Harris and J. H. Beynon, *Int. J. Mass Spectrom. Ion Processes.* **82** (1988) 151-162
- 6 J. M. Curtis and R. K. Boyd, *J. Chem. Phys.* **80** (1984) 1150-1161
- 7 K. Vekey, A. G. Brenton and J. H. Beynon, *J. Phys. Chem.* **90** (1986) 3569-3577
- 8 M. Hamdan and A. G. Brenton, *J. Phy. B-Atom. Molec. Opt. Phys.* **22** (1989) L 45-1 50
- 9 R. Susic, L. Lu, D. E. Riederer, D. Zigon, R. G. Cooks and T. Ast, *Org. Mass Spectrom.* **27** (1992) 769-776
- 10 L. Wahlin, *Nuclear Instruments & Methods in Physics Research Section B-beam Interactions with Materials and Atoms.* **27** (1964) 55
- 11 W. Wien, *Ann. Physik.* **65** (1898) 440
- 12 M. L. Oliphant, E. S. Shire and B. M. Crowther, *Proc. Royal Soc. (London).* **A146** (1934) 922
- 13 S. A. Rogers, S. D. Price and S. R. Leone, *J. Chem. Phys.* **98** (1993) 280-289
- 14 S. D. Price, S. A. Rogers and S. R. Leone, *J. Chem. Phys.* **98** (1993) 9455-9465
- 15 S. D. Price, M. Manning and S. R. Leone, *Chem. Phys. Lett.* **214** (1993) 553-558
- 16 S. D. Price, M. Manning and S. R. Leone, *J. Am. Chem. Soc.* **116** (1994) 8673-8680
- 17 D. A. Dahl, *SIMION*, Idaho National Engineering Labratory, 3.11, (1988)
- 18 W. C. Wiley and I. H. McLaren, *Rev. Sci. Inst.* **26** (1955) 1150

Chapter 3

Data reduction

3.1 Introduction

In order to extract meaningful information from our raw data, we use data reduction methods which take into account various aspects of the instrumental setup. These include knowledge of the internal dimensions of the time of flight mass spectrometer (TOFMS) and the timing electronics. This chapter describes, in detail, how the raw data was processed to extract integral reaction cross sections for the reaction processes we observed.

3.2 Data analysis

3.2.1 Determination of R_{obs}

In order to extract reliable information from our raw data, we must correct any raw data to allow for background counts and impurity ions. Background counts arise as a result of random stray ions hitting the detector and are seen as a non zero baseline. It is important to correct the data for background counts as some reaction channels, such as bond forming processes, may have small cross sections and the background counts may account for a significant proportion of the ion signal.¹⁻⁵ Although the dication beam is of high purity (> 99 %), impurity ions may be present in the mass spectrum as a result of unimolecular dissociation of the reactant dication,⁶ collision induced dissociation caused by the reactant dication colliding with residual gas in the chamber or undesired ions passing through the velocity filter due to its less than perfect resolution. These impurity ions may be the same ions as the product ions of interest formed as a result of collisions between the reactant dications and neutral collision partner.

Background subtraction is achieved, using the mass spectra we record, by selecting an appropriate background area in the spectrum close to the ion signal under consideration. The average number of counts per channel in this background area of the mass spectrum close to the peak of interest, is then subtracted from each channel of the product ion signal. In short, the background corrected ion signal intensity I_{bgc} is given as

$$I_{bgc} = I_{obs} - \left[\frac{I_{bgd}}{N_1} \right] \times N_2 \quad (3.1)$$

where I_{obs} is the observed ion signal intensity, I_{bgd} is the number of counts in the selected background region and N_2 and N_1 are the widths, in terms of number of channels, in the ion's signal and selected background region in the mass spectrum respectively.

Three mass spectra are collected and treated in this way. In addition to these three mass spectra, two mass spectra are collected in the absence of any neutral collision partner. These 'collision free' mass spectra allow us to determine which ion signals arise in our mass spectrum as a result of unwanted processes such as those outlined above. The collision free spectra are treated in exactly the same manner as the mass spectra collected in the presence of the neutral collision gas. In total, these five mass spectra, three with neutral collision gas and two without, make up one "set". Three of these sets are collected for each collision energy in the energy range under study. The I_{bgc} for each ion signal is averaged across the three mass spectra gathered in the presence of neutral collision gas. The same is done for the collision free mass spectra and the second subtracted from the first. This yields I , a value which is corrected for both background counts and impurity ions

$$I = \left[\frac{\sum I_{bgc}}{3} \right]_{gas\ on} - \left[\frac{\sum I_{bgc}}{2} \right]_{gas\ off} \quad (3.2)$$

Following this procedure, the background and impurity ion corrected I value for a particular ion in reaction channel j , I_j , for each ion signal is normalised to the background and impurity ion corrected value for the unreacted reactant dication I_0 to yield a value for $R_{obs}(j)$, the observed ion intensity ratio for a particular reaction channel j .

$$R_{obs} = \frac{I_j}{I_0} \quad (3.3)$$

However, in order to extract absolute reaction cross sections from our data, various other factors must be taken into consideration. These include mass discriminating effects of the TOFMS, that is, the fact that the TOFMS may count some ions more efficiently than others, kinetic energy release associated with these collision reactions and dication flux saturation at the CFD. By accurately knowing exactly how each of these factors affects the final ion signals in the mass spectrum, it is possible to determine integral reaction cross sections from our data. These data reduction methods are discussed in the following section.

3.2.2 Determination of integral reaction cross section σ' ⁷

The variation in the cross sections for the various product channels with collision energy for a given collision system can provide a valuable insight into the dynamics and mechanisms of the reactions which are occurring. In previous investigations we extracted from our data the ratio of the cross sections of pairs of product channels.^{4,8} Such ‘‘product ion ratios’’ are independent of the target gas pressure and their extraction

from the experimental mass spectra does not require a detailed consideration of the detection efficiency of the unreacted dications. However, accounting for the variation of such product ion ratios with the collision energy is not straightforward, as the cross sections of both of the reaction channels under consideration may vary with collision energy. To overcome these problems we present below a new data analysis procedure, which allows us to extract integral reactive cross sections from the $R_{obs}(j)$ values by accurately counting the unreacted reactant dications.

If the cross section for a particular reaction channel j is σ_j then

$$F_u = F_0 e^{-\sigma_j nl} \quad (3.4)$$

Where F_u is the final flux of the dication beam, that is the flux of the unreacted reactant dications, F_0 is the initial flux of the dication beam, n is the number density of the neutral collision partner and l is the length of the interaction region in which a collision may occur. The reduction in this dication flux on passing through an interaction region is

$$F_0 - F_u = F_j \quad (3.5)$$

and

$$F_0 - F_u = F_0 - F_0 e^{-\sigma_j nl} \quad (3.6)$$

$$= (1 - e^{-\sigma_j nl}) F_0 \quad (3.7)$$

However, when $\sigma_j nl$ is small, $e^{-\sigma_j nl}$ may be approximated as

$$e^{-\sigma_j nl} \approx 1 - \sigma_j nl \quad (3.8)$$

The initial flux F_0 may not be directly determined from our experiments. However, because only a very small fraction of incident dications react during an experiment (<1%), $F_0 \approx F_u$, we may use F_0 instead of F_u . From the above, we have

$$F_j = \sigma_j n l F_0 \quad (3.9)$$

where F_j is the flux of the product channel j . Rearranging, we have

$$\sigma_j = \frac{F_j}{n l F_0} \quad (3.10)$$

The initial flux, F_0 , of the dication beam is the product of the ion density of the initial dication beam and its velocity.

$$F_0 = \rho_0 v_0 \quad (3.11)$$

Similarly, the flux of the product ion is the product of the ion density of the product and its velocity

$$F_j = \rho_j v_j \quad (3.12)$$

substituting equations 3.11 and 3.12 into equation 3.10 gives

$$\sigma_j = \frac{\rho_j v_j}{n l \rho_0 v_0} \quad (3.13)$$

ρ may be expressed in terms of the detected ion intensity I , the volume of the interaction region imaged onto the detector V and some constant k , where k is a mass independent ion detection efficiency. For reaction channel j and for the reactant dication, we have

$$\rho_j = \frac{k I_j}{V_j} \quad (3.14)$$

and

$$\rho_0 = \frac{k I_0}{V_0} \quad (3.15)$$

The volume of the interaction region imaged onto the detector is included here as ions with different kinetic energies across the source region of the TOFMS possess different velocities and so will travel different distances orthogonal to the axis of the TOFMS prior to reaching the end of the TOFMS. Hence, a certain ion with a certain velocity across the source region will image a certain volume of the source onto the detector. A different ion possessing a different velocity will image a different volume of the source region onto the detector. After a reaction occurs between a dication and a neutral, the product ions may separate from each other with a considerable release of kinetic energy. This kinetic energy release (KER) arises as a result of the Coulomb repulsion experienced by the two positive charges in close proximity. This KER is released in the centre of mass frame and affects the ion's velocity in the laboratory frame. As a result of this KER, two product ions with different masses may depart with different velocities across the source region of the TOFMS. For these calculations, the reaction is known to give forward scattering of the ion derived from the reactant dication.⁵ The difference in these ions' transverse velocities across the source region of the TOFMS means that they will travel different distances perpendicularly to the axis of the TOFMS before reaching the detector. Consequently, more energetic ions may not reach the detector but be lost to the sides of the chamber. Figure 3.1 shows how the trajectories of two ions with different energies across the TOFMS may behave. Trajectory A shows an ion formed with low kinetic energy. Any ion formed with less kinetic energy than the ion tracing trajectory A will be lost to the sides of the chamber. Similarly, Trajectory B shows an ion formed with high kinetic energy. Any ion formed with higher kinetic energy than the ion tracing trajectory B will be lost to the sides of the chamber.

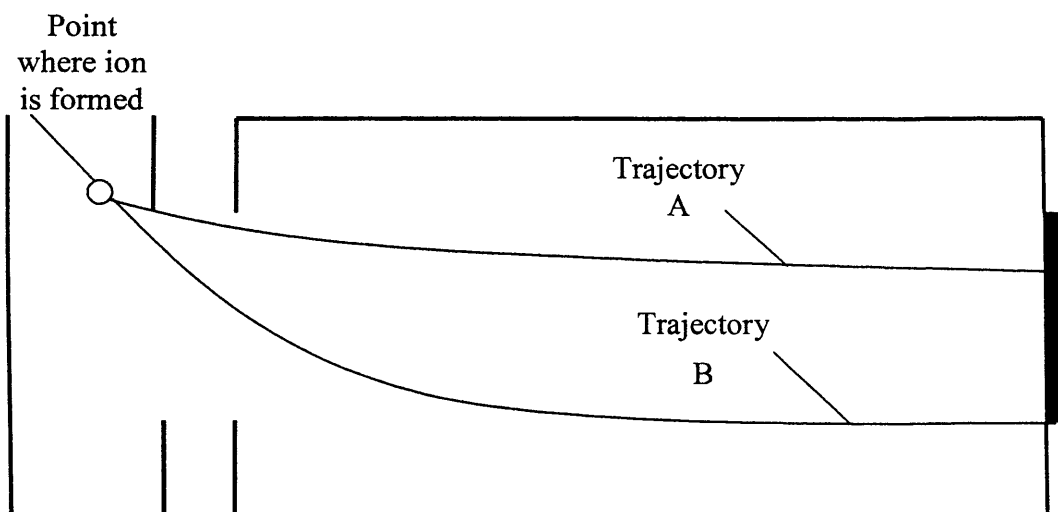


Figure 3.1 Trajectories of two ions. One with low kinetic energy perpendicular to the axis of the TOFMS (Trajectory A) and the other with high kinetic energy (Trajectory B)

For a particular reaction channel, where the ion produced possesses a certain laboratory frame kinetic energy across the TOFMS, there will be a range of positions, in which, if the ion is formed, it will reach the detector and not be lost to the sides of the chamber. This area, in which the ion may be formed and not be lost, will be cylindrical in shape, being determined by the cross sectional shape of the incident dication beam.

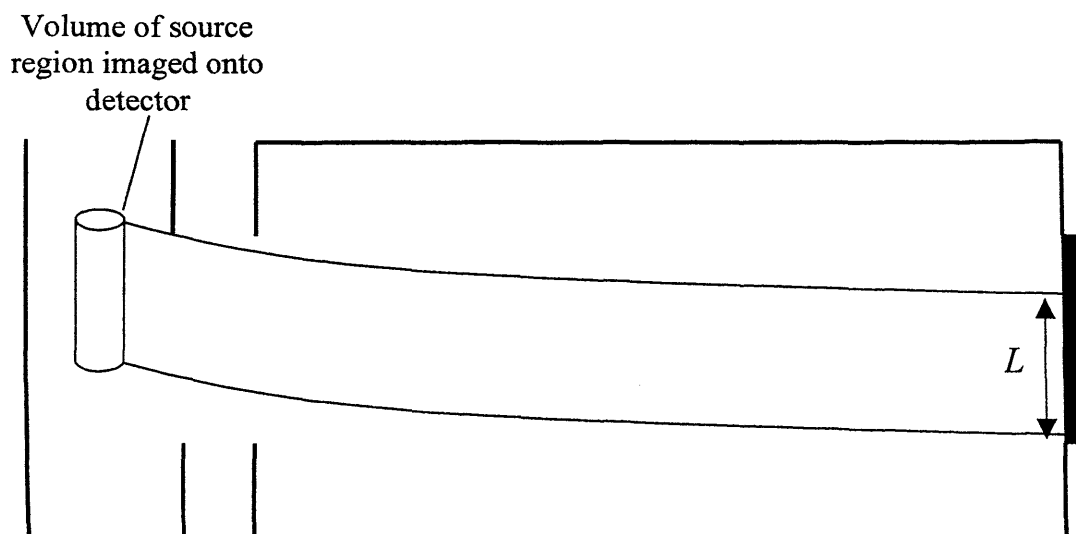


Figure 3.2 The volume of the TOFMS source region imaged onto the detector. L is used in calculating integral reaction cross sections

The volume of the source region imaged on to the detector may be expressed as a length L and an area A .

$$V_j = A_j L_j \quad (3.16)$$

and

$$V_0 = A_0 L_0 \quad (3.17)$$

for reaction channel j and the detection respectively. Combining equations 3.13, 3.14, 3.15, 3.16 and 3.17 gives

$$\sigma_j = \frac{k I_j \nu_j A_0 L_0}{n I_0 \nu_0 A_j L_j} \quad (3.18)$$

However, the cross sectional areas of the interaction region imaged onto the detector for the initial flux F_0 and the product channel flux F_j are equivalent for the same reaction system because the detection beam is the same throughout, so

$$A_0 = A_j \quad (3.19)$$

and

$$\sigma_j = \frac{I_j v_j L_0}{I_0 v_0 L_j} \frac{1}{nl} = \frac{v_j L_u}{v_u L_j nl} \frac{R_{obs}(j)}{c} \quad (3.20)$$

I_j and I_0 are the detected ion intensities of the product j and the reactant dication. v_j and v_0 are their velocities and L_j and L_0 are their effective lengths of the source region imaged onto the detector. n is the number density of the neutral gas and l is the interaction path length. n and l are constant for a particular reaction system at constant pressure.

Equation 3.20 shows that, in order to calculate the absolute reaction cross section σ_j , we require the laboratory frame velocities of the ion j , and the reactant dication, and the lengths of the TOFMS source region imaged onto the detector. All of these parameters may be calculated using knowledge of the internal dimensions of the TOFMS and simple ion dynamics. The total kinetic energy release of the two monocationic products following an electron transfer reaction is usually about 7 eV. Therefore, we have

$$\frac{1}{2} m_1 v_1^2 + \frac{1}{2} m_2 v_2^2 = 7q \quad (3.21)$$

where m_1 , v_1 , m_2 and v_2 are the masses and velocities of electron transfer product ions 1 and 2. We also know that, in the center of mass frame, the sum of the momenta of the electron transfer products following the reaction is zero. Therefore we have

$$m_1 v_1 + m_2 v_2 = 0 \quad (3.22)$$

By solving equations 3.21 and 3.22 simultaneously, it is possible to calculate the velocity v of an ion across the source region of the source region of the TOFMS. This velocity then allows the length of the source region imaged onto the detector, L , to be calculated using the dimensions of the TOFMS to determine whether an ion will reach the detector or be lost to the walls of the chamber.

The value $I_j/I_0 (R_{obs}(j))$ is evaluated using the method in the previous section of this chapter. Unfortunately, an additional constant c ($c \geq 1$) is required in equation 3.20 to quantify saturation effects associated with the constant fraction discriminator, which means that the reactant dications are not, at higher dication beam currents, detected by the experimental electronics with the same efficiency as the product ions. Thus, experimental values of I_u may underestimate the flux of unreacted dications and the experimental values of $R_{obs}(j)$ are artificially large. However, as shown in the next section, this reduction in the dication detection efficiency can be quantified, that is, c can be accurately determined, so that integral reaction cross sections in arbitrary units can be evaluated using equation 3.20. As described above, in previous studies we presented the variation in the relative yields of pairs of product ions with collision energy. This procedure was adopted as these product ion ratios are independent of target gas pressure and ion beam fluctuations. However, the above analysis shows that, as long as the neutral gas pressure (n) and beam quality (affecting A and I) can be maintained throughout a series of experiments, by expressing our product ion intensities relative to the accurately measured intensity of the unreacted dication signal we can extract a value which is directly proportional to the absolute reaction cross section, with a constant of proportionality that will not vary between experiments. That is, we can extract values of the integral cross sections σ_j in arbitrary units. These values of σ_j are, of course, proportional to the absolute reaction cross section.

3.2.3 Determination of c

For every real ion signal which is sent from the multichannel plates to the CFD, a corresponding signal is sent to the TDC and an ion is counted. However, if two (or

more) ions arrive at the MCP detector in close succession, within the dead time (70 ns) of the CFD, the later ions will not be counted. The space focus of the TOFMS means that the temporal width of the dication peak in the TOF mass spectrum is less than 20 ns. Hence, if more than one dication reaches the detector following a given repeller plate pulse then the second arrival will be lost within the dead-time of the CFD. Hence, at significant dication currents, the number of reactant dications reaching the detector during the course of the acquisition of a mass spectrum may well be greater than that recorded in the mass spectrum via the TDC. It is important to note that the dead-time losses described above only affect the dication signals. This is because the number of unreacted dications detected, approximately 0.3–0.8 per repeller plate pulse on average, is far greater than the number of product ions detected, as we operate under single collision conditions. This means that the probability of two product ions arriving within the dead-time of the CFD is negligible. Hence, the CFD losses will lead to the raw values $R_{obs}(j)$, being larger than the true value $R_{real}(j) = R_{obs}(j)/c$. We need only to determine a value of c for each set of mass spectra recorded, as the dication beam current is effectively constant during the accumulation of the five mass spectra making up a set. In practice, we endeavour to use the lowest practical dication beam current in our experiments and to keep the dication beam current approximately constant between the different sets of mass spectra we record. This results in c being as close to unity as possible and not varying dramatically between different sets of spectra. To determine c we must consider in detail how we record a mass spectrum. Each pulse of the TOF repeller plate causes any ions in the source region to accelerate towards the detector. Any ion that does not arrive when the CFD is “dead” is then allocated a flight time.

These flight times are accumulated in a memory module until it is full (16 kbytes). Once the memory unit is full, the data is downloaded to a PC. Each filling of the memory unit and subsequent download is termed one “cycle ” of the data acquisition process and each mass spectrum is acquired for 1000 cycles.

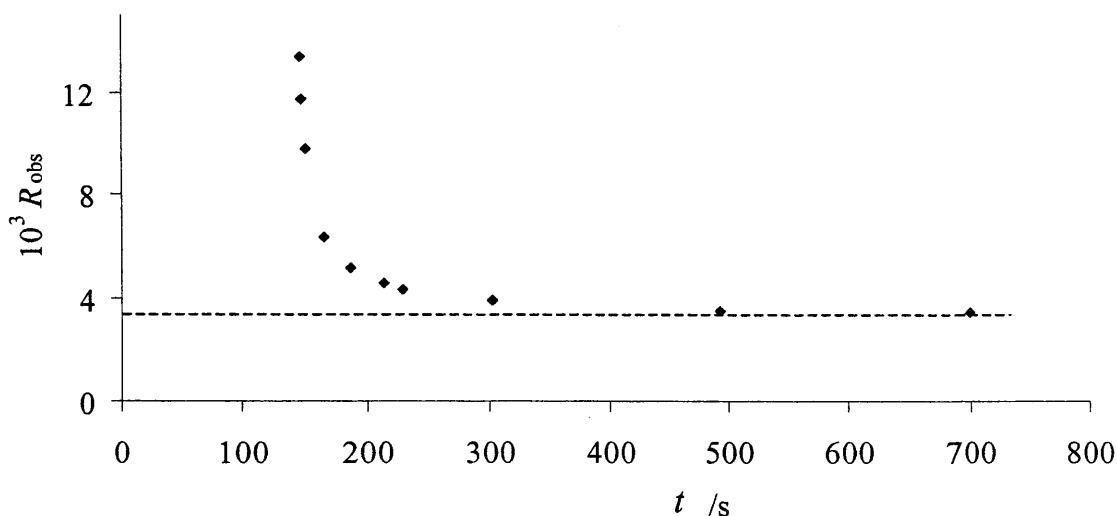


Figure 3.3 Plot of R_{obs} , the ratio of the product ion CF_2^+ signal intensity to the unreacted reactant dication signal intensity, against mass spectral acquisition time. The dashed line shows the value of R_{real} which is 3.4×10^{-3}

The time t taken to accumulate a mass spectrum, that is the time for 1000 cycles, is dependent on the time taken to accumulate 16 kbytes of data, which is in turn dependent on the dication beam current, since unreacted dications dominate the ions detected. If there is a large dication beam current, accumulating 1000 cycles takes a shorter period of time than at low dication beam currents. Thus, the value of t for a mass spectrum can be used to quantify the dication current during that spectrum.

If, by recording mass spectra at different dication beam currents, we record the variation of $R_{obs}(j)$ as a function of t we produce a curve (Figure 3.3) which converges at large t , that is low dication currents, to $R_{real}(j)$, the value of $R_{obs}(j)$ when $c = 1$. If for this same

dataset of $R_{obs}(j)$ as a function of t , after performing experiments at low dication beam currents to determine $R_{real}(j)$, we plot $R_{obs}(j)/R_{real}$ against t , we generate a calibration curve (Figure 3.4) which tends towards unity from above with increasing t . A function has been fitted to this curve:

$$\frac{R_{obs}(j)}{R_{real}(j)} = c = \frac{a}{t^n} + 1 \quad (3.23)$$

where a and n are variables which can be adjusted to improve the quality of the fit. Here, $a = 1.4 \times 10^{13}$ and $n = 5.94$. Equation 3.23 fits the calibration curve well, with a correlation coefficient r of 0.88. Very similar values of a and n are derived for fits to calibration curves determined for the formation of different product ions from a variety of collision systems at different collision energies. Hence, Equation 3.23 can be considered an empirical “ general calibration curve”. So, if a given reactive channel yields a value of R_{obs} in a mass spectrum recorded for t seconds then the appropriate value of c can be determined from Equation 3.23.

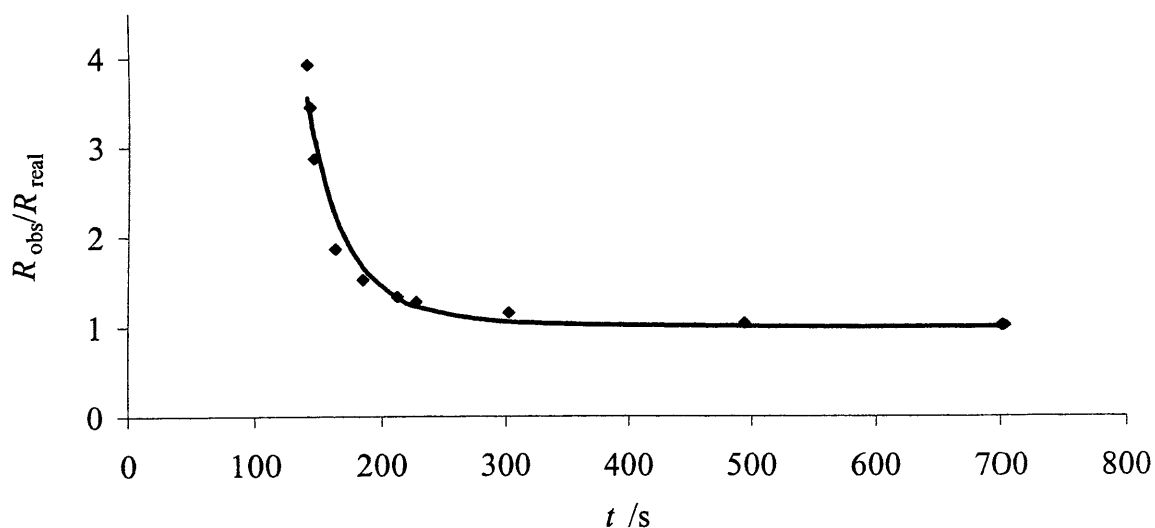


Figure 3.4 Plot of R_{obs}/R_{real} against mass spectral acquisition time. The curve is fitted using the least squares method

In practice, the average time t taken to record each of the individual mass spectra making up a set is used via Equation 3.23 to determine c for that set. The values of $R_{obs}(j)$ for that set of data can then be corrected to yield the values of $R_{real}(j)$ for that set. The average value of $R_{real}(j)$ for several sets of data at a specific collision energy are then used in the determination of the integral reaction cross section σ'_j , in arbitrary units, at that collision energy:

$$\sigma'_j = nl\sigma_j = \frac{v_j L_u}{v_u L_j} R_{real}(j) \quad (3.24)$$

3.3 Conclusion

The data analysis procedure used to extract integral reaction cross sections from our raw data has been reviewed. This analysis accounts for background and impurity ions in the mass spectrum, kinetic energies of product ions and saturation effects of the electronics.

3.4 References

- 1 S. D. Price, M. Manning and S. R. Leone, *J. Am. Chem. Soc.* **116** (1994) 8673-8680
- 2 S. D. Price, *J. Chem. Soc. Faraday Trans.* **93** (1997) 2451-2460
- 3 K. A. Newson and S. D. Price, *Chem. Phys. Lett.* **269** (1997) 93-98
- 4 K. A. Newson and S. D. Price, *Chem. Phys. Lett.* **294** (1998) 223-228
- 5 Z. Dolejšek, M. Farnik and Z. Herman, *Chem. Phys. Lett.* **235** (1995) 99-104
- 6 R. D. Levine and R. B. Bernstein, *Molecular Reaction Dynamics and Chemical Reactivity*, (1987)
- 7 D. Kearney and S. D. Price, *Phys. Chem. Chem. Phys.* **5** (2003) 1575-1583
- 8 K. A. Newson, N. Tafadar and S. D. Price, *J. Chem. Soc. Faraday Trans.* **94** (1998) 2735-2740

Chapter 4

A theoretical perspective

4.1 Introduction

This chapter examines some of the theoretical aspects of collisions between dicationic and neutral species. Electron transfer, forming monocations from the reactant dication and neutral often dominates the bimolecular reactivity of dications.¹⁻³ The ‘reaction window’ model based on the Landau-Zener theory^{4,5} has been a useful tool during the course of these investigations which compliments the experimental results obtained.

Also contained in this chapter, are descriptions of the centre of mass co-ordinate system and collision and reaction cross section theory.

4.2 Reaction window model based on the Landau-Zener Theory

The relative abundance of the product ions from electron transfer reactions may be rationalised using the “Reaction Window” model derived from the Landau-Zener theory.^{4,5} This model may be used to predict the probability of an electron transfer reaction between a dication and a neutral. In this model an electron transfer occurs at the crossing of two simple electrostatic diabatic potential energy surfaces corresponding to the reactants ($X^{2+} + Y$) and products ($X^+ + Y^+$). The interaction between the reactants is modelled as the sum of a simple polarisation attraction potential derived from the polarisability of the neutral α , and the reaction exothermicity ΔE .

$$V_r = -\frac{z^2 e^2 \alpha}{8\pi\epsilon_0 r^4} + \Delta E \quad (4.1)$$

This simple polarization attraction model does not take into account the large repulsive wall encountered at very small interspecies separation. However, this is not a problem as the repulsive wall occurs at much smaller interspecies separation than the curve crossings. The product potential is represented as purely repulsive.

$$V_p = \frac{e^2}{4\pi\epsilon_0 r} \quad (4.2)$$

Where the zero of energy is defined as the point of infinite separation of the two monocationic products. The interspecies separation of the intersection of these two potential energy curves, the curve crossing radius, then determines the probability of electron transfer.

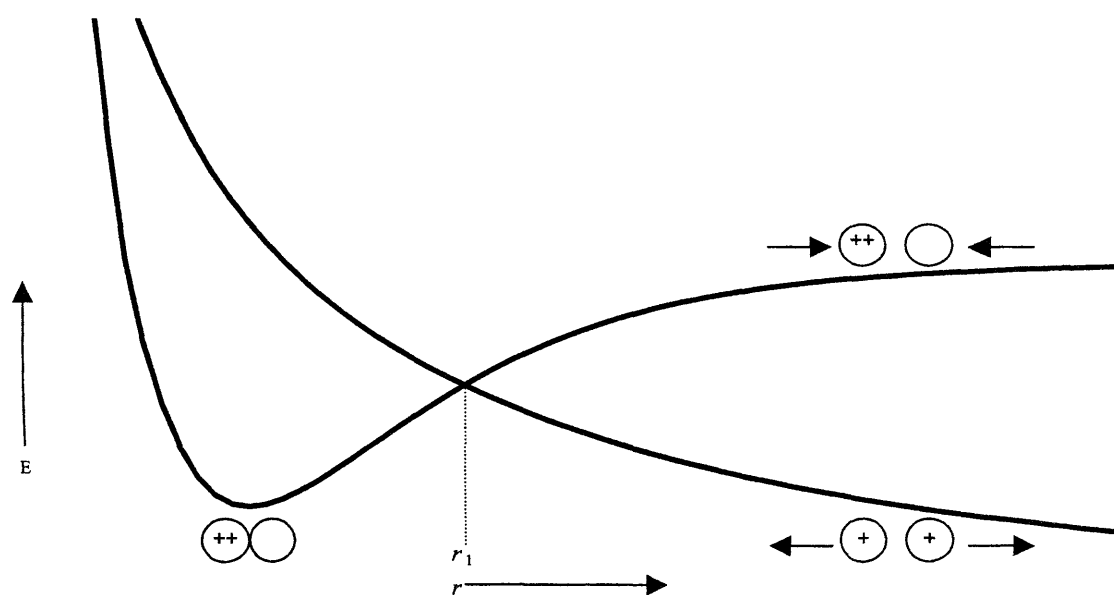


Figure 4.1 the curve crossing point r_1 of the two diabatic curves, one corresponding to dication plus neutral and the other corresponding to two monocations, is the interspecies separation at which electron transfer occurs.

If the curve crossing is at a large interspecies separation then there is little interaction between the reactant and product states and the probability for electron transfer is small. Conversely, if the curve crossing is at small interspecies separation then the two states interact strongly and there is a high likelihood of electron transfer, on one

pass through the crossing. However, to react, the system must pass through the curve crossing twice, once on approach and again on separation. Hence, for small crossing radii the net probability of electron transfer is small even though the probability of electron transfer on one pass through the crossing is large. Between these two behavioural limits there is a range of interspecies separations, the reaction window where the coupling is neither too weak nor too strong and effective electron transfer can result. The cross sections for the population of the different product electronic states can be calculated using this reaction window model. If the products are formed in stable electronic states, then non-dissociative electron transfer results. However, if the products are formed in unstable electronic states then dissociative electron transfer will result. Thus, to predict which ions are observed in the mass spectrum we need to know both the probability for populating the available electronic states of each of the primary electron transfer products and also the stability of these electronic states.

If δ is the probability that there is no change in electronic state (i.e. remaining on the diabatic curve through the crossing), then the overall probability P that an electron transfer reaction will occur is given by

$$P = 2\delta(1 - \delta) \quad (4.3)$$

The value of δ is evaluated using the magnitude of the difference in the gradients of the two potential curves at the crossing radius $|V_2' - V_1'|$, the relative radial velocity at the crossing v_b , which can be calculated for a given impact parameter from the collision energy and the interaction potential, and the electronic coupling matrix H_{12} .

$$\delta = \exp\left(\frac{-\pi|H_{12}|^2}{2\hbar|V_1' - V_2'|v_b}\right) \quad (4.4)$$

The *ab initio* calculation of the electronic coupling matrix element requires a detailed description of the wavefunctions of the collision system. However, here H_{12} is evaluated from the ionization potentials of the reactants and the curve crossing radius using the semi-empirical formula of Olson *et al.*⁶

$$|H_{12}| = (I_A I_B)^{1/2} (R_c^*)^2 \exp(-1.72 R_c^*) \quad (4.5)$$

where

$$R_c^* = \left(\frac{\sqrt{I_A} + \sqrt{I_B}}{\sqrt{2}} \right) R_c \quad (4.6)$$

If the curve crossing is at large interspecies separation, δ will be effectively unity as $|H_{12}|$ is small. Whilst if the curve crossing is at small interspecies separation δ will approach zero as $|H_{12}|$ is large. Between these two limits, in the reaction window, P can approach the Landau–Zener maximum of 0.5. The probability of an electron transfer reaction P is a function of the radial collision velocity v_b , which is in turn a function of the collision energy and impact parameter b . At a given collision energy we can evaluate the electron transfer cross section σ_{calc} by integrating P over b from $b = 0$ to b_{max} , the maximum value of b for which the collision system reaches the crossing radius:

$$\sigma_{calc} = \int_0^{b_{max}} 2\pi P(b) b \, db \quad (4.7)$$

From Figure 4.2, it is clear that the interspecies separation at which this curve crossing occurs is largely dependant upon the exothermicity of the reaction



If the exothermicity is small (ΔE_1), the curve crossing radius of the product and reactant states will occur at large interspecies separation (r_3) and so be outside the reaction window. Similarly, if the exothermicity is large (ΔE_3), the curve crossing

will occur at small interspecies separation (r_1), again placing it outside the reaction window. However, if the exothermicity is within certain limits (ΔE_3), usually between about 2 eV and 6 eV, the curve crossing radius (r_2) of the product and reactant states will lie in the reaction window and net electron transfer will occur.

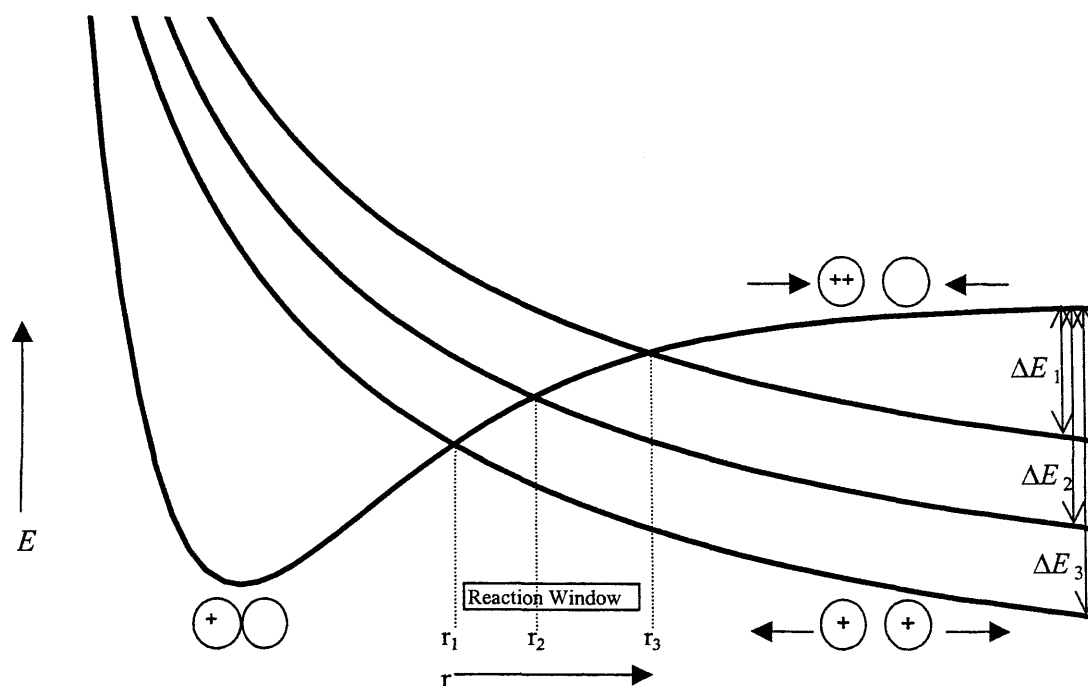


Figure 4.2 A Landau-Zener reaction window diagram showing the link between curve crossing radius and reaction exothermicity.

In practice, in order to model the dication neutral electron transfer reaction, it is only necessary to construct the potential energy surfaces of the reactants and products. If the curve crossing lies within the reaction window, then electron transfer will proceed.

The calculations performed with this model only give approximate values for the reaction cross sections. However, in the past the Landau-Zener model has proved successful in the semi-quantitative rationalisation of product ion yields in dication neutral electron transfer reactions.^{1,7-10} The success of this model is due, largely, to the fact that electron transfer occurs at relatively large interspecies separation (3-6 Å)

where the modelled potential energy surfaces provide a good approximation to the real potential energy surfaces. For example, it has been shown that for collisions between molecular dications and rare gas atoms, electron transfer is not favoured between dications and light rare gases such as He and Ne where the reactions are only slightly exothermic or even endothermic. However, for heavier rare gases, where the ionisation potentials are less, electron transfer does proceed as the exothermicities for these reactions lie within the reaction window of exothermicities.¹⁰

During collisions between dications and neutrals, the exothermicity dictates whether an electron transfer process will be dissociative or non-dissociative. If a large exothermicity is required to populate the lower vibrational levels of an electronic state, then these low vibrational levels will not be populated. However, higher vibrational levels of that electronic state may fall within the window of exothermicities and so be populated. These vibrationally excited electron transfer products may fragment to yield dissociative electron transfer products.

4.3 Centre of mass frame¹¹

The motion of two colliding bodies may be described in terms of the independent motion of each body relative to the laboratory. This is known as the laboratory frame. However, this particular reference frame is not appropriate for the collisions described here as a relatively large number of parameters must be considered in order to model collisions of this nature. Instead, the motions of the colliding bodies are described relative to each other and to their centre of mass. For this reason, this reference frame is known as the centre of mass frame (COM). Calculations are simplified by the fact that, by definition, the total linear momentum of the two bodies in the COM frame is zero and the COM moves at a constant velocity relative

to the laboratory. The COM collision energy is the total energy available to the system, with which work, such as rearrangement of bonds or electron or energy transfer, may be done.

The distances of the two bodies from the COM are r_a and r_b respectively, where

$$r_a = \frac{m_b}{m_a + m_b} (R_a - R_b) \quad (4.9)$$

and R_a and R_b are the distances of A and B respectively, from the laboratory frame origin, that is the point of collision in the laboratory frame.

Similarly

$$r_b = \frac{-m_a}{m_a + m_b} (R_a - R_b) \quad (4.10)$$

The velocity vectors, u_a and u_b may be evaluated simply by differentiating equations 4.9 and 4.10 with respect to time

$$u_a = \frac{dr_a}{dt} = \frac{m_b}{m_a + m_b} (v_a - v_b) \quad (4.11)$$

and

$$u_b = \frac{dr_b}{dt} = \frac{-m_a}{m_a + m_b} (v_a - v_b) \quad (4.12)$$

equations 4.11 and 4.12 may be combined to yield the sum of the linear momenta of the two colliding bodies in the COM frame ΣP_{COM} .

$$\Sigma P_{COM} = m_a u_a + m_b u_b = \frac{m_a m_b}{m_a + m_b} (v_a - v_b) - \frac{m_a m_b}{m_a + m_b} (v_a - v_b) = 0 \quad (4.13)$$

this shows that the total linear momentum of the system in the COM frame is zero.

In a similar analysis to that above, the relative kinetic energies of the two colliding bodies of COM kinetic energies of T_a and T_b may be given by

$$T_a = \frac{1}{2} m_a u_a^2 = \frac{1}{2} m_a \left[\frac{m_b}{m_a + m_b} (v_a - v_b) \right]^2 \quad (4.14)$$

and

$$T_b = \frac{1}{2} m_b u_b^2 = \frac{1}{2} m_b \left[\frac{-m_a}{m_a + m_b} (v_a - v_b) \right]^2 \quad (4.15)$$

therefore, the combined centre of mass kinetic energy, T , is given as

$$T = T_a + T_b = \frac{1}{2} \frac{m_a m_b}{m_a + m_b} (v_a - v_b)^2 \left[\frac{m_b}{m_a + m_b} + \frac{m_a}{m_a + m_b} \right] \quad (4.16)$$

This may be simplified to

$$T = \frac{1}{2} \mu v^2 \quad (4.17)$$

where μ is the reduced mass and v is the relative velocity of the colliding bodies. However, when considering dication neutral reactions using our experimental setup, the neutral, having only thermal velocity, is effectively stationary compared to the reactant dication. Therefore, the relative velocity of the two colliding bodies is equivalent to the laboratory frame velocity of the dication. The collision energy in the centre of mass frame is therefore given as

$$T = \frac{\mu}{m_D} E \quad (4.18)$$

where m_D is the mass of the dication and E is the laboratory frame collision energy.

In comparing the centre of mass frame with the laboratory frame for collisions, it is useful to use a Newton diagram. Figure 4.3 shows how the centre of mass frame co-ordinates relate to the laboratory frame co-ordinates for a simple, non-dissociative electron transfer reaction during a collision between a dication and a neutral.

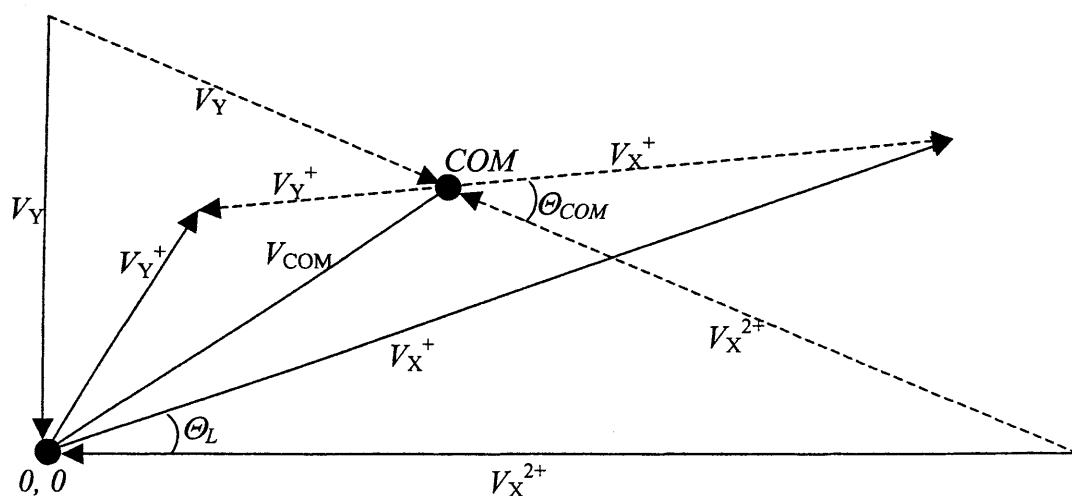


Figure 4.3 A schematic diagram of how the centre of mass velocity vectors (V) relate to those of the laboratory frame for the electron transfer reaction $X^{2+} + Y \rightarrow X^+ + Y^+$. the solid lines represent velocities in the laboratory frame whereas the dashed lines represent velocities in the centre of mass frame. $0,0$ is the collision point in the laboratory frame. θ_L is the laboratory scattering angle relative to V_X^{2+} (solid) and θ_{COM} is the centre of mass scattering angle relative to V_X^{2+} (dashed).

In the collisions described in this thesis, the neutral is effectively stationary before interactions so, in reality, the velocity vector V_Y would be much smaller than shown in Figure 4.3. However, to make the diagram more understandable, V_Y has been increased.

4.4 Collision cross section¹²

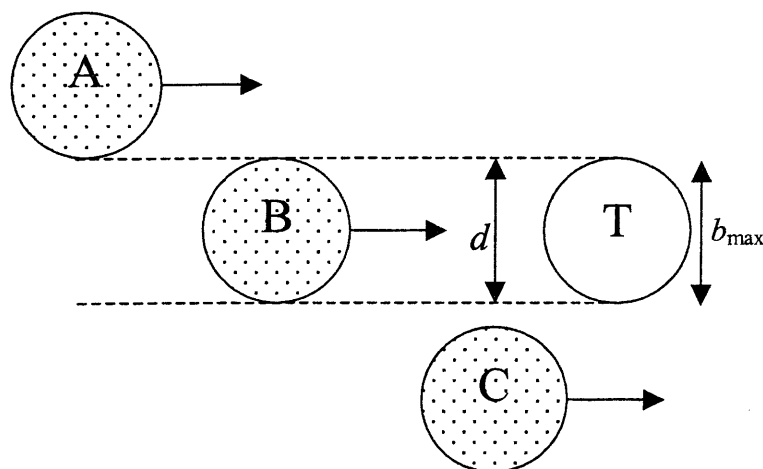


Figure 4.4 A diagrammatic representation of colliding bodies. For a collision to occur, a colliding body must be within the limits labelled d . Bodies A and B will collide with T but C will not.

In order that two chemical species may react, they must first come within a close enough proximity of each other. If the assumption is made that the reactants are hard spheres of diameter d , then they must first collide before a chemical reaction may proceed. From figure 4.4, we can see that, before collision, one body must enter the limits marked d . At the point of collision, the distance between the centres of the two species is equal to d . A collision is said to have occurred if the centre of one species enters a sphere of radius d around the second species. Hence, the collision cross section is determined by the physical size of the two colliding species. This collision cross section σ_c may be defined as the constant of proportionality in the relationship

$$\frac{1}{\lambda} = \sigma_c n_b \quad (4.19)$$

where λ is the mean free path and n_b is the number density of the collision partner. By increasing σ_c , we decrease the mean free path and increase the chances of a collision occurring.

However, real molecules (or ions) are not hard spheres. It is therefore more realistic to consider collisions between molecular species in terms of their impact parameter.

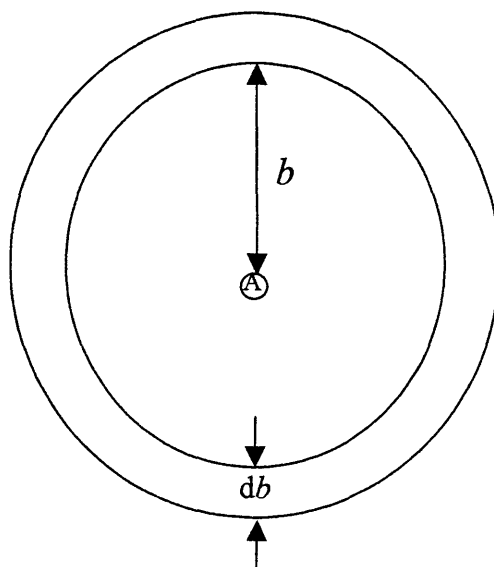


Figure 4.5 A diagram showing the cross sectional area presented for collisions with A that have an impact parameter between b and $b + db$.

The impact parameter is the distance of closest approach of the two species in the absence of any intermolecular interactions between them. If the incident ion has trajectories with an impact parameter in the range b to $b+db$, then the ions must pass through an annular volume of radius b and thickness db (Figure 4.5). Any species with a trajectory inside the area of the annulus will collide with the target species. The collision cross section may be given as

$$d\sigma_c = 2\pi b db \quad (4.20)$$

Integrating this within the range 0 to b_{max} , that is, for all values of impact parameter up to a maximum (b_{max}) that will result in a collision gives

$$\sigma_c = \pi b_{max}^2 \quad (4.21)$$

In the case of the hard sphere model, $b_{max} = d$. Therefore, the collision cross section for the hard spheres is

$$\sigma_c = \pi d^2 \quad (4.22)$$

However, when considering real dication neutral collisions, we must appreciate that not every collision will result in a reaction. In order to understand real collisions, we require some coefficient to account for the actual likelihood of a reaction taking place. This reaction cross section is discussed below.

4.5 Reaction cross section

The collision cross section determines whether two species will collide, or more specifically, whether two bodies will come into close enough proximity to undergo some reaction process. However, it is clear that not every 'collision' will result in a chemical reaction occurring. Whether or not a chemical reaction does indeed take place during a collision is dependent on the reaction cross section σ_{rxn} . This quantity

σ_{rxn} , is smaller than the collision cross section σ_c as not all collisions will result in a reaction occurring.

If we consider a cell filled with a collision gas B of number density N_B , an incident beam of reactant particles, A and number density N_A , passing through that cell will undergo a loss in flux according to

$$-\left(\frac{dI_A}{dx}\right) = k(v)N_A N_B = I_A(x)N_B \sigma_{rxn} \quad (4.23)$$

where $I_A(x)$ is the intensity of the beam A at position x and $k(v)$ is the reaction rate constant where

$$k(v) = v\sigma_{rxn} \quad (4.24)$$

Clearly, $\sigma_c \geq \sigma_{rxn}$ as not every collision will result in a reaction. The likelihood that a collision will lead to a reaction may be defined as a function of the opacity function $P(b)$. That is, the fraction of collisions having impact parameter b , that will result in a reaction. Therefore, $0 \leq P(b) \leq 1$.

At impact parameters larger than b_{max} , reactions will not occur. Therefore, $P(b)$ is zero if the impact parameter is larger than b_{max} . Incorporating this opacity function $P(b)$ into the equation for the collision cross section gives us a relationship for the reaction cross section σ_{rxn} where

$$d\sigma_{rxn} = 2\pi b(P)b db \quad (4.25)$$

and

$$\sigma_{rxn} = 2\pi \int_0^{b_{max}} bP(b)db \quad (4.26)$$

The opacity function $P(b)$ is P if $b \leq b_{max}$ and 0 if $b > b_{max}$

4.6 Scattering

In this thesis, the reactions described are dominated by electron transfer. That is, a single electron transferring from the neutral to the dication. Such electron transfer processes involve forward scattering, in the centre of mass frame, of the monocation derived from the dication.¹³ This forward scattering arises as a result of the impact parameter at which electron transfer may occur. When a reaction may occur at large interspecies separation, that is where b_{max} is large, then reactions are dominated by forward scattering. For example, in the case of the reaction



Following the reaction, KBr proceeds along on much the same path as the reactant K and H proceeds along a similar path to that of HBr. In short, K “strips” away Br from HBr. This mechanism is sometimes referred to as spectator stripping. In the same way, X^{2+} strips away an electron from Y at about 3-6 Å.

Conversely, for reactions which occur at small interspecies separations, backward scattering dominates. In the case of the reaction



I transfers from CH_3I to K and KI rebounds back in the direction from where it originated. This mechanism is sometimes known as the rebound mechanism.

4.7 Conclusions

The Landau-Zener reaction window model and its application have been discussed. Also reviewed here is the centre of mass reference frame and the collision and reaction cross sections. All of these theoretical aspects of reaction dynamics are important in understanding the bimolecular reactivity of molecular dication.

4.8 References

- 1 S. D. Price, M. Manning and S. R. Leone, *J. Am. Chem. Soc.* **116** (1994) 8673-8680
- 2 W. Lu, P. Tosi and D. Bassi, *J. Chem. Phys.* **112** (2000) 8648
- 3 Z. Herman, J. Zabka, Z. Dolejsek and M. Farnik, *Int. J. Mass Spectrom.* **192** (1999) 191-203
- 4 L. Landau, *Phys. Z. Sowjetunion.* **2** (1932) 26
- 5 C. Zener, *Proc. Roy. Soc. Lond. Ser. A.* **137** (1932) 696
- 6 R. E. Olson, F. T. Smith and E. Bauer, *App. Opt.* **10** (1971) 1848
- 7 M. Manning, S. D. Price and S. R. Leone, *J. Chem. Phys.* **99** (1993) 8695-8704
- 8 S. A. Rogers, S. D. Price and S. R. Leone, *J. Chem. Phys.* **98** (1993) 280-289
- 9 S. D. Price, S. A. Rogers and S. R. Leone, *J. Chem. Phys.* **98** (1993) 9455-9465
- 10 S. D. Price, *J. Chem. Soc. Faraday Trans.* **93** (1997) 2451-2460
- 11 R. D. Levine and R. B. Bernstein, *Molecular Reaction Dynamics and Chemical Reactivity*, (1987)
- 12 P. W. Atkins, *Physical Chemistry*, (1998)
- 13 Z. Dolejsek, M. Farnik and Z. Herman, *Chem. Phys. Lett.* **235** (1995) 99-104

Chapter 5



5.1 Introduction

The absolute partial ionisation cross section for forming CF_2^{2+} from CF_4 has been measured by electron impact ionisation, to be 0.059 \AA^2 .¹ In addition, Husak *et al.*² calculated the heat of formation of CF_2^{2+} to be 29.88 eV .²

It has been shown that the bimolecular reactivity of CF_2^{2+} , as with many other dicationic neutral collision systems, is dominated mainly by electron transfer reactivity.^{3,4} However, the bond-forming reactivity of CF_2^{2+} has also been observed and studied intensively, largely due to the ease of forming high quality beams of this dication. Initially, Price *et al.*⁵ observed the presence of DCF_2^+ following collisions between CF_2^{2+} and D_2 . Subsequently, the angular scattering in the collision system $\text{CF}_2^{2+} + \text{D}_2$ was studied by Dolejšek and co-workers,⁶ revealing that the DCF_2^+ product is largely forward scattered. Following the success of these studies, intermolecular and intramolecular isotope effects have been studied following collisions of CF_2^{2+} with H_2 , HD and D_2 .^{7,8} The experiments involving HD as the neutral collision partner showed a strong preference for the formation of the deuterated adduct DCF_2^+ over HCF_2^+ . It was first suggested that this preference for the formation of the deuterated adduct may arise via an orientational isotope effect. However, more recent experiments measuring intramolecular isotope effects in other dicationic collision systems and more detailed understanding of the reaction mechanisms indicate that the preference for the deuterated product may be accounted for by statistical effects.⁹

Given the considerable reactivity of CF_2^{2+} with H_2 , we have investigated the reactivity exhibited following collisions of CF_2^{2+} with other hydrogen containing

molecules. This chapter reports the results of an experimental study of the reactivity between CF_2^{2+} and H_2X ($\text{X} = \text{O}, \text{S}$). Experiments were performed at collision energies between 3 and 14 eV in the laboratory frame. Both of these collision systems exhibit energy transfer and electron transfer processes, together with previously unobserved bond forming reactions producing OCF^+ and SCF^+ . The electron transfer reactivity is discussed in terms of the Landau-Zener reaction window model.

5.2 Results

Mass spectra were recorded following collisions between CF_2^{2+} and H_2O at collision energies between 0.79 eV and 3.71 eV in the centre of mass frame (3 to 14 eV in the laboratory frame). For collisions between CF_2^{2+} and H_2S , mass spectra were recorded between 1.6 and 5.6 eV in the centre of mass frame (4 to 14 eV in the laboratory frame). Representative ion intensity ratios are listed in Table 5.1 and Table 5.2.

5.2.1 Assignment of product ions

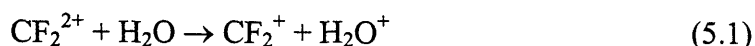
As has been shown in previous work, the precise identities of the product ions formed in the collision system $\text{CF}_2^{2+} + \text{H}_2\text{X}$ ($\text{X} = \text{O}, \text{S}$) can offer a great deal of information regarding the reactivity that is occurring.

H_2O^+	CF^+	OCF^+	CF_2^+	C^+	H^+	F^+
49000	78700	3590	45300	4	305	225
(1600)	(8910)	(65)	(5940)	(26)	(12)	(230)

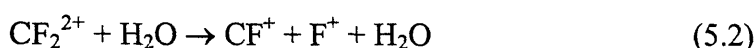
Table 5.1 Representative product ion intensity ratios (R_{real}) from one set of mass spectra recorded following collisions of CF_2^{2+} with H_2O at a collision energy of 7 eV in the laboratory frame. The intensity ratio R_{real} is determined using equation 3.23 as explained in chapter 3 and outlined later in this chapter. The values in parenthesis indicate one standard deviation in the values of R_{real}

5.2.2 CF₂²⁺ and H₂O

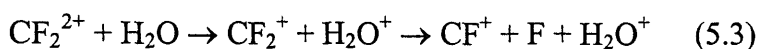
From Table 5.1, we can see that H₂O⁺ and CF₂⁺ are formed from this collision system. Both of these ions can only arise as a result of a non-dissociative electron transfer reaction



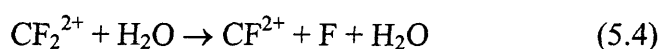
The CF⁺ we observe may be formed via one of two routes. Firstly, CF₂²⁺ may undergo collision-induced charge separation



to yield CF⁺ and F⁺, or, secondly, dissociative electron transfer



may occur to yield CF⁺ and F. However, after impurity ion correction, no F⁺ ions are detected which result from bimolecular reactions (Table 5.1), which confirms that the CF⁺ ions we detect are formed by dissociative electron transfer (equation 5.3). The detection of OCF⁺ following collisions of CF₂²⁺ with H₂O clearly shows the occurrence of a bond forming reaction. The other products formed along with OCF⁺ could be H₂F⁺, HF⁺ + H or HF + H⁺. No HF⁺ and H₂F⁺ ions are observed in our mass spectra. However, H⁺ is detected indicating that the chemical reaction forms OCF⁺ and H⁺ together with neutral H and F atoms or HF. The inequality in the size of the OCF⁺ and H⁺ signals (Table 5.1) is readily attributed, as has been described before,^{10,11} to the fact that H⁺ is very light and is formed with a high laboratory frame velocity, causing its detection efficiency to be significantly reduced in our experimental arrangement. The proposed mechanism for this bond forming reaction is discussed later in the chapter. In agreement with previous investigations of the reactivity of CF₂²⁺, no collision-induced neutral loss



is observed in this collision system. The production of OH^+ from H_2O^+ cannot be entirely eliminated as this area of the mass spectrum is partially obscured by the wings of the H_2O^+ signal. However, the intensity of any OH^+ signal, formed by dissociative electron transfer, is certainly not greater than ca. 5% of the H_2O^+ signal. Note that C^+ ions are not detected following collisions of CF_2^{2+} with H_2O .

H_2S^+	CF^+	SCF^+	CF_2^+	C^+	H^+	F^+
20600	59800	267	6070	230	365	-5
(212)	(2440)	(8)	(429)	(93)	(423)	(37)

Table 5.2 Representative product ion intensity ratios (R_{real}) from one set of mass spectra recorded following collisions of CF_2^{2+} with H_2S at a collision energy of 7 eV in the laboratory frame. The values in parenthesis indicate one standard deviation in the values of R_{real}

5.2.3 $\text{CF}_2^{2+} + \text{H}_2\text{S}$.

Table 5.2 shows that, following collisions of CF_2^{2+} with H_2S , we observe product ions analogous to those detected following reactions between CF_2^{2+} and H_2O (Table 5.1). Thus, CF_2^+ , CF^+ and H_2S^+ are formed by electron transfer and SCF^+ is also detected. However, the SCF^+ signal is considerably weaker than the corresponding OCF^+ signal in $\text{CF}_2^{2+} + \text{H}_2\text{O}$, the R_{real} values for the formation of OCF^+ being approximately ten times that for SCF^+ . By comparison with the $\text{CF}_2^{2+}/\text{H}_2\text{O}$ collision system, we would expect H^+ to be the partner ion produced together with SCF^+ , in the $\text{CF}_2^{2+}/\text{H}_2\text{S}$ collision system. However (Table 5.2) no “real” H^+ signals are observed in our mass spectra. However, since the SCF^+ signal is so weak, the intensity of the accompanying H^+ ions, which are less efficiently detected, will lie below our detection limit. Signals corresponding to the C^+ ions are also present in the mass spectra from the $\text{CF}_2^{2+}/\text{H}_2\text{S}$ system. Any signals corresponding to HS^+ and S^+ are not visible in our mass spectra. However, their presence at a level below 5%

of the H_2S^+ signal cannot be excluded, as the H_2S^+ peak is quite broad and may obscure weak signals at m/z values of 33 and 32.

5.3 Determination of integral reaction cross sections

Using the methodology described in Chapter 3, integral reaction cross sections, in arbitrary units, can be determined for the formation of CF_2^+ , CF^+ and XCF^+ from collisions of CF_2^{2+} with H_2X . To determine these integral reaction cross sections we require the translational energies of the product ions across the source region perpendicular to the axis of the TOFMS. These energies are needed to determine v_j and, L_j , the velocity of product ion j across the source region of the TOFMS and the length of the source region imaged onto the detector for reaction channel j . These two parameters allow us to calculate R_{real} , the real ratio of a product ion to the reactant dication intensity. R_{real} is then used to determine the integral reaction cross section for a particular reaction channel. The method for extracting integral reaction cross sections from our data is detailed in chapter 3.

The energies of the products of the electron transfer reactions of molecular dications have been determined before.^{3,4,12,13} These previous investigations indicate that the kinetic energy release (KER) experienced by the two resultant monocations in non-dissociative electron transfer reactions is, on average, around 7 eV. Thus, to estimate the velocity of the CF_2^+ product across the source region of the TOFMS we use a representative KER of 7 eV, and assume that the dynamics of the electron transfer reaction are dominated by forward scattering of the monocation derived from the dication, as has been observed in all the angularly resolved studies of dication electron transfer processes to date.^{3,4,12,13} Using an estimated value for the KER following electron transfer is unavoidable, as the kinetic energy release in the reaction of CF_2^{2+} with H_2O has not been measured. However, the ratios of the L and

ν parameters we determine for the product ion and reactant dications are not a strong function of the KER. Indeed, product ion intensities corrected using this methodology agree well with those measured in other laboratories.^{3,7,8} Once ν is determined then L can be derived from the geometry of the TOFMS.⁸

For the dissociative electron transfer channel forming CF^+ , we assume that the excited CF_2^{+*} formed by the initial electron transfer dissociates after it has effectively left the electric field of the H_2O^+ ion. Such behaviour has been observed experimentally for other dissociative electron transfer reactions.¹³ If we assume that the additional velocity imparted to the CF^+ ion by the fragmentation of CF_2^{+*} is negligible, then the CF^+ will be travelling with the same velocity as its CF_2^+ precursor, which we have estimated above. Hence, we have the information we require to determine the σ_j^+ values for the electron transfer channels, which are displayed in Figure 5.3.

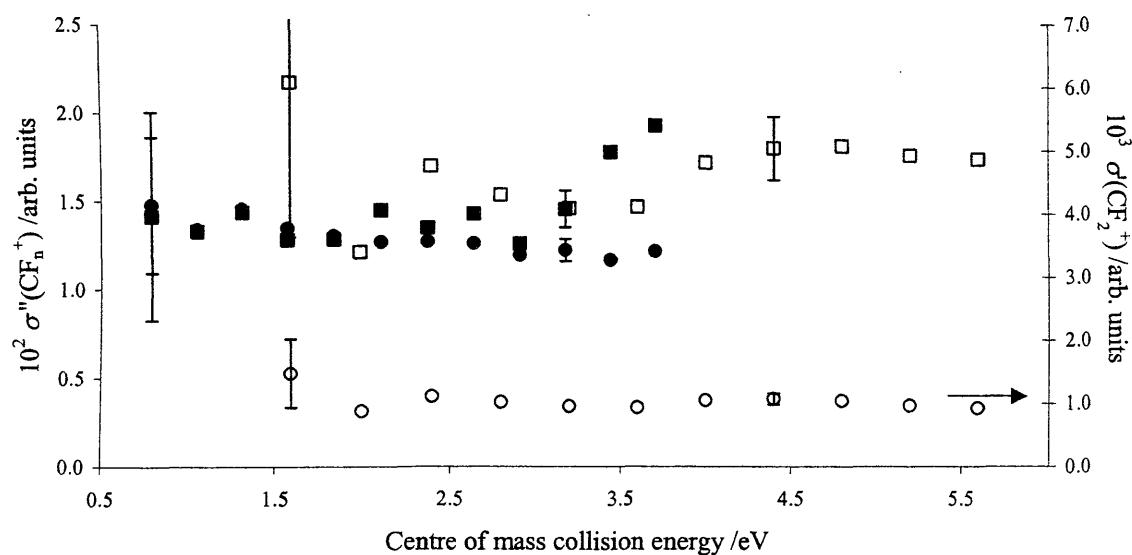


Figure 5.3 Reaction cross section in arbitrary units as a function of centre of mass collision energy for CF_2^+ (■) and CF^+ (●) from $\text{CF}_2^{2+} + \text{H}_2\text{O}$ and CF_2^+ (○) and CF^+ (□) from $\text{CF}_2^{2+} + \text{H}_2\text{S}$. representative error bars are shown. The data for the formation of CF_2^+ from $\text{CF}_2^{2+} + \text{H}_2\text{S}$ should be read on the right hand axis.

For the formation of XCF^+ we assume that there is an initial fragmentation to H^+ and HXCF_2^+ with a kinetic energy release of 7 eV and that the HXCF_2^+ subsequently

dissociates to XCF^+ . Since we know the charged product accompanying the XCF^+ ion is H^+ , this mechanism is in accord with previous studies of the mechanisms of dication chemical reactions such as the theoretical studies performed by Lambert *et al.*¹⁴ and angularly resolved experiments carried out by Harper and co-workers.¹⁵ As mentioned, the mechanism for forming XCF^+ from $\text{CF}_2^{2+} + \text{H}_2\text{X}$ is discussed in detail later in this chapter. The initial charge separation in this mechanism involves the formation of a heavy and a light ion. Hence, the additional kinetic energy given to the HXCF_2^+ ion is very small and the corrections to R_{real} are small and only very weakly dependent on the collision energy and the value of the kinetic energy release we assume for the initial charge separation. The σ' values we derive for the chemical channels are presented in Figure 5.4.

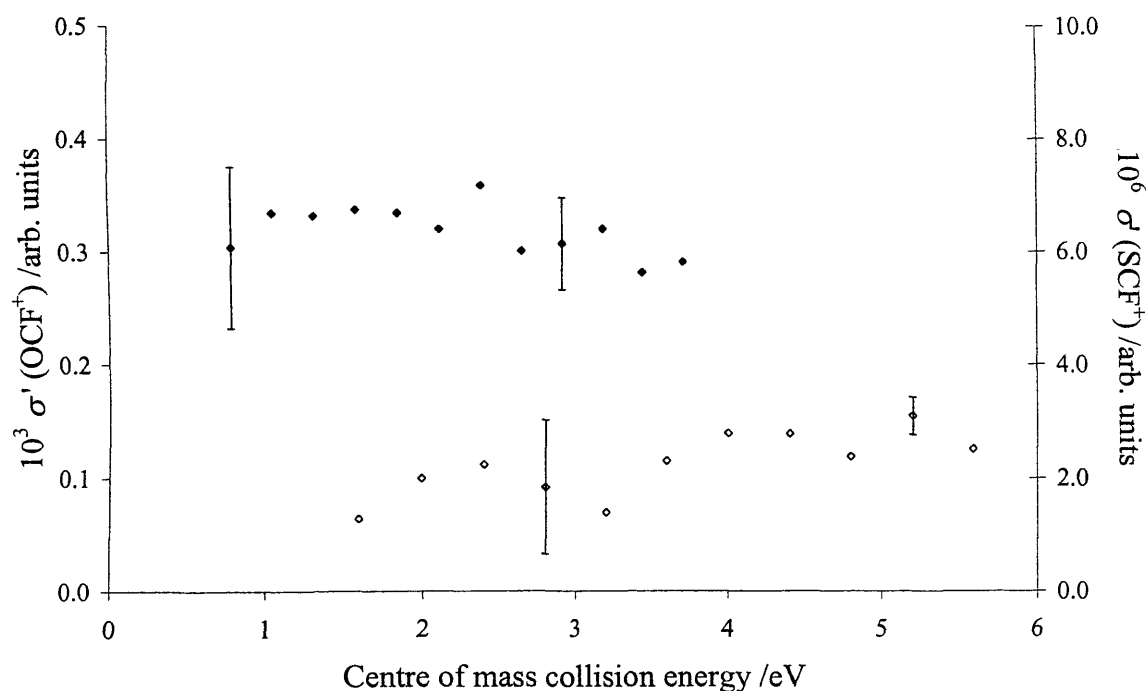


Figure 5.4 Reaction cross sections in arbitrary units as a function of centre of mass collision energy for OCF^+ (\blacklozenge) from $\text{CF}_2^{2+} + \text{H}_2\text{O}$ and SCF^+ (\diamond) from $\text{CF}_2^{2+} + \text{H}_2\text{S}$. Representative error bars are shown.

The cross sections for the electron transfer reactions (Figure 5.3) clearly show the trends revealed in the representative ion intensities given in Table 5.1 and Table 5.2. The cross sections for the formation of CF_2^+ and CF^+ are similar for the H_2O

collision system, whilst for the H₂S collision system significantly more CF⁺ is formed than CF₂⁺. In addition, we see that the cross section for forming CF⁺ from the H₂S collision system is slightly larger than for forming either CF₂⁺ or CF⁺ following collisions of CF₂²⁺ with H₂O. As has been observed for some analogous reactive systems, all the cross sections remain approximately constant over the range of collision energies investigated.¹³

The cross sections for forming OCF⁺ and SCF⁺ (Figure 5.4) show that the formation of OCF⁺ from collisions of CF₂²⁺ with H₂O is distinctly more probable than the formation of SCF⁺ from collisions of CF₂²⁺ with H₂S. In addition, over the range of collision energies studied the yield of OCF⁺ seems constant, whereas, within the error bars which are proportionally larger for the small SCF⁺ signal, the SCF⁺ yield appears to fall with decreasing collision energy. To rationalise the magnitudes of the cross sections of the electron transfer reactions of CF₂²⁺ with H₂X we now attempt to model these processes using a model based on the Landau–Zener theory.^{16,17}

For the reaction window algorithm to be employed successfully, the exothermicities of the transitions between the ground states of CF₂²⁺ and H₂X and the accessible electronic states of the product ions formed following an electron transfer reaction are required. These exothermicities are listed in Table 5.5 and Table 5.6 and have been principally obtained from thermodynamic tables.^{18,19} The heat of formation of CF₂²⁺ used in our calculations (29.88 eV) is a value recently calculated by Hrusak *et al.*² and the relative energies of the excited states of the monocations used to calculate the exothermicities given in Table 5.5 and Table 5.6 have been determined from the relevant photoelectron spectra.²⁰⁻²²

Electronic state of CF ₂ ⁺ product	Electronic state of H ₂ O ⁺ product					
	X (→ H ₂ O ⁺)		A (→ H ₂ O ⁺)		B (→ H ₂ O ⁺ , OH ⁺ , H ⁺)	
	ΔH/eV	σ	ΔH/eV	σ	ΔH/eV	σ
6a ₁ ⁻¹ (→CF ₂ ⁺)	7.7	0	5.7	0	1.8	0.3
4b ₂ ⁻¹ (→CF ⁺)	3.6	22.5	1.6	0	-2.3	0
1a ₂ ⁻¹ (→CF ⁺)	2.6	8.9	0.6	0	-3.3	0
5a ₁ ⁻¹ (→CF ⁺)	0.83	0	-1.2	0	-5.1	0
1b ₁ ⁻¹ (→CF ⁺)	-0.9	0	-2.9	0	-6.8	0
3b ₂ ⁻¹ (→C ⁺)	-2.2	0	-4.2	0	-8.1	0
4a ₁ ⁻¹ (→C ⁺)	-4.0	0	-6.0	0	-9.9	0
6a ₁ ⁻¹ (→CF ₂ ⁺) ^a	4.7	1.5	2.7	8.9	-1.2	0

^a The final row of the table gives the exothermicity and cross section for populating a vibrationally excited level of the stable electronic ground state of CF₂⁺ at the equilibrium linear geometry of the reactant dication

Table 5.5 Exothermicities ΔH and calculated reaction cross sections (σ /Å²) for forming the various possible combinations of electronic states of the CF₂⁺ and H₂O⁺ product ions following single electron transfer between CF₂²⁺ and H₂O at a laboratory frame collision energy of 8 eV.

Electronic state of CF ₂ ⁺ product	Electronic state of H ₂ O ⁺ product					
	X (→ H ₂ S ⁺)		A (→ H ₂ S ⁺ , S ⁺)		B (→ HS ⁺)	
	ΔH/eV	σ	ΔH/eV	σ	ΔH/eV	σ
6a ₁ ⁻¹ (→CF ₂ ⁺)	9.9	0	7.0	0.4	4.9	5.0
4b ₂ ⁻¹ (→CF ⁺)	5.8	1.3	2.9	21.3	-0.8	0
1a ₂ ⁻¹ (→CF ⁺)	4.8	5.5	1.9	0.6	-0.2	0
5a ₁ ⁻¹ (→CF ⁺)	3.0	27.0	0.1	0	-2.0	0
1b ₁ ⁻¹ (→CF ⁺)	1.3	0	-1.6	0	-3.7	0
3b ₂ ⁻¹ (→C ⁺)	0.0	0	-2.9	0	-5.0	0
4a ₁ ⁻¹ (→C ⁺)	-1.8	0	-4.7	0	-6.8	0
6a ₁ ⁻¹ (→CF ₂ ⁺) ^a	6.9	0.4	4.0	18.2	1.9	0.5

^a The final row of the table gives the exothermicity and cross section for populating a vibrationally excited level of the stable electronic ground state of CF₂⁺ at the equilibrium linear geometry of the reactant dication

Table 5.6 Exothermicities ΔH and calculated reaction cross sections (σ /Å²) for forming the various possible combinations of electronic states of the CF₂⁺ and H₂S⁺ product ions following single electron transfer between CF₂²⁺ and H₂S at a laboratory frame collision energy of 8 eV.

The reaction window model tells us in which electronic states the initial products of electron transfer ($\text{CF}_2^+ + \text{H}_2\text{X}^+$) are likely to be formed, but to understand the fragmentation pathways of these primary products, a knowledge of the stability of their different electronic states is necessary. Photoelectron-photoion coincidence (PEPICO) studies of H_2S and H_2O provide the details of how the electronic states of H_2X^+ behave.^{23,24} The ground electronic states of both H_2O^+ and H_2S^+ are stable as they lie well below their first dissociation asymptotes. For H_2S^+ , the dissociation limit for forming $\text{S}^+ + \text{H}_2$ lies 3.0 eV above the ionic ground state. The first excited electronic state (A) of H_2S^+ lies just below this asymptote with its higher vibrational levels lying above it. Hence, the higher vibrational levels of the A state of H_2S^+ will dissociate to $\text{S}^+ + \text{H}_2$, whereas lower vibrational levels will remain undissociated. The second excited state (B) of H_2S^+ lies just above the dissociation limit $\text{H}_2\text{S}^+ \rightarrow \text{H} + \text{HS}^+$ (3.8 eV with respect to the ground states of H_2S^+) and dissociates to these products. The dissociation limits $\text{H}_2\text{S}^+ \rightarrow \text{S}^+ + 2\text{H}$ and $\text{H}_2\text{S}^+ \rightarrow \text{S} + \text{H}_2^+$ lie 7.5 eV and 8.1 eV above the ground state of H_2S^+ . It is assumed that any electronic states of H_2S^+ formed with these high internal energies will yield S^+ and H_2^+ ions. The first electronic excited state (A) of H_2O^+ lies well below the dissociation limit for forming $\text{OH}^+ + \text{H}$ (5.6 eV with respect to the ground state). The second excited state (B) of H_2O^+ also lies just below this dissociation limit. However, higher vibrational levels of the B state lie above the dissociation limit and their population results in the formation of $\text{H} + \text{OH}^+$. Significantly higher vibrational levels of the B state lie above the dissociation limit to $\text{H}^+ + \text{OH}$ (6.2 eV) and dissociate to these products.

No PEPICO data for the fragmentation of CF_2^+ is available in the literature, due to the fact that CF_2 is an unstable molecule. Consequently, to predict how the various electronic states of CF_2^+ will fragment, we must fall back on considering the relative

energetics of the electronic states of CF_2^+ with respect to the various dissociation asymptotes. An experimental photoelectron spectrum of CF_2 showing the population of the low-lying states of CF_2^+ is available, and the electronic state energies of CF_2^+ have also been determined.²⁰ Using the adiabatic ionization potentials and heats of formation,^{18,19} we calculate that the dissociation limit for $\text{CF}^+ + \text{F}$ lies ca. 3.04 eV above the ground state of CF_2^+ . We note that the difference (≈ 0.2 eV) between this value and previous estimations is due to the recently revised heat of formation of CF_2 .¹⁹ As the first excited electronic state²⁰ of CF_2^+ lies approximately 4.1 eV above the ground state of CF_2^+ , it is reasonable to suppose that only the ground electronic state of CF_2^+ will remain undissociated. This conclusion is supported by the fact that the peaks in the photoelectron spectrum corresponding to the population of the first and second excited states of CF_2^+ do not possess any resolved vibrational fine structure, indicating a short lifetime due to predissociation.²⁰

The dissociation limit for forming $\text{F}_2 + \text{C}^+$ from CF_2^+ lies 9.2 eV above the ground state of CF_2^+ . The $\text{CF}_2^+ [3b_2^{-1}]$ state lies directly above this dissociation limit (9.9 eV above the ground state of CF_2^+) so can dissociate to these products. The dissociation limit for $\text{CF}_2^+ \rightarrow \text{C}^+ + 2\text{F}$ lies 10.8 eV above the ground state of CF_2^+ . Of the known states of CF_2^+ , only the $4a_1^{-1}$ excited state (11.7 eV above the ground state) lies above this limit, although, of course, higher lying electronic states will exist. Hence, we will take the behaviour of the $4a_1^{-1}$ state as representative of such high energy states. The $\text{CF}_2^+ [4a_1^{-1}]$ state also lies above the dissociation asymptote $\text{CF}_2^+ \rightarrow \text{CF} + \text{F}^+$ (11.4 eV) and so may also dissociate to $\text{CF} + \text{F}^+$. However, in previous investigations of the electron transfer reactivity of CF_2^{2+} , no formation of F^+ is observed, as is the case in the present study. Hence, there must be some dynamical

restriction to the formation of F^+ and we assume that the $4a_1^{-1}$, and higher, states of CF_2^+ do not dissociate to form $F^+ + CF$ but instead form $C^+ + 2F$.

Given the above data we can now use the Landau–Zener algorithm to calculate the probability of forming the various combinations of the electronic states of the primary product ions ($CF_2^+ + H_2X^+$) in an electron transfer reactions between CF_2^{2+} and H_2X . To calculate the reaction exothermicities for populating the product asymptotes involving electronically excited monocations we use excitation energies derived from photoelectron spectra.^{20,22,25} We also know from the information given above the stability and fate of these various electronic states. Hence, we can predict the product ions we should observe in our mass spectra. These predictions are summarized in Table 5.5 and Table 5.6 which show the calculated electron transfer reaction cross sections for populating, and the final ionic products expected from, each possible combination of the electronic states of $CF_2^+ + H_2X^+$.

As described above, it is clear from our product ion spectra that the principal product ion derived from the reactant H_2O molecule is H_2O^+ . This is in good agreement with the results of our calculations (Table 5.3) which indicate that electron transfer reactions should principally populate the X and A states of H_2O^+ which are stable. However, from Table 5.5 it is also apparent that the calculated cross section for populating the vibrationless level of the ground electronic state of CF_2^+ is close to zero. Since the ground state of CF_2^+ is the only stable electronic state, our calculations would then predict a very large $CF^+ : CF_2^+$ intensity ratio in the product ion mass spectra. This is clearly not the case (Table 5.1 and Figure 5.3) as experimentally we observe a CF^+ to CF_2^+ intensity ratio of approximate unity.

The explanation for this disagreement with the predictions of the Landau–Zener model and the experimental results for the reactions of polyatomic dications has been

described before.²⁶ The problem is that the energetics for CF_2^+ we use to calculate the reaction exothermicities are obtained from photoelectron spectroscopy (PES), from vertical transitions at the geometry of the neutral molecule. Conversely, if we assume, as has been verified experimentally,²⁷ that vertical transitions are usually dominant in the electron transfer process at our collision energies, then CF_2^{2+} accepts an electron to form CF_2^+ at the linear geometry of the dication, which is a different part of the potential energy surface to that for which we have energetic information from photoelectron spectra. Thus, the electron transfer process is certain to favour the formation of vibrationally excited, rather than vibrationless, CF_2^+ ions. *Ab initio* calculations have been performed¹⁰ to determine the energy of CF_2^+ when it adopts the linear geometry of CF_2^{2+} . For the ground state geometries of both the monocation and the dication the results of Hrusak *et al*² were reproduced satisfactorily. Specifically, for the dication a minimum of $D_{\infty h}$ symmetry with a bond length of 1.152 Å was calculated, and for the monocation a C_{2v} ground state geometry with $r(\text{C-F}) = 1.217$ Å and a bond angle of 125.0° was calculated. The difference in the calculated energetics at these two points results in a calculated adiabatic second ionization energy of 20.7 eV in good agreement with experiment (20.6eV) and previous calculations (20.4 eV).²

Calculating the energy of CF_2^+ at the geometry of the equilibrium structure of CF_2^{2+} indicates that the Franck–Condon zone for populating the monocation from the equilibrium geometry of the dication lies ca. 3.0 eV above the vibrationless electronic ground state of CF_2^+ . Thus, when we include these geometric effects we predict the exothermicity for populating the stable ground state of CF_2^+ in a vertical transition from CF_2^{2+} will be 3.0 eV smaller than for populating the vibrationless ground state of CF_2^+ . Obviously, this number is only an estimate of the amount of

vibrational excitation that will be deposited in the ground electronic state of CF_2^+ , as there is the distinct possibility of vibrational excitation in the reactant dication which will affect the geometry of the CF_2^+ ion that is formed. The final line of Table 5.5 gives the calculated electron-transfer cross sections for populating the electronic ground state of CF_2^+ with 3.0 eV of vibrational excitation. We see that, when allowance is made for the difference in geometries of the dication and monocation, we predict a significant cross section for populating the electronic ground state of CF_2^+ together with both the X and A electronic states of H_2O^+ . We then predict a comparable cross section for forming CF^+ and CF_2^+ in qualitative agreement with our experimentally determined cross sections. Quantitatively, our calculations seem to slightly overestimate the probability of forming CF^+ , if processes populating the X and A states of H_2O^+ are equally probable in the electron transfer process. Satisfyingly, our calculations also indicate that we should not populate and CF_2^+ states lying above the dissociation limit to C^+ , again in good agreement with our experimental observations.

The results for our Landau–Zener calculations of the electron transfer cross sections for $\text{CF}_2^{2+} + \text{H}_2\text{S}$ are presented in Table 5.6. As for the $\text{CF}_2^{2+}/\text{H}_2\text{O}$ collision system, Table 5.6 includes calculations performed for forming the vibrationally excited electronic ground state of CF_2^+ in a vertical transition at the dication geometry. Our experiments indicate that we form predominantly H_2S^+ from the neutral reactant following the transfer of an electron from H_2S to CF_2^{2+} . This observation indicates, given the stability of the H_2S^+ electronic states described above, that we principally populate the X state of H_2S^+ and perhaps lower vibrational levels of the A state. Again, as with the H_2O system this is confirmed by our Landau–Zener calculations which predict that electron transfer processes which populate the B state of H_2S^+

have low cross sections. The calculations also predict that the vast majority of the CF_2^+ states populated will be those which dissociate to CF^+ . This is because, due to the lower ionisation potential of H_2S than H_2O , the electron transfer processes in the $\text{CF}_2^{2+}/\text{H}_2\text{S}$ system favour the population of higher lying electronic states of CF_2^+ . Thus, the calculations predict that the vast majority of favoured CF_2^+ states populated will be those which dissociate to CF^+ , in contrast to our predictions for the $\text{CF}_2^{2+}/\text{H}_2\text{O}$ system. Again this is in agreement with experimental observations which show that the formation of CF_2^+ by electron transfer is more likely in collisions of CF_2^{2+} with H_2O than with H_2S . The calculations also indicate that the formation of stable CF_2^+ ions following collisions of CF_2^{2+} with H_2S in this system should be dominated by the population of vibrationally excited levels of the CF_2^+ ground state together with H_2S^+ in its A state.

A potential disagreement between the calculations and the experimental ion intensities is then apparent. Specifically, if we are populating the A state of H_2S^+ why do we not observe S^+ as a product ion? Perhaps the $\text{H}_2\text{S} \rightarrow \text{H}_2\text{S}^+$ process, when induced by electron transfer rather than photo-absorption populates the low vibrational levels of the A state more heavily than photoionization. In other words, there is perhaps a distinct non-vertical nature to the electron transfer processes populating the A state of H_2S^+ . Indications of such non-vertical transitions in electron transfer reactions have been observed before in encounters at low collision energies.^{27,28}

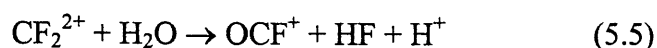
To understand the energy dependence of the electron transfer cross sections, the reaction window calculations were carried out at a laboratory collision energy of 3 eV, in addition to the data presented in Table 5.3 and Table 5.4 which is at laboratory collision energy of 8 eV. The calculated ratios of $\sigma_{\text{calc}} [\text{CF}_2^+]: \sigma_{\text{calc}} [\text{CF}^+]$

were not found to vary significantly with collision energy, in agreement with experimental observations.

5.4 Bond-forming reactions

Both of the collision systems exhibit analogous bond forming reactivity, resulting in the generation of an XCF^+ product. Obviously these reactive pathways, which involve considerable chemical rearrangement, may well be considerably more complex than the more extensively investigated chemical reactions of dications with H_2 . The degree of chemical rearrangement required to form the chemical products (XCF^+) certainly suggests that a collision complex must be involved. The cross section for forming OCF^+ from CF_2^{2+}/H_2O is markedly larger than that for the formation of SCF^+ from CF_2^{2+}/H_2S , but is still significantly smaller than the yields of the electron transfer reactions, or the yield of chemical reaction products in dication/ H_2 collision systems.^{3,4,7-9,29} Similar conclusions have been drawn for the formation of $HNCF^+$ from collisions of CF_2^{2+} with NH_3 .³⁰ Indeed, the formation of $HNCF^+$ matches the chemical reactivity we observe in the CF_2^{2+}/H_2X collision systems if $X = NH$. The low yield of these chemical reactions also points to a complex reaction pathway, involving considerable rearrangement of a collision complex. The yield of OCF^+ appears constant (Figure 5.5) over the collision energy range investigated, with no evidence of a threshold apparent. However, the yield of SCF^+ , despite more scatter on the data points due to the weaker ion signals, appears to be falling with decreasing collision energy. Clearly, theoretical calculations are required in order to rationalise the experimentally observed energy dependence.

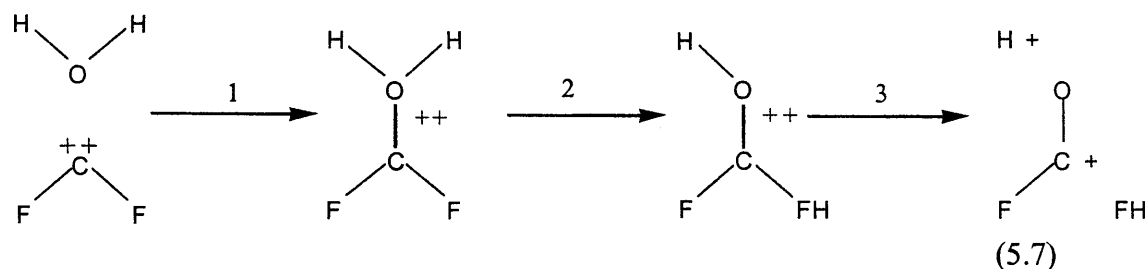
Lambert and co workers¹⁴ have shown, using *ab initio* calculations, that the bond forming process



proceeds via a similar mechanism to that proposed by Mrazek *et al.*¹³ for



Lambert and co-workers¹⁴ proposed that the mechanism for forming OCF^+ proceeds by three steps.



Step 1 in equation (5.6) involves addition of the two reacting species to form the addition complex $\text{H}_2\text{OCF}_2^{2+}$. This addition is followed by a rearrangement (step 2) where an H atom migrates to F atom. Finally, in step 3, the complex fragments to yield OCF^+ , H^+ and HF . In addition to these findings, angularly resolved experiments¹⁵ have shown that H^+ is isotropically scattered, indicating that the complex has rotated prior to this charge separation occurring. Also, the mutual angle of separation between OCF^+ and HF is 180° , suggesting that OCF^+ and HF separate after H^+ has departed from the field of HOFCF_2^+ . These findings indicate that the final fragmentation step takes two parts, where the complex undergoes charge separation to HOFCF_2^+ and H^+ and HOFCF_2^+ then fragments to OCF^+ and neutral HF . It is reasonable to suppose that the mechanism for the formation of SCF^+ in the $\text{CF}_2^{2+}/\text{H}_2\text{S}$ collision will proceed via a similar mechanism proposed for OCF^+ in the $\text{CF}_2^{2+}/\text{H}_2\text{O}$ collision system.

5.5 Conclusions

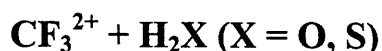
The products of electron transfer and chemical reactions following the collision of CF_2^{2+} with H_2X ($\text{X} = \text{O}, \text{S}$) have been identified by time-of-flight mass spectrometry. The integral reaction cross sections, in arbitrary units, for forming the observed CF^+ and CF_2^+ ions from electron transfer reactions, and the XCF^+ products from the chemical reactions, have been determined from the mass spectral data using a new data processing procedure. A Landau–Zener model has been employed with qualitative success to account for the relative abundances of the product ions from electron transfer. Specifically, that the electron transfer reactions favour the formation of H_2O^+ , together with approximately equal amounts of CF^+ and CF_2^+ following collisions of CF_2^{2+} with H_2O . Collisions of CF_2^{2+} with H_2S , however, favour the formation of H_2S^+ together with CF^+ . CF_2^+ and C^+ ions are formed following collisions of CF_2^{2+} with H_2S , but in significantly smaller quantities than CF^+ . The subtle differences between the predictions of the Landau–Zener model and the experimental data may be due to an increasing importance of non-vertical processes at low collision energies. With regard to the chemical reactions, the formation of OCF^+ from collisions of CF_2^{2+} with H_2O is distinctly more probable than the formation of SCF^+ from collisions of CF_2^{2+} with H_2S . The partner ion formed together with the XCF^+ ion in both these chemical channels appears to be H^+ . Such significant rearrangement in the atomic connectivity between reactants and products is strongly indicative of a mechanism involving a collision complex.

5.6 References

- 1 C. Ma, M. R. Bruce and R. A. Bonham, *Phys. Rev. A*. **44** (1991) 2921-2934
- 2 J. Hrusak, Z. Herman, N. Sandig and W. Koch, *Int. J. Mass Spectrom.* **201** (2000) 269-275
- 3 Z. Herman, J. Zabka, Z. Dolejsek and M. Farnik, *Int. J. Mass Spectrom.* **192** (1999) 191-203
- 4 Z. Herman, *Int. Rev. Phys. Chem.* **15** (1996) 299-324
- 5 S. D. Price, M. Manning and S. R. Leone, *J. Am. Chem. Soc.* **116** (1994) 8673-8680
- 6 Z. Dolejsek, M. Farnik and Z. Herman, *Chem. Phys. Lett.* **235** (1995) 99-104
- 7 K. A. Newson and S. D. Price, *Chem. Phys. Lett.* **294** (1998) 223-228
- 8 K. A. Newson and S. D. Price, *Chem. Phys. Lett.* **269** (1997) 93-98
- 9 N. Tafadar, D. Kearney and S. D. Price, *J. Chem. Phys.* **115** (2001) 8819
- 10 D. Kearney and S. D. Price, *Phys. Chem. Chem. Phys.* **5** (2003) 1575-1583
- 11 N. Lambert, D. Kearney, N. Kaltsoyannis and S. D. Price, *J. Am. Chem. Soc.* **126** (2004) 3658-3663
- 12 Z. Herman, P. Jonathan, A. G. Brenton and J. H. Beynon, *Chem. Phys. Lett.* **141** (1987) 433-442
- 13 L. Mrazek, J. Zabka, Z. Dolejsek, J. Hrusak and Z. Herman, *J. Phys. Chem. A*. **104** (2000) 7294-7303
- 14 N. Lambert, N. Kaltsoyannis and S. D. Price, *J. Chem. Phys.* **119** (2003) 1421-1425
- 15 S. M. Harper, W. P. Hu and S. D. Price, *J. Chem. Phys.* **121** (2004) Proof Copy
- 16 L. Landau, *Phys. Z. Sowjetunion.* **2** (1932) 26
- 17 C. Zener, *Proc. Roy. Soc. Lond. Ser. A*. **137** (1932) 696
- 18 S. G. Lias, J. E. Bartmess, J. F. Liebman, J. L. Holmes, R. D. Levin and W. G. Mallard, *J. Phys. Chem. Ref. Data.* **17 S1** (1988) 1-861
- 19 S. G. Lias, R. D. Levin and S. A. Kafafi, *NIST Chemistry WebBook, NIST Standard Reference Database Number 69* (<http://webbook.nist.gov>), (1998)

- 20 J. M. Dyke, L. Golob, N. Jonathan, J. Morris and M. Okuda, *J. Chem. Soc. Faraday Trans.* **70** (1974) 1828
- 21 P. Baltzer, L. Karlsson, M. Lundqvist, B. Wannberg, D. M. P. Holland and M. A. Macdonald, *Chem. Phys.* **195** (1995) 403-422
- 22 J. E. Reutt, L. S. Wang, Y. T. Lee and D. A. Shirley, *J. Chem. Phys.* **85** (1986) 6928-6939
- 23 J. H. D. Eland, *Chem. Phys.* **11** (1975) 41-47
- 24 J. H. D. Eland, *Int. J. Mass Spectrom. Ion Phys.* **31** (1979) 161-173
- 25 A. W. Potts and W. C. Price, *Proc. R. Soc. London, Ser. A.* **326** (1972) 181
- 26 P. Champkin, N. Kaltsoyannis and S. D. Price, *Int. J. Mass Spectrom. Ion Proc.* **172** (1998) 57-69
- 27 A. Ehbrecht, N. Mustafa, C. Ottinger and Z. Herman, *J. Chem. Phys.* **105** (1996) 9833-9846
- 28 E. Y. Kamber, K. Akgungor, C. P. Safvan and D. Mathur, *Chem. Phys. Lett.* **258** (1996) 336-341
- 29 N. Tafadar and S. D. Price, *Int. J. Mass Spectrom.* **223** (2003) 547
- 30 K. A. Newson, N. Tafadar and S. D. Price, *J. Chem. Soc. Faraday Trans.* **94** (1998) 2735-2740

Chapter 6



6.1 Introduction

The molecular dication CF_3^{2+} has been observed as a product of electron-impact ionisation of CF_4 .¹ This study determined the absolute partial cross section for forming CF_3^{2+} from CF_4 , at an electron energy of 100 eV, to be 0.028 \AA^2 , a cross section just less than half that for forming CF_2^{2+} from CF_4 at an electron energy of 100 eV (0.058 \AA^2). It is perhaps this difference in partial ionisation cross sections which has prompted experimentalists to study CF_2^{2+} rather than CF_3^{2+} .²⁻⁸ Masuoka and co workers⁹ used dissociative photoionisation of CF_4 to determine the appearance potentials of CF_3^{2+} and CF_2^{2+} to be 40.7 eV and 41.7 eV respectively. It has been suggested that both CF_3^{2+} and CF_2^{2+} are formed from CF_4 via the molecular dication CF_4^{2+} , which then goes on to fragment to yield the target dication of interest.¹⁰

Theoretical studies have been carried out on the structure and stability of CF_3^{2+} by a number of investigators.¹¹⁻¹⁴ In 1994, De La Vega *et al.*¹¹ used *ab initio* and density functional calculations to determine the structure of CF_3^{2+} to be of D_{3h} symmetry. However, according to Hrusak and co-workers,¹² these calculations were carried out at “rather modest levels of theory”. Instead, Hrusak *et al.* suggest that CF_3^{2+} in fact possesses C_{2v} symmetry with one long weak C-F bond and two shorter stronger C-F bonds. These findings are in agreement with the work of other groups performing similar calculations.^{13,14}

As with many dication neutral collision systems, electron transfer dominates the bimolecular reactivity of CF_3^{2+} . However, other processes do occur. For example, the consequences of energy transfer have been seen, following collisions between

CF_3^{2+} and rare gases.^{14,15} These energy transfer processes are manifested by neutral loss from the reactant dication. That is, after the collision, the dication departs with sufficient energy to fragment to CF_2^{2+} and F. Collision experiments involving collisions between CF_3^{2+} and Ar have provided an estimate of the strength of the weaker, longer bond of CF_3^{2+} by determining the threshold energy at which loss of F occurs.¹⁴ In addition, experiments on the bimolecular reactivity of CF_3^{2+} with Ar, coupled with Landau-Zener calculations, have provided information on the electron transfer reactivity of this system.¹⁴ It has been postulated that an excited state of CF_3^{2+} , lying about 5 eV above the electronic ground state, exists in a dication beam formed by electron impact ionisation. Bond-forming reactivity has been seen to occur in collisions between CF_3^{2+} and D_2 and CF_3^{2+} and O_2 . In these collision systems, DCF_2^+ and OCF^+ were formed respectively.^{7,8}

Previously in this thesis, the reactions occurring during collisions between CF_2^{2+} and H_2X ($\text{X} = \text{O}, \text{S}$) have been described.² In this Chapter, we investigate analogous processes which occur when CF_2^{2+} is replaced with CF_3^{2+} . In addition to this, by using H_2X as the neutral collision partner in place of Ar, we introduce a further level of complexity to our system as H_2X may react to produce monocationic products with vibrational excitation. That is, following collisions between CF_3^{2+} and H_2X , the neutral collision partner (or product derived from the neutral collision partner) may carry away some of the collision energy in the form of vibrational excitation.

This chapter describes the electron transfer, neutral loss and bond forming reactivity of the $\text{CF}_3^{2+} + \text{H}_2\text{X}$ ($\text{X} = \text{O}, \text{S}$) collision system. Landau-Zener calculations are used to rationalise the electron transfer channel.

6.2 Results

6.2.1 Ion Identities

Mass spectra were acquired following collisions between CF_3^{2+} and H_2O at collision energies between 0.83 and 2.90 eV in the centre of mass frame (4 to 14 eV in the laboratory frame). In the case of CF_3^{2+} and H_2S , collisions were studied within the energy range 1.65 to 4.62 eV in the centre of mass frame (5 to 14 eV in the laboratory frame). Collisions between CF_3^{2+} and H_2S were not studied at laboratory frame energies below 5 eV as a sufficiently high quality beam could not be generated. Representative product ion intensities from the two collision systems are listed in table 6.1

H^+	C^+	F^+	H_2O^+	CF_2^{2+}	CF^+	OCF^+	CF_2^+
792	19	-1047	16800	9280	10100	1250	17400
(57)	(25)	(1828)	(2470)	(584)	(1190)	(141)	(1740)

Table 6.1a Representative values of R_{real} at a laboratory frame collision energy of 7 eV for $\text{CF}_3^{2+} + \text{H}_2\text{O}$. Values in parenthesis are the uncertainty in that value.

H^+	C^+	F^+	HS^+	CF_2^{2+}	CF^+	CF_2^+	S^+
24	11	505	25900	1180	6070	2510	6750
(33)	(5)	(726)	(15100)	(104)	(2480)	(94.5)	(2490)

Table 6.1b Representative values of R_{real} at a laboratory frame collision energy of 7 eV for $\text{CF}_3^{2+} + \text{H}_2\text{S}$. Values in parenthesis are the uncertainty in that value.

6.2.2 $\text{CF}_3^{2+} + \text{H}_2\text{O}$

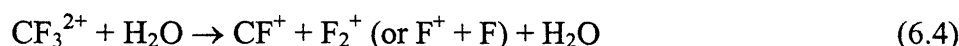
The CF_2^+ ion observed in the mass spectrum (Table 6.1a) may be formed by one of two routes. CF_3^{2+} may undergo collision induced charge separation to yield CF_2^+ along with F^+ .



However we do not observe any real F^+ signal in these experiments. This lack of a real F^+ signal shows that collision induced charge separation is not the route by which CF_2^+ is formed in this particular collision system. Instead, it is clear that CF_2^+ is formed via dissociative electron transfer where, during electron transfer, CF_3^+ is formed in some vibronically excited state which then dissociates to yield CF_2^+ .



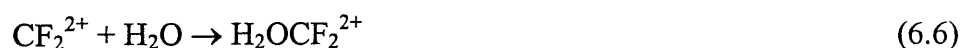
CF^+ is also observed (Table 6.1) and may also be attributed to dissociative electron transfer for similar reasons to those given for the CF_2^+ ion. If CF^+ were formed via collision induced charge separation, i.e.



then F_2^+ or F^+ would be present in the mass spectrum. As, after correction of the mass spectrum, no real F_2^+ and F^+ signals are present. Here, collision induced charge separation is not the mechanism by which CF^+ is formed. The detection of CF_2^{2+} indicates the occurrence of the collision-induced neutral loss reaction.



The C^+ observed in our mass spectrum is also attributed to dissociative electron transfer as F_2^+ and F^+ are not detected. Finally, OCF^+ is detected in the mass spectrum showing that a bond forming process is occurring. Position sensitive coincidence studies¹⁶ as well as theoretical studies¹⁷ have shown that, in the similar collision system $CF_2^{2+} + H_2O$, OCF^+ is formed via the complex $H_2OCF_2^{2+}$ which then goes on to fragment.



It is certainly reasonable to infer that the OCF^+ in the collision system $\text{CF}_3^{2+} + \text{H}_2\text{O}$ may be formed via an analogous mechanism to that of OCF^+ formed in the $\text{CF}_2^{2+} + \text{H}_2\text{O}$ collision system.² One would perhaps suppose that, in the case of $\text{CF}_3^{2+} + \text{H}_2\text{O}$, OCF_2^+ may be a bond forming product. However, OCF_2^+ , at $m/z = 66$, is not detected in the mass spectrum. Although OH^+ is not detected in the mass spectrum, its presence cannot be totally eliminated as this area of the mass spectrum is partially obscured by the edges of the H_2O^+ signal. If there is a signal from OH^+ , it is certainly not larger than 5 % of the H_2O^+ signal. H^+ is present in the mass spectrum for $\text{CF}_3^{2+} + \text{H}_2\text{O}$. This H^+ signal may arise as a result of fragmentation of H_2O^+ to $\text{H}^+ + \text{OH}$ or, in a bond-forming process, from the fragmentation of the intermediate $\text{H}_2\text{OCF}_3^{2+}$ to $\text{OCF}^+ + \text{HF}_2 + \text{H}^+$. The formation and subsequent fragmentation of the potential intermediate $\text{H}_2\text{OCF}_3^{2+}$ formed in collisions between CF_3^{2+} and H_2O will be discussed in detail later in this chapter.

6.2.3 $\text{CF}_3^{2+} + \text{H}_2\text{S}$

Following collisions between CF_3^{2+} and H_2S , we observe in our mass spectrum analogous product ions to those produced in the $\text{CF}_3^{2+} + \text{H}_2\text{O}$ collision system. We therefore assign CF_2^+ , CF^+ and C^+ to dissociative electron transfer. No analogous bond-forming product (SCF^+) is detected, perhaps because it is formed in quantities which lie below the detection limits of the apparatus. In contrast to the $\text{CF}_3^{2+} + \text{H}_2\text{O}$ collision system, we observe fragmentation of the monocation derived from the neutral. That is, HS^+ and S^+ . It is not possible to say with any certainty whether H_2S^+ is formed following collisions between CF_3^{2+} and H_2S as H_2S^+ has a mass to charge ratio of 34 and may be obscured by the wings of the large unreacted reactant dication

signal CF_3^{2+} at $m/z = 34.5$. In contrast with the $\text{CF}_3^{2+} + \text{H}_2\text{O}$ collision system, no H^+ signal is present in the $\text{CF}_3^{2+} + \text{H}_2\text{S}$ mass spectrum.

6.3 Determination of integral cross sections

Integral reaction cross sections, in arbitrary units, have been determined for the formation of the electron transfer products derived both from the reactant dication, [CF_3^+ , CF_2^+ , CF^+ and C^+], and from the neutral, [H_2X^+ , XH^+ and X^+] following collisions between CF_3^{2+} and H_2X . In order to determine these integral reaction cross sections, we require information about the translational energy of the various ions across the source region of the TOFMS. These translational energies are required in order to determine both of the quantities L_j and v_j required for equation 3.21 in chapter 3. In previous investigations, it has been shown that the total kinetic energy release (KER) experienced by the two singly charged product ions following a non-dissociative electron transfer process is about 7 eV.^{4,18-20} Therefore, we use in our kinematic calculations, a combined kinetic energy of 7 eV for the two singly charged product ions as they move away from one another, when calculating the velocity of the product ion across the source region of the TOFMS. We also assume that the reaction is dominated by forward scattering of the monocation derived from the dication as has been shown to be the case in other collision systems.^{4,18-20} Once the velocity v of each ion across the source region of the TOFMS has been determined, L may be evaluated from the geometry of the apparatus. When evaluating L for each daughter ion, we assume that the parent ions, in this case CF_3^+ and H_2X^+ , undergo fragmentation only when they have departed from the field of the other product ion. In this assumption, each daughter ion will possess a velocity across the source region of the TOFMS equal to that of its parent product ion. For example, in the process



we assume that no kinetic energy release occurs during the separation of CF_2^+ and F. As a result, CF_2^+ is left with a final velocity identical to the initial velocity of CF_3^+ . This assumption holds, because the kinetic energy released when a monocation and neutral separate, is negligible compared with the kinetic energy released during the charge separation of two monocations.

Using the above assumption, we can determine the integral reaction cross section in arbitrary units for all the electron transfer channels. It should be mentioned here, that integral reaction cross sections for forming product ions derived from the reactant dication and those derived from the neutral collision partner are not directly comparable. This arises as a result of the different areas of the TOF source region from which the two types of electron transfer product ions are sampled. Fig 6.2 shows how forward scattering in the centre of mass frame relates to scattering in the laboratory frame. In Figure 6.2, v_1 is the centre of mass frame velocity of the monocation derived from the neutral and v_2 is the centre of mass frame velocity of the monocation derived from the reactant dication. In addition, v_{com} is the velocity, in the laboratory frame, of the centre of mass. At lower collision energies, such as these experiments, the magnitude of v_1 is greater than that of v_{com} .

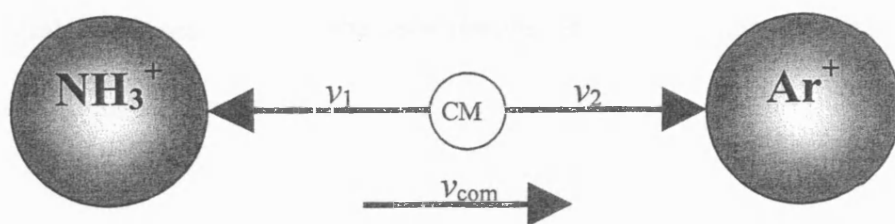


Figure 6.2 Diagram of how forward or backward scattering in the centre of mass frame relates to forward or backward scattering in the laboratory frame.

Consequently, the monocation derived from the neutral will be backward scattered in both the laboratory frame and the centre of mass frame. At higher collision energies, the velocity of the centre of mass, v_{com} , may be larger than the magnitude of v_1 . The monocation derived from the neutral may then be backward scattered in the centre of mass frame but forward scattered in the laboratory frame. Ions derived from the reactant dication are always forward scattered and so, from fig 6.3, we can see that, in order for them to reach the detector, they must be sampled from the area A of the TOF source region. However, because product ions derived from the neutral collision partner are backward scattered in both the centre of mass frame and the laboratory frame over the energies studied, in order for them to reach the detector they must be sampled from area B of the TOF source region. The H_2X pressure in these two areas of the TOF source region will be different during an experiment. However, we assume in our measurements of the integral reaction cross section, that the pressure of the neutral collision gas, n , is constant. Indeed, the pressure at any point in the TOF source region is constant with time. Hence, the pressure differential across the TOF source region will result in measured integral cross sections for ions derived from the reactant dication not being directly comparable with measured integral cross sections for ions derived from the neutral. To avoid confusion, integral cross sections for ions derived from the neutral collision partner will be referred to as σ'' . Integral cross sections for the ions derived from the reactant dication are, as mentioned, referred to as σ' .

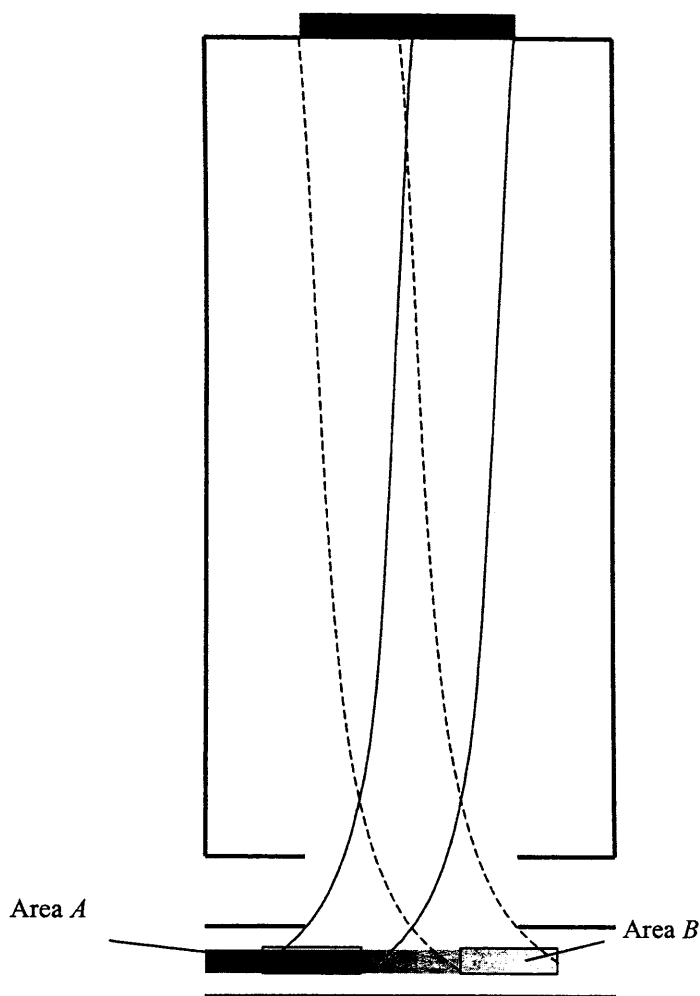


Figure 6.3 Diagram illustrating how backward and forward scattered product ions are sampled from different areas of the source region of the TOF with different neutral collision gas pressures.

In the case of the bond forming product, OCF^+ , we assume a bond forming adduct, $\text{H}_2\text{OCF}_3^{2+}$, dissociates to H^+ and HOCF_3^+ with a KER of 7 eV. This initial fragmentation has been shown to occur, by position sensitive coincidence studies for the analogous $\text{CF}_2^{2+} + \text{H}_2\text{O}$ collision system.¹⁶ The charge separation of the initial bond forming adduct to a heavy ion and a light ion means that very little extra kinetic energy is imparted onto the HOCF_3^+ ion as a result of this KER. That is, the light H^+ ion carries away the majority of the kinetic energy released from the charge separation and the heavier HOCF_3^+ ion is left with a laboratory frame velocity only slightly different to that of the initial HOCF_3^+ . The neutral loss of HF_2 from HOCF_3^+ will not significantly affect the velocity of the ion, now OCF^+ , across the source

region of the TOFMS. As a result, the integral reaction cross section for forming OCF^+ differs only marginally from its value of R_{real} . The H^+ signal is very small in this mass spectrum because H^+ is very light and highly energetic. As a result, our collection efficiency for H^+ ions is very poor. As discussed above, the loss of neutral HF_2 does not affect the velocity OCF^+ across the source region of the TOFMS. We may therefore use this mechanism to extract a value for the integral reaction cross section of the bond forming reaction. Having extracted the integral reaction cross section for the relevant bond forming, dissociative and non dissociative electron transfer and collision induced neutral loss reactions, we may plot them as a function of collision energy. These plots are shown in figures 6.4 to 6.7. These plots indicate that the ion yields are largely independent of collision energy as has been observed in other similar experiments.² In order to rationalise the variation with energy of integral reaction cross sections for the electron transfer processes, we have employed a model based on the Landau-Zener theory.

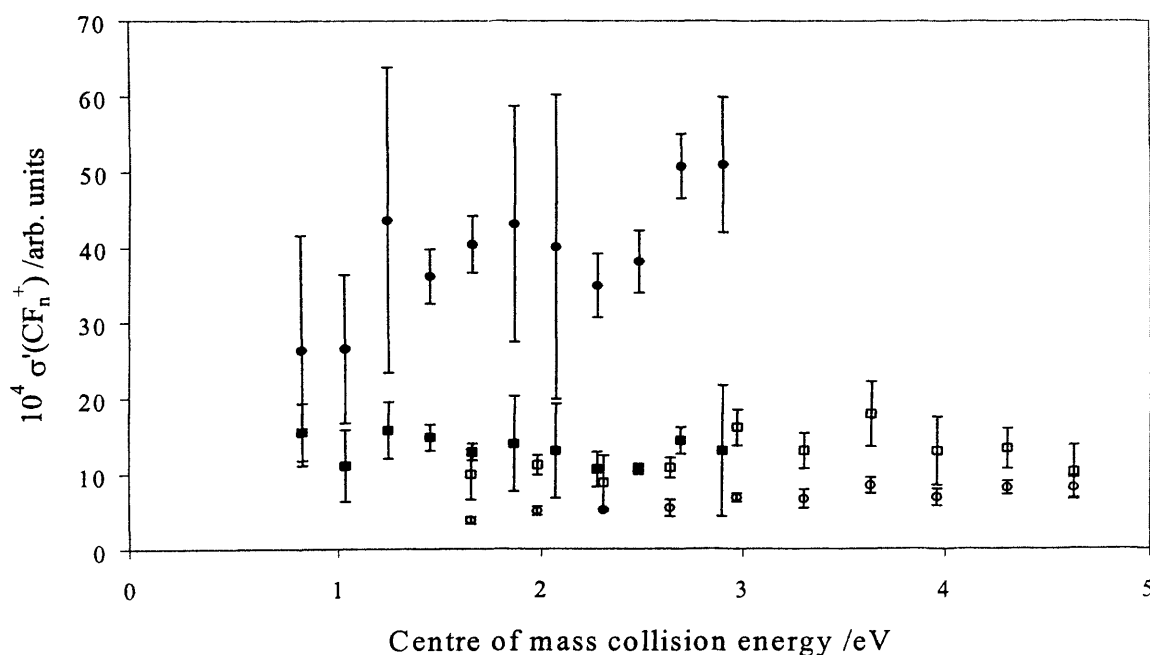


Figure 6.4 Integral reaction cross section in arbitrary units, as a function of centre of mass collision energy, for forming CF^+ (■) and CF_2^+ (●) from $\text{CF}_3^{2+} + \text{H}_2\text{O}$ and CF^+ (□) and CF_2^+ (○) from $\text{CF}_3^{2+} + \text{H}_2\text{S}$

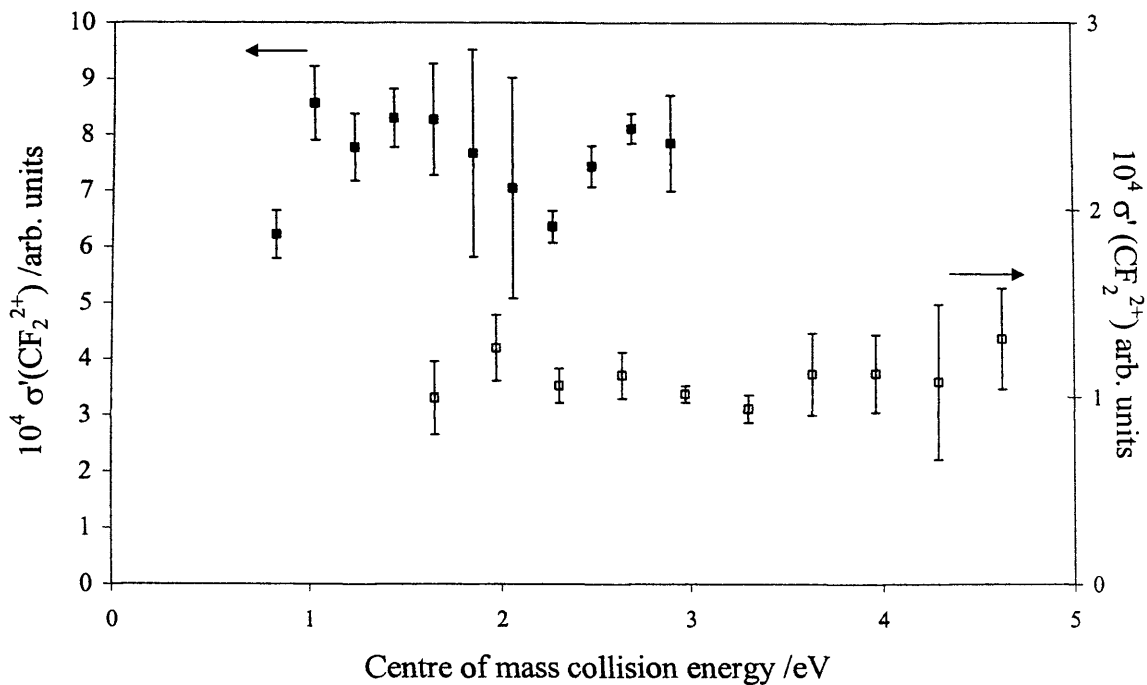


Figure 6.5 Integral reaction cross section in arbitrary units as a function of centre of mass collision energy for forming CF_2^{2+} (■) from $\text{CF}_3^{2+} + \text{H}_2\text{O}$ and CF_2^{2+} (□) from $\text{CF}_3^{2+} + \text{H}_2\text{S}$. The data for the formation of CF_2^{2+} from $\text{CF}_3^{2+} + \text{H}_2\text{O}$ is shown on the left hand axis.

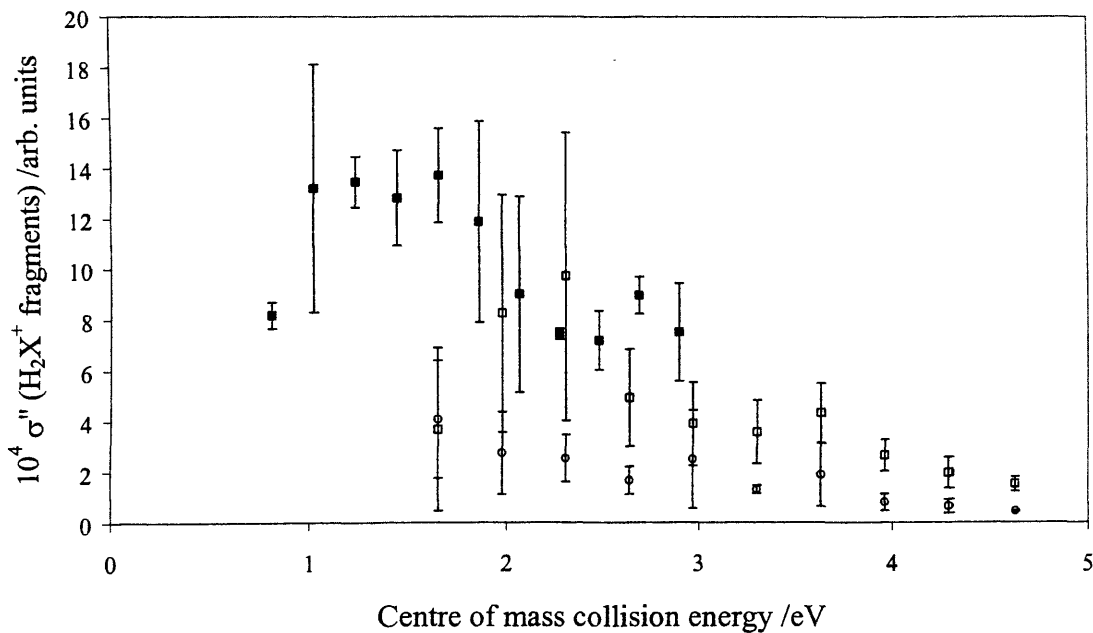


Figure 6.6 Integral reaction cross section in arbitrary units as a function of centre of mass collision energy for forming H_2O^+ (■) from $\text{CF}_3^{2+} + \text{H}_2\text{O}$ and HS^+ (□) and S^+ (○) from $\text{CF}_3^{2+} + \text{H}_2\text{S}$

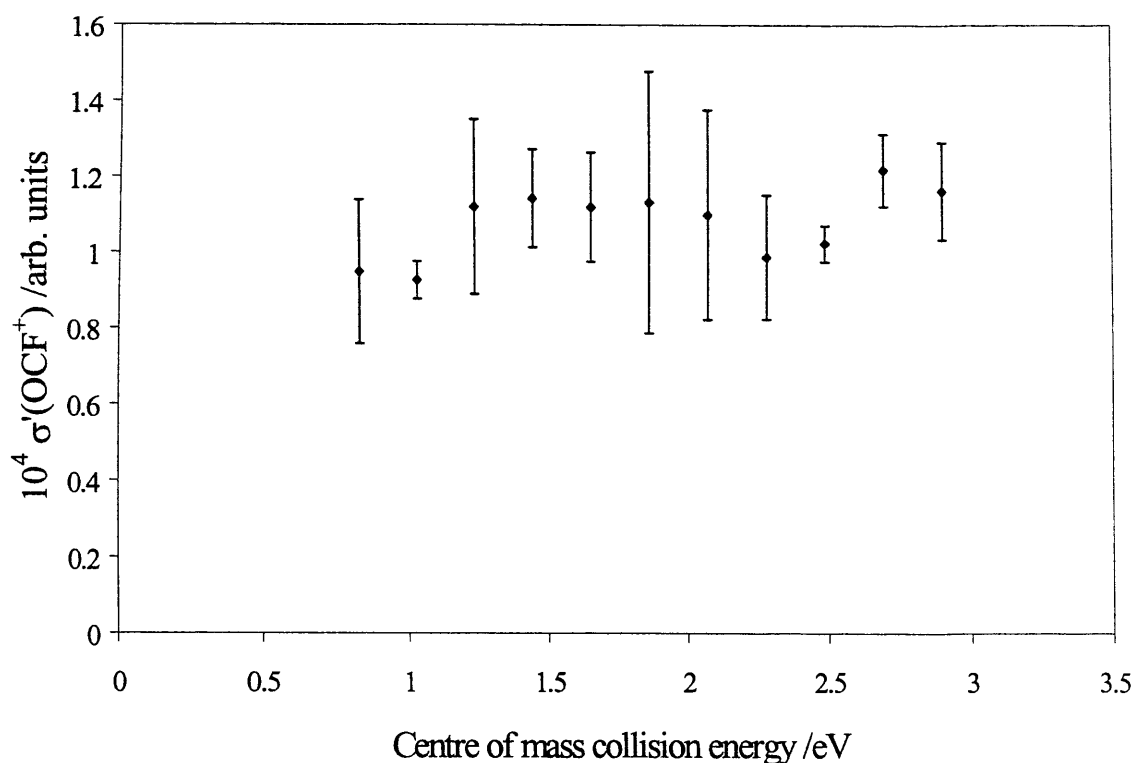


Figure 6.7 Integral reaction cross section in arbitrary units as a function of centre of mass collision energy for forming OCF^+ (ν) from $\text{CF}_3^{2+} + \text{H}_2\text{O}$

6.4 Discussion

6.4.1 Landau-Zener calculations

As discussed previously, in order to understand the electron transfer process, we use the reaction window model based on the Landau-Zener theory.^{21,22} This model allows us to predict the electronic states in which the electron transfer product ions will be formed (CF_3^+ and H_2X^+) directly following a collision. In order to rationalise the relative abundances of the various dissociative and non-dissociative electron transfer products, it is vital that we understand how each electronic state of these electron transfer product ions will fragment. In the past, photoelectron-photoion coincidence (PEPICO) studies have been used to determine exactly how each state of H_2X^+ will behave.^{23,24} These studies have shown that the ground electronic (X) states of both H_2O^+ and H_2S^+ are stable. In the case of the first excited (A) state of H_2S^+ ,

lower lying vibrational levels are stable, whereas higher lying vibrational levels dissociate to form S^+ and H_2 . The second excited (*B*) state of H_2S^+ dissociates to yield HS^+ and H . The first excited (*A*) state of H_2O^+ is stable and higher vibrational levels of the second excited (*B*) state of H_2O^+ fragment to yield OH^+ or H^+ .

To our knowledge, no PEPICO studies have been carried out on CF_3 , which would determine the fragmentation properties of CF_3^+ . Therefore, in order that we may predict how CF_3^+ fragments, it is necessary to rely on the relative energetics of the various electronic states of CF_3^+ relative to the various dissociation asymptotes. We assume that a particular vibronic state of the product parent ions lying on or above a certain dissociation limit will dissociate to yield those fragment ions. If a vibronic state lies above two or more dissociation limits, we assume it will dissociate to the dissociation limit lying highest in energy. This assumption regarding the dissociation of each vibronic state of the primary product ions is not considered to be a major one. Indeed, previous PEPICO experiments by Eland have shown that the vibrational ground state (0,0,0) of CO_2^+ ($C\ ^2\Sigma_g^+$) fragments to O^+ and CO in its ground vibrational level whereas higher vibrational levels fragment to products corresponding to dissociation asymptotes lying directly below them in energy.²⁵ Similar results have been obtained in PEPICO experiments on H_2O and H_2S .^{23,24}

From figure 6.8, we can see schematically how each electronic state of an ion might fragment. The electronic ground state of the monocation XY_n^+ does not lie above any dissociation limit and so is stable. However, the first excited state (*A*) lies above two dissociation limits, we assume that an ion formed in the (*A*) state will fragment to the limit corresponding to $XY_{n-2} + 2Y$ as this limit lies higher in energy. Similarly, the second excited state of XY_2^+ lies directly above the dissociation limit corresponding to loss of $2Y$ so we would expect this ion to fragment accordingly. However, higher

vibrational levels of this electronic state lie above a dissociation limit corresponding to $XY_{n-3} + 3Y$. higher vibrational levels will therefore fragment to these products. Using these simple “rules”, we are able to predict how an ion will fragment.

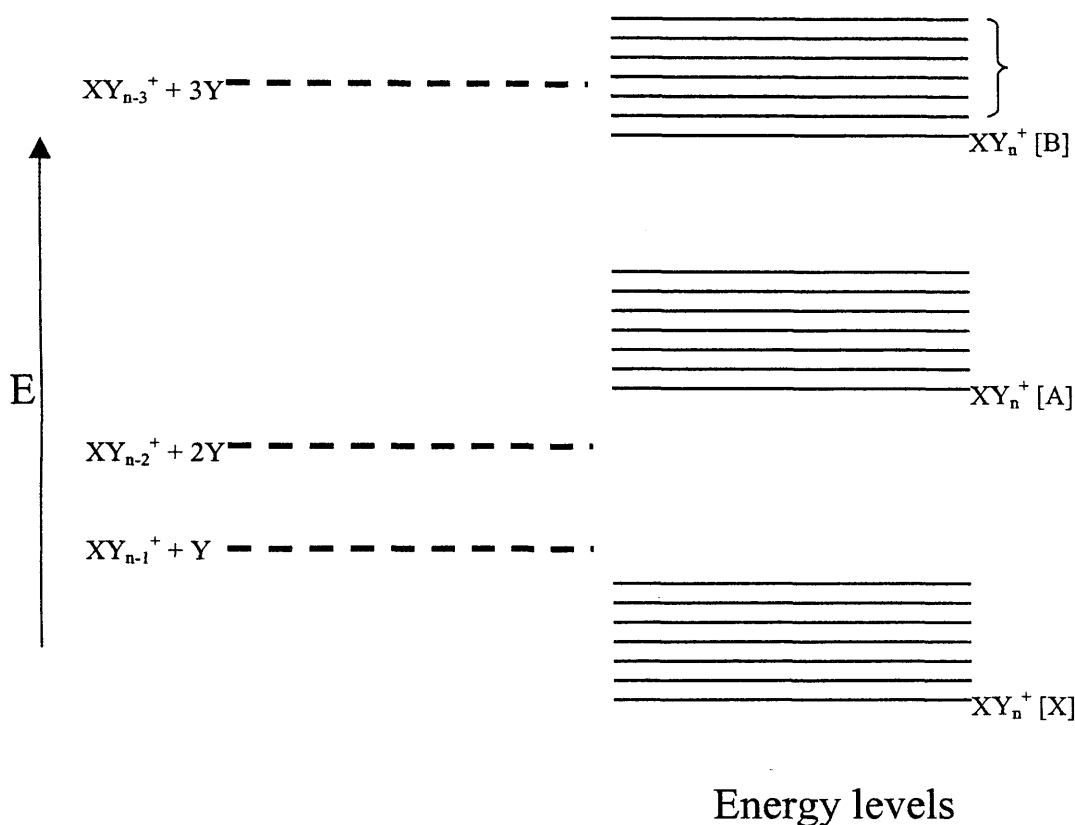


Figure 6.8 Schematic diagram of how different vibronic states of an ion will fragment.

The energies of the lowest lying electronic states of CF_3^+ (relative to the energy of the 1A_1 ground state in its equilibrium D_{3h} geometry) at the geometry of the 2B_2 ground state of CF_3^{2+} , have been calculated previously.¹⁴ Energies are calculated at the geometry of the 2B_1 of CF_3^{2+} as the transition from CF_3^{2+} to CF_3^+ in the electron transfer process is assumed to be vertical. In addition, the energies above the vibronic ground state of CF_3^+ , of the dissociation limits have been calculated from the heats of formation of the various product fragments. These heats of formation of the product fragments have been gathered from data tables.²⁶⁻²⁸ All dissociation limits are calculated using the difference between the heat of formation of CF_3^+ at its

equilibrium geometry, and the heats of formation of the resultant fragments in their equilibrium geometries. In the case of CF_3^+ , the first (lowest) dissociation limit lies 6.19 eV above the vibronic ground state of CF_3^+ and corresponds to the neutral loss $\text{CF}_3^+ \rightarrow \text{CF}_2^+ + \text{F}$. A second dissociation limit lies at 9.23 eV and any vibronic state of CF_3^+ lying on or above this limit is assumed to fragment to $\text{CF}^+ + 2\text{F}$. In addition to forming $\text{CF}^+ + 2\text{F}$, CF^+ may be formed along with F_2 . The dissociation asymptote for $\text{CF}^+ + \text{F}_2$ lies 7.59 eV above the vibronic ground state of CF_3^+ . Vibronic states of CF_3^+ lying above a dissociation asymptote at 16.99 eV are assumed to result in fragmentation to $\text{C}^+ + 3\text{F}$.

Using these positions of the relevant dissociation asymptotes, we may deduce exactly how each state of our electron transfer product ions (CF_3^+ and H_2X^+) will fragment following an electron transfer between CF_3^{2+} and H_2X . In order that we may calculate the exothermicities for electron transfer processes which populate various states of the product monocations, photoelectron spectra of the relevant neutrals have been consulted.^{29,30} For the energies of the various states of CF_3^+ , calculations performed by Tafadar *et al.*¹⁴ have been used. These energies of the low lying electronic states of CF_3^+ are calculated at the equilibrium geometry of the reactant dication CF_3^{2+} . Tables 6.9 and 6.10 show the exothermicity for forming the electron transfer products in each possible combination of their excited states along with their predicted daughter ion and the calculated cross section for that particular electron transfer process.

Electronic state of H ₂ O ⁺ product						
Electronic state of CF ₃ ⁺ product	X	→H ₂ O ⁺	A	→H ₂ O ⁺	B	→H ₂ O ⁺ , OH ⁺ , H ⁺
	ΔH /eV	σ	ΔH /eV	σ	ΔH /eV	σ
1 ¹ A ₁ →CF ₃ ⁺	13.5 (18.5)	0 (0)	11.4 (16.4)	0 (0)	7.6 (12.6)	0 (0)
1 ³ A ₁ →CF ₂ ⁺	6.5 (11.5)	0 (0)	4.5 (9.5)	3.2 (0)	0.6 (5.6)	0 (0.1)
1 ¹ A ₂ →CF ₂ ⁺	6.3 (11.3)	0 (0)	4.2 (9.2)	8.3 (0)	0.4 (5.4)	0 (0.1)
1 ³ A ₂ →CF ₂ ⁺	6.3 (11.3)	0 (0)	4.3 (9.3)	6.2 (0)	0.4 (5.4)	0 (0.1)
2 ¹ A ₁ →CF ₂ ⁺	6.1 (11.1)	0 (0)	4.1 (9.1)	10.9 (0)	0.2 (5.2)	0 (0.2)
1 ¹ B ₂ →CF ₂ ⁺	5.9 (10.9)	0 (0)	3.9 (8.9)	17.2 (0)	0.1 (5.1)	0 (0.3)
1 ³ B ₁ →CF ₂ ⁺	5.7 (10.7)	0 (0)	3.6 (8.6)	26.4 (0)	-0.2 (4.8)	0 (1.1)
1 ¹ B ₁ →CF ₂ ⁺	5.1 (10.1)	0.4 (0)	3.0 (8.0)	20.1 (0)	-0.8 (4.2)	0 (8.3)
2 ¹ B ₁ →CF ₂ ⁺	4.9 (9.9)	0.7 (0)	2.9 (7.9)	16.3 (0)	-1.0 (4.0)	0 (13.9)
2 ³ B ₁ →CF ₂ ⁺	4.9 (9.9)	0.7 (0)	2.8 (7.8)	12.5 (0)	-1.0 (4.0)	0 (13.9)
2 ³ A ₁ →CF ₂ ⁺	4.8 (9.8)	1.1 (0)	2.8 (7.8)	12.5 (0)	-1.1 (3.9)	0 (17.2)
2 ¹ B ₂ →CF ₂ ⁺	2.6 (7.6)	6.3 (0)	0.6 (5.6)	0 (0)	-3.3 (1.7)	0 (0)
2 ³ A ₂ →CF ₂ ⁺	2.3 (7.3)	1.4 (0)	0.3 (5.3)	0 (0.2)	-3.6 (1.4)	0 (0)
2 ¹ A ₂ →CF ₂ ⁺	2.2 (7.2)	0.8 (0)	0.2 (5.2)	0 (0.2)	-3.7 (1.3)	0 (0)
3 ³ A ₁ →CF ⁺	0.1 (5.1)	0 (0.2)	-1.9 (3.1)	0 (23.7)	-5.7 (-0.7)	0 (0)
3 ¹ B ₁ →CF ⁺	-0.3 (4.7)	0 (1.6)	-2.4 (2.6)	0 (16.3)	-6.2 (-1.2)	0 (0)
3 ³ B ₁ →CF ⁺	-0.3 (4.7)	0 (1.6)	-2.3 (2.7)	0 (19.1)	-6.2 (-1.2)	0 (0)
3 ¹ B ₂ →CF ⁺	-1.0 (4.0)	0 (13.9)	-3.1 (1.9)	0 (1.2)	-6.9 (-1.9)	0 (0)
3 ³ A ₂ →CF ⁺	-1.1 (3.9)	0 (17.2)	-3.2 (1.8)	0 (0)	-7.0 (-2.0)	0 (0)
3 ¹ A ₂ →CF ⁺	-1.4 (3.6)	0 (26.4)	-3.4 (1.6)	0 (0)	-7.3 (-2.3)	0 (0)
3 ¹ A ₁ →C ⁺	-2.1 (2.9)	0 (16.3)	-4.1 (0.9)	0 (0)	-8.0 (-3.0)	0 (0)

Table 6.9 Exothermicities and calculated cross sections for forming CF₃⁺ and H₂O⁺ from CF₃²⁺ and H₂O in various electronic states. Also shown are the predicted fragmentation pathway of each ion. The values in parenthesis are those for forming productions from H₂O with CF₃²⁺ in an excited state lying 5 eV above the ground state.

Electronic state of H ₂ S ⁺ product						
Electronic state of CF ₃ ⁺ product	X	→H ₂ S ⁺	A	→H ₂ S ⁺ , S ⁺	B	→HS ⁺
	ΔH/eV	σ	ΔH/eV	σ	ΔH/eV	σ
1 ¹ A ₁ →CF ₃ ⁺	15.6 (20.6)	0 (0)	12.7 (17.7)	0 (0)	10.6 (15.6)	0 (0)
1 ³ A ₁ →CF ₂ ⁺	8.6 (13.6)	0 (0)	5.8 (10.8)	0.8 (0)	3.6 (8.6)	29.0 (0)
1 ³ A ₂ →CF ₂ ⁺	8.5 (13.5)	0 (0)	5.6 (10.6)	1.1 (0)	3.5 (8.5)	32.4 (0)
1 ¹ A ₂ →CF ₂ ⁺	8.4 (13.4)	0 (0)	5.5 (10.5)	1.3 (0)	3.4 (8.4)	32.4 (0)
2 ¹ A ₁ →CF ₂ ⁺	8.2 (13.2)	0 (0)	5.4 (10.4)	1.8 (0)	3.2 (8.2)	32.4 (0)
1 ¹ B ₂ →CF ₂ ⁺	8.1 (13.1)	0 (0)	5.2 (10.2)	2.1 (0)	3.1 (8.1)	28.3 (0)
1 ³ B ₁ →CF ₂ ⁺	7.8 (12.8)	0 (0)	4.9 (9.9)	3.7 (0)	2.8 (7.8)	21.2 (0)
1 ¹ B ₁ →CF ₂ ⁺	7.2 (12.2)	0.2 (0)	4.3 (9.3)	11.1 (0)	2.2 (7.2)	2.7 (0.2)
2 ³ A ₁ →CF ₂ ⁺	7.0 (12.0)	0.2 (0)	4.1 (9.1)	15.5 (0)	2.0 (7.0)	0.4 (0.2)
2 ¹ B ₁ →CF ₂ ⁺	7.0 (12.0)	0.2 (0)	4.2 (9.2)	15.5 (0)	2.0 (7.0)	0.8 (0.2)
2 ³ B ₁ →CF ₂ ⁺	7.0 (12.0)	0.2 (0)	4.1 (9.1)	15.5 (0)	2.0 (7.0)	0.8 (0.2)
2 ¹ B ₂ →CF ₂ ⁺	4.7 (9.7)	5.3 (0)	1.9 (6.9)	0.4 (0.2)	-0.3 (4.7)	0 (5.3)
2 ³ A ₂ →CF ₂ ⁺	4.5 (9.5)	0.9 (0)	1.6 (6.6)	0 (0.3)	-0.5 (4.5)	0 (9.3)
2 ¹ A ₂ →CF ₂ ⁺	4.3 (9.3)	11.1 (0)	1.5 (6.5)	0 (0.3)	-0.7 (4.3)	0 (11.1)
3 ³ A ₁ →CF ⁺	2.3 (7.3)	4.4 (0.2)	-0.6 (4.4)	0 (9.3)	-2.7 (2.3)	0 (4.4)
3 ¹ B ₁ →CF ⁺	1.8 (6.8)	0 (0.2)	-1.1 (3.9)	0 (20.9)	-3.2 (1.8)	0 (0)
3 ³ B ₁ →CF ⁺	1.8 (6.8)	0 (0.2)	-1.0 (4.0)	0 (20.9)	-1.2 (1.8)	0 (0.2)
3 ¹ B ₂ →CF ⁺	1.1 (6.1)	0 (0.5)	-1.7 (3.3)	0 (32.4)	-3.9 (1.1)	0 (0)
3 ³ A ₂ →CF ⁺	1.0 (6.0)	0 (0.6)	-1.9 (3.1)	0 (30.8)	-4.0 (1.0)	0 (0)
3 ¹ A ₂ →CF ⁺	0.7 (5.7)	0 (0.9)	-2.1 (2.9)	0 (21.3)	-4.3 (0.7)	0 (0)
3 ¹ A ₁ →C ⁺	0.1 (5.1)	0 (3)	-2.8 (2.2)	0 (2.7)	-4.9 (0.1)	0 (0)

Table 6.10 Exothermicities and calculated cross sections for forming CF₃⁺ and H₂S⁺ from CF₃²⁺ and H₂S in various electronic states. Also shown are the predicted fragmentation pathway of each ion. The values in parenthesis are those for forming productions from H₂S with CF₃²⁺ in an excited state lying 5 eV above the ground state.

6.4.2 Formation of CF_n^+ from $\text{CF}_3^{2+} + \text{H}_2\text{O}$

The Landau Zener reaction window algorithm, the results of which are shown in tables 6.9 and 6.10, predicts that, during collisions between CF_3^{2+} and H_2O , the calculated cross section (σ_{calc}) for forming CF_3^+ in states which fragment to CF_2^+ is 145 Å (Fig 6.11). In addition, the values of σ_{calc} for forming CF_3^+ which fragments to C^+ , CF^+ or remains stable as CF_3^+ are zero. These predictions are in conflict with our experimental results which show that, in reality, although CF_2^+ is indeed formed in larger quantities, CF^+ is still observed in the mass spectrum. For $\text{CF}_3^{2+} + \text{H}_2\text{O}$, the ratio of R_{real} for CF^+ and CF_2^+ is about 1 to 2.

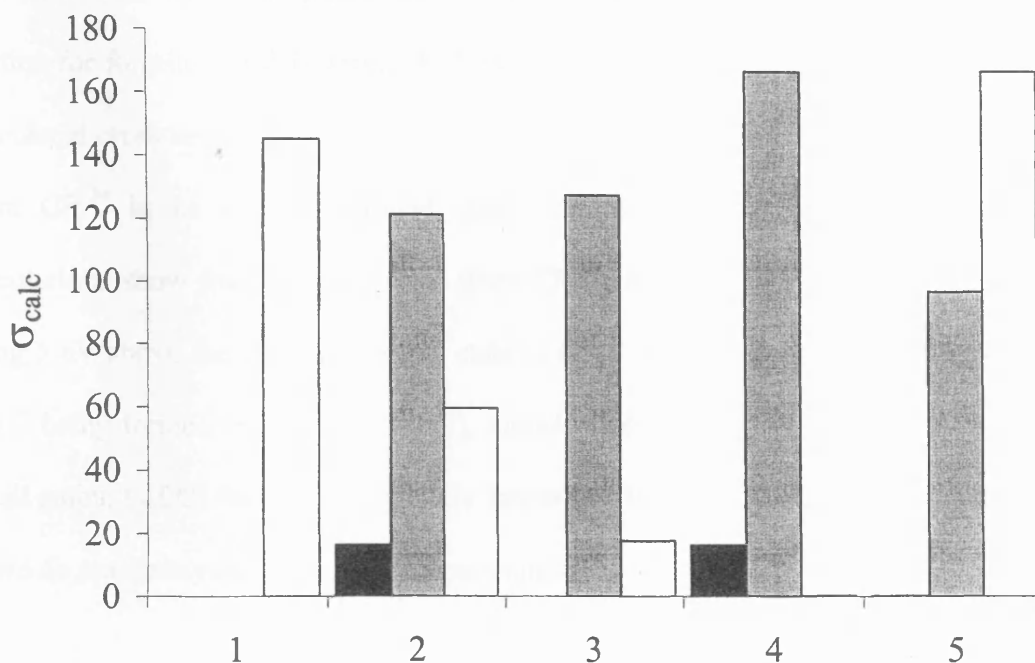


Figure 6.11 $\text{CF}_3^{2+} + \text{H}_2\text{O}$. Landau-Zener calculated cross section (\AA^2) for forming C^+ (black), CF^+ (grey) and CF_2^+ (white). (1) $\Delta H_f(\text{CF}_3^{2+}) = 30.47$ eV, (2) $\Delta H_f(\text{CF}_3^{2+}) = 35.47$ eV, (3) $\Delta H_f(\text{CF}_3^{2+}) = 30.47$ eV with dissociation limit $\text{CF}_3^+ \rightarrow \text{CF}^+ + \text{F}_2$, (4) $\Delta H_f(\text{CF}_3^{2+}) = 35.47$ eV with dissociation limit $\text{CF}_3^+ \rightarrow \text{CF}^+ + \text{F}_2$. (5) is the measured integral cross section, in arbitrary units, normalized to the largest calculated cross section.

In the past, it has been suggested that a higher energy state of CF_3^{2+} , lying 5 eV above the ground state of CF_3^{2+} , may be present in an incident dication beam formed

by electron impact of CF_4 .¹⁴ If this excited CF_3^{2+} takes part in the electron transfer process, an electron will transfer from H_2O to yield CF_3^+ with sufficiently high internal energy to fragment to $\text{CF}^+ + 2\text{F}$. Therefore, this excited state of CF_3^+ will be expected to fragment to CF^+ and 2F . The exothermicity for the transition $\text{CF}_3^{2+*} \rightarrow \text{CF}_3^+$ will be within the required window of exothermicities for the reaction to be favoured. From Fig 6.11, block 2, it is clear that the presence of CF_3^{2+*} , lying 5 eV above the vibronic ground state of CF_3^{2+} , in the incident dication beam would increase the amount of CF^+ formed following collisions between CF_3^{2+} and H_2O and so account for the measured CF^+ to CF_2^+ ratio of 1 to 2.

The calculated cross section for forming stable CF_3^+ is zero. The measured cross section for forming CF_3^+ is zero, which is in accordance with our calculations. The calculated cross section for forming CF_3^+ in states which will fragment to yield C^+ , from CF_3^{2+} in its vibronic ground state, is zero. However, our Landau-Zener calculations show that, forming CF_3^+ from CF_3^{2+} in an electronically excited state lying 5 eV above the vibronic ground state of CF_3^{2+} would result in a small amount of C^+ being formed (Fig 6.11, block 2), namely from $\text{CF}_3^+ (3^1\text{A}_1) + \text{H}_2\text{O}^+ (X)$. The small amount of C^+ formed may well lie below the detection limits of our apparatus, as we do not observe C^+ in our mass spectrum.

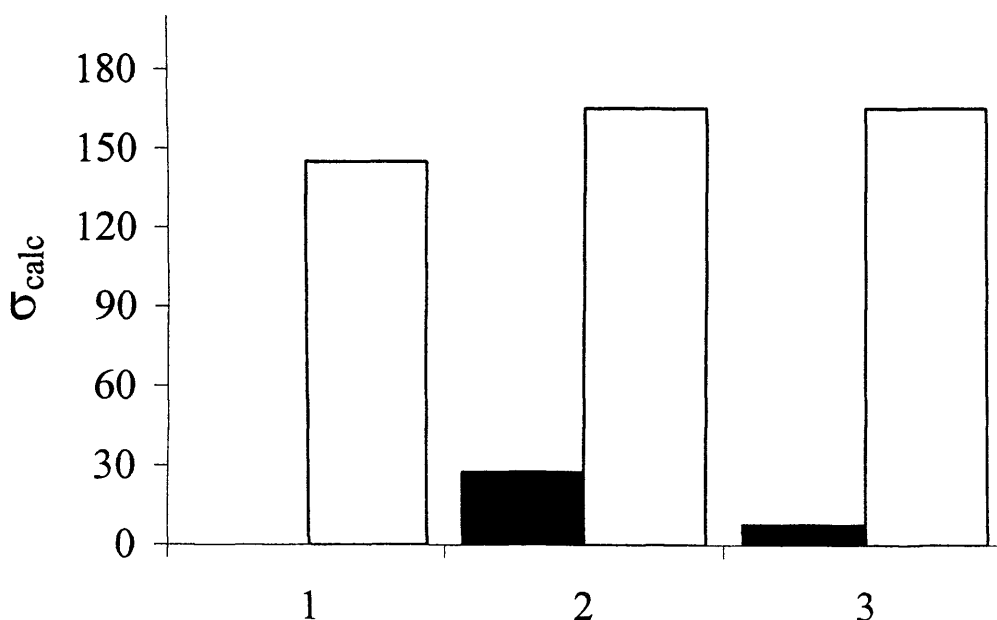


Figure 6.12 $\text{CF}_3^{2+} + \text{H}_2\text{O}$. Landau-Zener calculated cross section (\AA^2) for forming $\text{OH}^+ + \text{H}^+$ (black) and H_2O^+ (white). (1) $\Delta H_f(\text{CF}_3^{2+}) = 30.47$ eV, (2) $\Delta H_f(\text{CF}_3^{2+}) = 35.47$ eV. (3) is the measured integral cross section, in arbitrary units, normalized to the largest calculated cross section.

6.4.3 Formation of H_2O^+ fragments from $\text{CF}_3^{2+} + \text{H}_2\text{O}$

From our Landau-Zener calculations we predict that H_2O^+ will be formed in principally (*X*) and (*A*) states which are stable (Table 6.10). This is in agreement with our experimental results where only H_2O^+ is observed with no evidence for forming O^+ or OH^+ . However, H^+ is detected following collisions between CF_3^{2+} and H_2O . This H^+ may well come from the bond forming reaction mentioned earlier and discussed later. Also, if we consider a proportion of the electron transfer products to be formed from H_2O with CF_3^{2+*} , then a small amount of H_2O^+ will be formed in its (*B*) state (fig 6.12, block 2), higher vibrational levels of which fragment to yield OH^+ and H^+ . OH^+ may well be obscured within the wings of the H_2O^+ signal in the mass spectrum. H^+ is observed in the mass spectrum. However, H^+ , being very light and back scattered in the laboratory frame, has a low detection efficiency in our

experiment. In short, it is certainly plausible that the slight H^+ signal could originate from both the bond forming process and from dissociative electron transfer.

It should be noted that, for the (*B*) state of H_2O^+ , where several possible product ions are predicted, we assume that half of the ions fragment to OH^+ and H^+ and the other half remain undissociated. We make this assumption because the first dissociation limit of H_2O^+ ($H_2O^+ \rightarrow OH + H^+$) lies in the centre of the Franck-Condon region for forming H_2O^+ in its (*B*) state. Significantly higher vibrational states of H_2O^+ (*B*) lie above the limit $H_2O^+ \rightarrow OH^+ + H$.

6.4.4 Formation of CF_n^+ from $CF_3^{2+} + H_2S$

From Fig 6.13, block 1, we see that during collisions between CF_3^{2+} and H_2S , σ_{calc} for forming CF_3^+ in states which fragments to CF_2^+ is 289.4 \AA^2 . Also, σ_{calc} for forming CF_3^+ which fragments to CF^+ is 4.4 \AA^2 and σ_{calc} for forming CF_3^+ in states which fragment to C^+ is 0 \AA^2 . That is, a ratio of CF_2^+ to CF^+ of about 66 to 1. Our experiments show that, in reality, CF^+ is formed in greater quantities than CF_2^+ with an observed ratio of these two ions being about 0.4 to 1. Additionally, C^+ is observed in our mass spectrum with a cross section about 0.2 % of the CF^+ signal, contrary to our initial calculated predictions. As before, we consider a higher lying state of CF_3^{2+} to be present in the incident dication beam to account for this discrepancy between calculated and experimental product ion branching ratios.

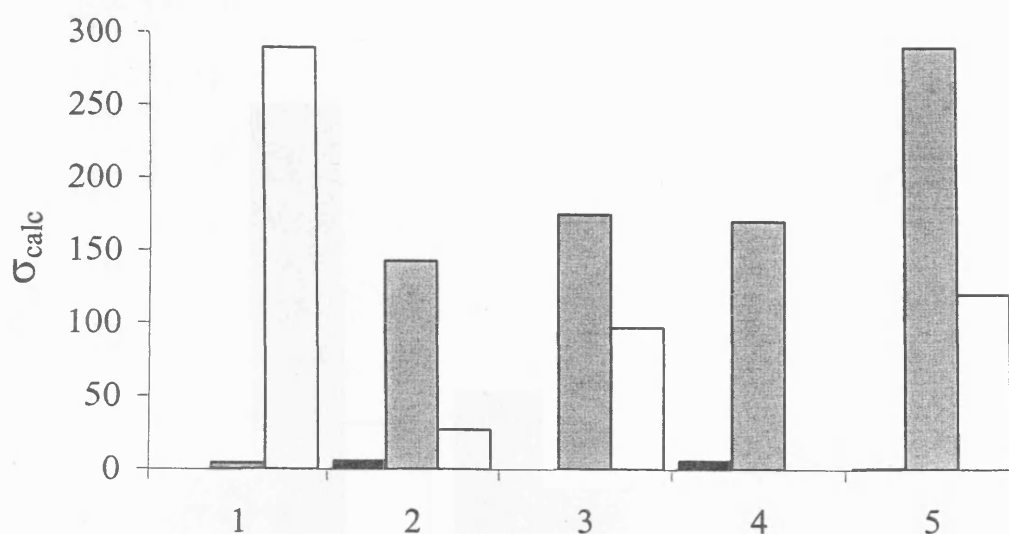


Figure 6.13 $\text{CF}_3^{2+} + \text{H}_2\text{S}$. Landau-Zener calculated cross section (\AA^2) for forming C^+ (black), CF^+ (grey) and CF_2^+ (white). (1) $\Delta H_f(\text{CF}_3^{2+}) = 30.47 \text{ eV}$, (2) $\Delta H_f(\text{CF}_3^{2+}) = 35.47 \text{ eV}$, (3) $\Delta H_f(\text{CF}_3^{2+}) = 30.47 \text{ eV}$ with dissociation limit $\text{CF}_3^+ \rightarrow \text{CF}^+ + \text{F}_2$, (4) $\Delta H_f(\text{CF}_3^{2+}) = 35.47 \text{ eV}$ with dissociation limit $\text{CF}_3^+ \rightarrow \text{CF}^+ + \text{F}_2$. (5) is the measured integral cross section, in arbitrary units, normalized to the largest calculated cross section

In a similar case to that of $\text{CF}_3^{2+} + \text{H}_2\text{O}$, calculations have been performed to account for the presence of this excited state of CF_3^{2+} lying about 5 eV above the vibronic ground state. This higher lying state of CF_3^{2+} will form a proportion of CF_3^+ , during electron transfer, which will possess sufficient internal energy to fragment to CF^+ . In addition, the exothermicity for this process will fall within the window of exothermicities within which the electron transfer process is most facile. This mixture of CF_3^{2+} and CF_3^{2+*} in the incident dication beam will therefore serve to increase the amount of CF^+ and also C^+ formed. Indeed, CF_2^+ , CF^+ and C^+ are all detected here (Table 6.1) in proportions similar to those calculated. CF_3^+ is neither theoretically predicted nor detected experimentally.

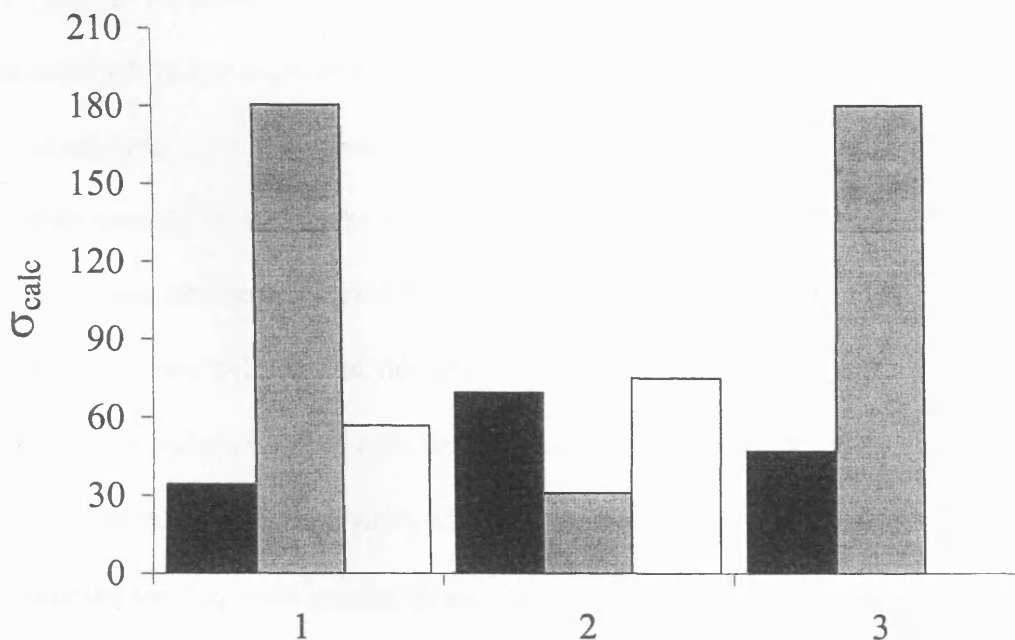


Figure 6.14 $\text{CF}_3^{2+} + \text{H}_2\text{S}$. Landau-Zener calculated cross section (\AA^2) for forming S^+ (black), HS^+ (grey) and H_2S^+ (white). (1) $\Delta H_f(\text{CF}_3^{2+}) = 30.47 \text{ eV}$, (2) $\Delta H_f(\text{CF}_3^{2+}) = 35.47 \text{ eV}$. (3) is the measured integral cross section, in arbitrary units, normalized to the largest calculated cross section

6.4.5 Formation of H_2S^+ fragments from $\text{CF}_3^{2+} + \text{H}_2\text{S}$

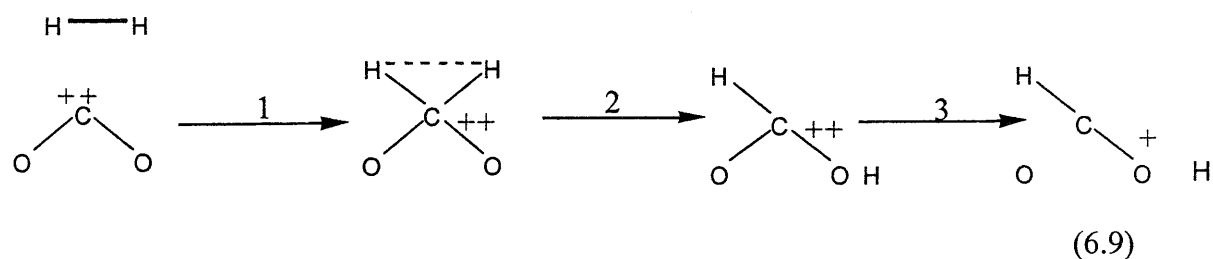
Following collisions between CF_3^{2+} and H_2S , the calculated cross section for forming HS^+ is about six times that for forming S^+ (Fig.6.14). The experimental cross section ratio of HS^+ to S^+ is about four to one. However, $\text{H}_2\text{S} + \text{CF}_3^{2+*}$ will yield more H_2S^+ in its (*A*) state, higher vibrational levels of which will fragment to S^+ . Consequently, the amount of S^+ formed will be more compared to if CF_3^{2+} existed in its ground state only. Similarly to the case of H_2O^+ , H_2S^+ in its (*A*) state should dissociate to yield both H_2S^+ and HS^+ in equal amounts because the first dissociation limit of H_2S^+ lies directly in the centre of the Franck-Condon region for $\text{H}_2\text{S} \rightarrow \text{H}_2\text{S}^+(A)$.

It should be noted that a hypothetical dissociation limit $\text{CF}_3^+ \rightarrow \text{CF}^+ + \text{F}_2$ exists 7.59 eV above the vibronic ground state of CF_3^+ and 1.65 eV below the dissociation limit $\text{CF}_3^+ \rightarrow \text{CF}^+ + 2\text{F}$. In similar studies of this type, most notably collisions between

CF_3^{2+} and Ar performed by Tafadar *et al.*¹⁴, this limit, $\text{CF}_3^+ \rightarrow \text{CF}^+ + \text{F}_2$, has not been included. In our study of $\text{CF}_3^{2+} + \text{H}_2\text{X}$, this limit has not been incorporated into our calculations. The fragmentation pathway $\text{CF}_3^+ \rightarrow \text{CF}^+ + \text{F}_2$ would require a concerted process in which the C-F bonds are cleaved and the F-F bond formed. Such a process has been reported in the past, where CS_2^+ dissociates you yield $\text{C} + \text{S}_2^+$. However, we believe that the process $\text{CF}_3^+ \rightarrow \text{CF}^+ + \text{F}_2$ is not a significant fragmentation pathway here due to the time scale involved for bond rearrangement. However, for completeness, figures 6.11 to 6.14 show the values of σ_{calc} for forming each product ion fragment had the dissociation limit $\text{CF}_3^+ \rightarrow \text{CF}^+ + \text{F}_2$ been included. As can be seen, there is no significant change in our conclusions had this limit been included in our calculations.

6.4.6 Bond forming reaction

The $\text{CF}_3^{2+} + \text{H}_2\text{O}$ collision system yields the ion OCF^+ . It is reasonable to suppose that the mechanism for the chemical reaction forming OCF^+ is similar to the bond forming process observed previously in the collision system $\text{CF}_2^{2+} + \text{H}_2\text{O}$. Previously, Mrazek *et al.*²⁰ proposed a mechanism for the bond forming process observed between CO_2^{2+} and H_2/D_2 forming HCO^+ .



The mechanism for this bond forming process involved three steps. In the first step, addition of the H_2 to the CO_2^{2+} gives a complex. In the second step, a hydrogen

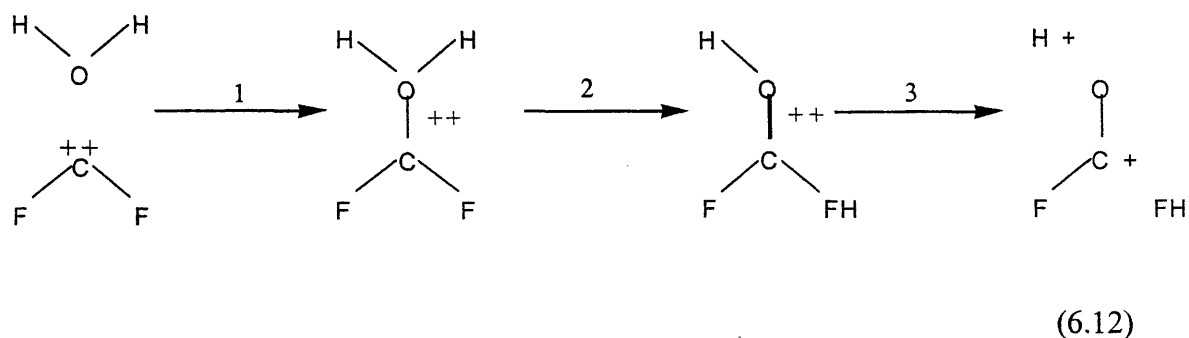
migrates from the carbon atom to an oxygen and the third step sees the fragmentation of the complex. Recently, Lambert and co workers¹⁷ have shown that the bond forming process



proceeds via a similar mechanism to that proposed by Mrazek *et al.*²⁰ for

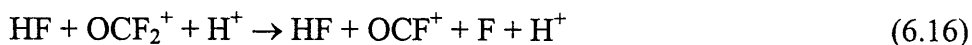
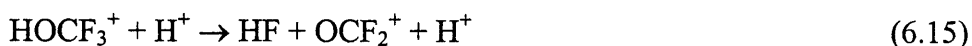


The formation of OCF^+ from CF_2^{2+} and H_2O proceeds via addition of H_2O (step 1 in equation 6.12), migration of a hydrogen (step 2) and finally fragmentation to yield OCF^+ (step 3).



In addition to the elucidation of the mechanism for the formation of OCF^+ from $\text{CF}_2^{2+} + \text{H}_2\text{O}$ using *ab initio* techniques, it has been shown³ that the final fragmentation (step 3) of $\text{H}_2\text{OCF}_2^{2+}$ is a two step process. $\text{H}_2\text{OCF}_2^{2+}$ first undergoes charge separation to H^+ and HOCF_2^+ and then the HOCF_2^+ ion fragments to HF and OCF^+ . This two step mechanism is confirmed by position sensitive coincidence studies carried out on $\text{CF}_2^{2+} + \text{H}_2\text{O}$.¹⁶ These studies have shown H^+ to be isotropically scattered, indicating that the complex is rotating. Further to this scattering, the mutual angle of separation between the HF and the OCF^+ is 180° , showing that the HF and OCF^+ separate after the H^+ has departed from the field of HOCF_2^+ .

For the reaction forming OCF^+ from $\text{CF}_3^{2+} + \text{H}_2\text{O}$, we propose an analogous mechanism to that of $\text{CF}_2^{2+} + \text{H}_2\text{O}$.



That is, formation of an adduct (equation 6.13), charge separation to a light H^+ and a heavier complex HOCF_3^+ (equation 6.14), fragmentation of that complex to OCF_2^+ (equation 6.15) and finally further fragmentation of the complex to OCF^+ . However, it is possible that the steps described in equations 6.15 and 6.16 may occur simultaneously, with HOCF_3^+ directly fragmenting to HF_2 and OCF^+ . Theoretical calculations are needed in order to confirm these proposed mechanisms. If OCF_2^+ were formed in this chemical reaction, then it should be detected by the experiment. However, as mentioned, OCF_2^+ is not detected. The lack of any OCF_2^+ signal may be rationalised by considering the stability and heats of formation of the two ions OCF^+ and OCF_2^+ . The heat of formation of OCF_2^+ is 6.73 eV. This value for OCF_2^+ is lower than the heat of formation of OCF^+ at 7.72 eV. Therefore, OCF_2^+ is thermodynamically more stable than OCF^+ and so should be the dominant bond forming product in the $\text{CF}_3^{2+} + \text{H}_2\text{O}$ system. However, if OCF_2^+ were formed in vibronic states which dissociates to yield OCF^+ and F then this would account for the lack of OCF_2^+ signal. The dissociation limit $\text{OCF}_2^+ \rightarrow \text{OCF}^+ + \text{F}$ lies 1.8 eV above the vibronic ground state of OCF_2^+ . The first electronically excited state of OCF_2^+ in its equilibrium geometry lies 3.1 eV above the vibronic ground state of OCF_2^+ . If OCF_2^+ were formed, during collisions between $\text{CF}_3^{2+} + \text{H}_2\text{O}$, in an electronically excited state, then it would certainly possess sufficient internal energy to dissociate

to yield OCF^+ and F. The possible formation of a vibronically excited OCF_2^+ may well account for its not being detected during the timescale of our experiment.

For the collision system $\text{CF}_2^{2+} + \text{H}_2\text{S}$, the bond forming product SCF^+ was observed, no such evidence for a bond forming process was observed in the collision system $\text{CF}_3^{2+} + \text{H}_2\text{S}$. This lack of SCF^+ may be explained by considering the intensities of the bond forming product signals. The SCF^+ signal in the $\text{CF}_2^{2+} + \text{H}_2\text{S}$ system is considerably weaker than OCF^+ signal in the $\text{CF}_2^{2+} + \text{H}_2\text{O}$ system. The OCF^+ signal in the $\text{CF}_3^{2+} + \text{H}_2\text{O}$ system is less intense than the OCF^+ signal in the $\text{CF}_2^{2+} + \text{H}_2\text{O}$. Therefore, it is reasonable to suppose that, were a bond forming process occurring in the $\text{CF}_3^{2+} + \text{H}_2\text{S}$ system that is analogous to those occurring in the other collision systems, the products ion's signal intensity would be below the detection limits of our apparatus. The question one must ask is why is the cross section for forming SCF^+ in collisions with H_2S markedly smaller than that for forming OCF^+ in collisions with H_2O . Perhaps some barrier exists in one of the mechanistic steps which is more pronounced in the H_2S systems. Indeed, if there were some barrier to forming an intermediate which was larger for the H_2S systems, then the cross section for forming $\text{H}_2\text{SCF}_3^{2+}$ from $\text{CF}_3^{2+} + \text{H}_2\text{S}$ may be so small that the amount of SCF^+ produced is below the detection limits of our experiment and so not observed by us.

6.4.7 Neutral loss

Collision induced neutral loss of the reactant dication involves that dication dissociating to a neutral fragment and a doubly charged fragment. In the past, the appearance energy of this doubly charged fragment has been used to estimate the strength of the cleaved bond.¹⁴ For example, following collisions between CF_3^{2+} and Ar, the neutral loss reaction $\text{CF}_3^{2+} \rightarrow \text{CF}_2^{2+} + \text{F}$ was observed. By plotting the signal

intensity ratios of $\text{CF}_2^{2+}/\text{CF}_3^{2+}$ vs. centre of mass collision energy, the appearance energy of CF_2^{2+} was shown to be 0.6 eV, indicating that the C-F bond strength is 0.6 eV. In this present study of $\text{CF}_3^{2+} + \text{H}_2\text{X}$, the scatter of points in the plots of CF_2^{2+} formed following collisions between CF_3^{2+} and H_2X (Fig.6.5) was too great for a reasonable extrapolation to be made. As a result, no more information could be obtained.

6.5 Conclusion

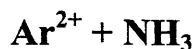
The collision system $\text{CF}_3^{2+} + \text{H}_2\text{X}$ ($\text{X} = \text{O}, \text{S}$) has been studied. It has been shown that, in both systems, the reactivity is dominated by electron transfer. The reaction window algorithm based on the Landau-Zener theory has been used, with qualitative success, to rationalise the presence of the dissociative and non dissociative electron transfer products. Evidence for neutral loss reactivity has also been observed. The bond forming adduct OCF^+ , seen in the $\text{CF}_3^{2+} + \text{H}_2\text{O}$ collision system, has been attributed to a similar mechanism to that observed in the collision system $\text{CF}_2^{2+} + \text{H}_2\text{O}$. The cross section for forming OCF^+ from $\text{CF}_2^{3+} + \text{H}_2\text{O}$ is much smaller than for forming SCF^+ from $\text{CF}_3^{2+} + \text{H}_2\text{S}$. As a result, we are unable to detect SCF^+ in this system with our present experimental apparatus. We also conclude that an excited state of CF_3^{2+} , lying about 5 eV above the ground state, is present in our reactant dication beam in accordance with conclusions made previously in similar experiments.

6.6 References

- 1 C. Ma, M. R. Bruce and R. A. Bonham, *Phys. Rev. A.* **44** (1991) 2921-2934
- 2 D. Kearney and S. D. Price, *Phys. Chem. Chem. Phys.* **5** (2003) 1575-1583
- 3 N. Lambert, N. Kaltsoyannis and S. D. Price, *J. Chem. Phys.* **119** (2003) 1421-1425
- 4 Z. Herman, J. Zabka, Z. Dolejssek and M. Farnik, *Int. J. Mass Spectrom.* **192** (1999) 191-203
- 5 K. A. Newson, N. Tafadar and S. D. Price, *J. Chem. Soc. Faraday Trans.* **94** (1998) 2735-2740
- 6 K. A. Newson and S. D. Price, *Chem. Phys. Lett.* **294** (1998) 223-228
- 7 K. A. Newson and S. D. Price, *Chem. Phys. Lett.* **269** (1997) 93-98
- 8 S. D. Price, M. Manning and S. R. Leone, *J. Am. Chem. Soc.* **116** (1994) 8673-8680
- 9 T. masuoka and A. Kobyashi, *J. Chem. Phys.* **113** (2000) 1559
- 10 T. masuoka, O. Okaji and A. Kobyashi, *Int. J. Mass Spectrom.* **218** (2002) 11
- 11 J. M. G. D. L. Vega and E. S. Fabian, *Int. J. Quan. Chem.* **52** (1994) 947-956
- 12 J. Hrusak, N. Sandig and W. Koch, *In. J. Mass Spectrom.* **187** (1999) 701-706
- 13 N. Kaltsoyannis and S. D. Price, *Chem. Phys. Lett.* **313** (1999) 679-684
- 14 N. Tafadar, N. Kaltsoyannis and S. D. Price, *Int. J. Mass Spectrom.* **192** (1999) 205-214
- 15 S. D. Price, M. Manning and S. R. Leone, *Chem. Phys. Lett.* **214** (1993) 553-558
- 16 S. M. Harper, W. P. Hu and S. D. Price, *J. Chem. Phys.* **121** (2004) Preprint
- 17 N. Lambert, N. Kaltsoyannis and S. D. Price, *J. Chem. Phys.* **119** (2003) 1421-1425
- 18 Z. Herman, *Int. Rev. Phys. Chem.* **15** (1996) 299-324
- 19 Z. Herman, P. Jonathan, A. G. Brenton and J. H. Beynon, *Chem. Phys. Lett.* **141** (1987) 433-442

- 20 L. Mrazek, J. Zabka, Z. Dolejšek, J. Hrusak and Z. Herman, *J. Phys. Chem. A.* **104** (2000) 7294-7303
- 21 L. Landau, *Phys. Z. Sowjetunion.* **2** (1932) 26
- 22 C. Zener, *Proc. Roy. Soc. Lond. Ser. A.* **137** (1932) 696
- 23 J. H. D. Eland, *Chem. Phys.* **11** (1975) 41-47
- 24 J. H. D. Eland, *Int. J. Mass Spectrom. Ion Phys.* **31** (1979) 161-173
- 25 J. H. D. Eland, *Int. J. Mass Spectrom. Ion Phys.* **9** (1972) 397
- 26 S. G. Lias, J. E. Bartmess, J. F. Liebman, J. L. Holmes, R. D. Levin and W. G. Mallard, *J. Phys. Chem. Ref. Data.* **17 S1** (1988) 1-861
- 27 S. G. Lias, R. D. Levin and S. A. Kafafi, *NIST Chemistry WebBook, NIST Standard Reference Database Number 69* (<http://webbook.nist.gov>), (1998)
- 28 S. Lias, *NIST Chemistry WebBook, NIST Standard Reference Database Number 69*, (2000)
- 29 J. E. Reutt, L. S. Wang, Y. T. Lee and D. A. Shirley, *J. Chem. Phys.* **85** (1986) 6928-6939
- 30 A. W. Potts and W. C. Price, *Proc. Roy. Soc. Lond. Ser. A.* **326** (1972) 181

Chapter 7



7.1 Introduction

This thesis has, so far, been concerned mainly with the reactivity of molecular dications colliding with neutral molecules. However, the bimolecular reactivity of atomic dications is also of interest. Indeed, there have been a number of studies involving collisions between doubly charged atoms and neutral species,¹⁻⁶ which have mainly consisted of high energy (keV) collisions where both the dication and the neutral are rare gases.¹⁻⁴ The products of these high energy collisions usually result from an electron transfer from the neutral to the dication. The reactivity of other atomic dications have also been studied and show similar reactivity. For example, experiments carried out by Burns *et al.*, involving high energy collisions between N^{2+} and rare gas atoms, again showed electron transfer reactivity to dominate.⁷ Even in low energy (eV) atomic dication-neutral collision, electron transfer reactivity dominates.^{8,9} However, Tonkyn and co-workers found that, during collisions between titanium dications and alkanes, chemical bonds were formed.⁵ For example, the reaction $\text{Ti}^{2+} + \text{CH}_4 \rightarrow \text{TiCH}_4^{2+}$ was observed.

The doubly charged ion Ar^{2+} has been the subject of a number of studies over the past few years, both as an isolated species^{10,11} and in terms of its bimolecular reactivity.^{1-3,12-14} Ar^{2+} has been observed mainly as a result of photo-ionisation^{10,15-17} and electron impact ionisation.^{18,19} The heat of formation of Ar^{2+} is 43.38 eV.¹⁴ Rejoub *et al.* determined the cross section for forming Ar^{2+} to be $1.8 \times 10^{-17} \text{ cm}^2$ at an electron energy of 100 eV.¹⁸

Collisions between Ar^{2+} and neutral species, at energies between 200 eV and 540 eV, have found, unsurprisingly, that electron transfer dominates the reactivity.¹⁻³

However, at collision energies below about 100 eV, bond forming reactivity is observed in some cases.²⁰ Collisions between Ar^{2+} and neutral molecules have shown doubly charged adducts to be formed. For example, collisions between Ar^{2+} and O_2 , N_2 , CO_2 and CO form ArO^{2+} , ArN^{2+} , and ArC^{2+} respectively.²⁰ Collisions between Ar^{2+} and O_2 also yielded ArO^+ .²⁰

In this chapter, we report the results of collisions between Ar^{2+} and NH_3 at low (eV) collision energies. The electron transfer reactivity we observe is discussed in terms of the Landau-Zener “reaction window” model. In addition, the bond forming products ArN^+ and ArNH^+ are observed. We find that the ratio of ArN^+ to ArNH^+ formed increases with collision energy. To our knowledge, ArNH^+ is the first example of the formation of a triatomic monocation as a result of a collision between a rare gas dication and a neutral.

7.2 Electron transfer reactivity results and discussion

Mass spectra were recorded following collisions between Ar^{2+} and NH_3 at collision energies between 0.3 eV and 4.2 eV in the centre of mass frame (1 eV to 14 eV in the laboratory frame). The identities of the product ions formed following collisions between dications and neutrals can offer considerable information about what types of reactions occur. We observe, in the mass spectrum, the presence of signals corresponding to NH_3^+ and Ar^+ . These product ions clearly arise as a result of non-dissociative single electron transfer. Also present in the mass spectrum are signals corresponding to NH_2^+ , NH^+ , N^+ and H^+ . These ions may all be attributed to dissociative electron transfer. The bond-forming adducts ArNH^+ and ArN^+ are also present in the mass spectrum. These two bond-forming product channels are discussed in detail later in this chapter.

7.2.1 Electron transfer reactivity

The methodology used to extract the integral cross sections from measured signal intensities in the mass spectra for the various reaction channels, has been described in detail previously in this thesis. This data reduction is in two parts. The first part takes into account the mass discriminating effects associated with the time of flight mass spectrometer. Briefly, when two ions travel across the source region of the TOFMS with different kinetic energies, and are accelerated down the flight tube of the TOFMS, they may travel different distances perpendicular to the direction of the TOFMS before reaching the detector. This difference in distances travelled may result in some ions missing the detector. As a result, ions of different energies will be detected with different efficiencies. By considering the physical dimensions of the mass spectrometer, we are able to model how far an ion will travel perpendicular to the axis of the TOFMS during the time taken to travel along the axis of the flight tube. We can determine whether or not an ion will strike the walls of the flight tube and so, determine the portion of the source region which is imaged onto the detector. If an ion is formed in this “imaged” region, it will reach the detector. We may then correct for the detection efficiencies of various ions. The second part of this data reduction involves consideration of signal saturation experienced by the constant fraction discriminator (CFD) at higher dication fluxes. By accounting for this saturation at the CFD and appreciating that, because the product ions account for only a small fraction of the total ion current, this saturation only affects the unreacted reactant dication signal, we are able to accurately determine the true intensity of the unreacted reactant dication signal from the observed dication signal intensity within the mass spectrum. As has been shown in chapter 4, accurately measuring the flux of

the unreacted reactant dication allows us to extract an integral cross section, in arbitrary units, from our raw data. However, for our collisions between dications and neutrals, electron transfer integral cross sections for forming product ions derived from the reactant dication are not directly comparable with product ions derived from the neutral. Briefly, product ions derived from the reactant dication are forward scattered in the centre of mass frame whereas product ions derived from the neutral are backward scattered in the centre of mass frame. This difference in scattering direction between these two classes of product ion means that any ions that reach the detector are sampled from different areas of the source region of the TOFMS. Due to the nature of our experiment, these different areas of the TOFMS will possess different neutral gas pressures. Our experiment does not allow us to accurately measure the absolute neutral gas pressure in the collision region. However, by maintaining a good quality incident dication beam and keeping the pressure of the neutral gas constant throughout, it is possible to extract a value which is directly proportional to the absolute reaction cross section with a constant of proportionality which does not vary between experiments. This constant of proportionality is a function of the neutral gas pressure in the collision region and that pressure varies throughout the collision region. Ions derived from the neutral, which are backward scattered in the centre of mass frame, are formed in the centre of the collision region where the neutral gas is of lower pressure. Ions derived from the reactant dication being forward scattered in the centre of mass frame, are formed in an area of the collision region where the neutral gas is of higher pressure. As a result of this difference in neutral gas pressure, the integral cross sections for forming ions derived from the neutral and ions derived from the dication are not directly comparable. Consequently, to emphasise this difference, integral cross sections for forming ions

derived from the dications are denoted σ' whereas the integral cross section for forming ions derived from the neutral have the value σ'' . These two quantities are independently indicative of the trends in the absolute cross sections for the electron transfer processes. It should be noted that, in the past, integral reaction cross sections have been determined only for the monocations derived from the dication (σ').²¹ This is the first study where integral reaction cross sections are determined and studied in detail for the less energetic monocations derived from the neutral (σ'').

Product ion	H ⁺	N ⁺	NH ⁺	NH ₂ ⁺	NH ₃ ⁺	Ar ⁺	ArN ⁺	ArNH ⁺
10 ⁶ σ' and σ'' (arb. units)	96 (12)	29 (4)	372 (62)	437 (66)	518 (125)	7940 (1387)	50 (10)	35 (9)

Table 7.1 The integral reaction cross section (σ' for Ar⁺, ArN⁺ and ArNH⁺ and σ'' for NH_n⁺) for forming product ions during collisions between Ar²⁺ and NH₃.

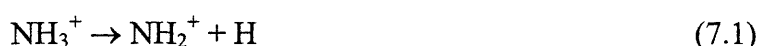
Once the integral reaction cross sections for forming each of the dissociative and non dissociative electron transfer products have been determined, representative values of which are given in table 7.1, we compare those measured cross sections with cross sections calculated using the Landau-Zener reaction window model. It should be noted that the experimentally determined cross sections, although having units of area, are given in arbitrary units whereas the calculated cross sections are in Å². Therefore, we compare branching ratios of experimental and calculated cross sections.

The Landau-Zener theory is a useful tool with which to model a single electron transfer from a neutral to a dication and has been used successfully in the past to model electron transfer reactions of molecular dications.^{21,22} A full description of this Landau-Zener model has been given in detail previously. Here, we use this reaction window algorithm to model a single electron transfer from NH₃ to Ar²⁺. In doing so,

we predict which fragments of the product ion NH_3^+ will be observed in our mass spectrum.

The LZ reaction window model allows us to estimate the level of internal energy, that is electronic and vibrational excitation, with which NH_3^+ may be formed following an electron transfer reaction. If NH_3^+ is formed with sufficient internal energy for it to lie above some dissociation threshold, then it will dissociate to yield fragment ions. These dissociative electron transfer processes compete with non-dissociative electron transfer processes as well as a number of other classes of reaction detailed in chapter 1. In order to account for the branching ratios of the various dissociative and non-dissociative electron transfer products, it is necessary to understand the stabilities of the various electronic and vibrational states of NH_3^+ .

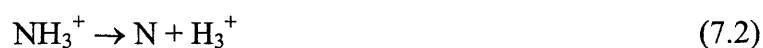
In the past, the stability of an ion has been determined by photoelectron-photoion coincidence (PEPICO) spectroscopy^{21,23,24}. PEPICO involves ionising the target molecule with a photon of known energy. The ejected photoelectron is then detected in coincidence with the photoion. By increasing the energy of the incident photon, it is possible to determine the energy at which the parent photoion signal diminishes and a daughter ion signal increases. The energy at which this change in signal intensities occurs is the dissociation limit for that particular fragmentation pathway. PEPICO studies of NH_3^+ performed by Song *et al.* have shown the value for the dissociation limit, $D_0(\text{NH}_2^+ + \text{H})$ for the bound electronic ground (X) state of NH_3^+ to be 5.6 eV.²⁵ The (X) state of NH_3^+ and lower vibrational levels of the first excited (A) state of NH_3^+ lie below this first dissociation limit



and so are stable (non-dissociative). The energy of the first dissociation limit for NH_3^+ is confirmed by the fact that only the ground (X) state and lower vibrational

levels of the first excited (*A*) state of NH_3^+ exhibit vibrational fine structure in the photoelectron spectrum, as higher vibrational levels quickly dissociate. The PEPICO study performed by Song *et al.*²⁵ only covers the dissociation of NH_3^+ to yield NH_2^+ close to its threshold. It is therefore necessary to fall back on the relative energetics of the electronic states of NH_3^+ in order to predict the fates of the various higher vibronic states of NH_3^+ . A photoelectron spectrum of NH_3^+ is available showing the population of low lying states of NH_3^+ .²⁶ Using the adiabatic ionisation potentials and heats of formations of the NH_3^+ fragments, we can calculate the various dissociation limits for NH_3^+ .^{27,28}

The equilibrium geometry of the first excited (*A*) state of NH_3^+ lies 4.5 eV above the equilibrium geometry of the electronic ground (*X*) state of NH_3^+ . From the photoelectron spectrum of NH_3 , it is clear that the Franck-Condon region for the transition between NH_3 and the (*A*) state of NH_3^+ lies from 4.5 eV to 9.02 eV above the (*X*) state of NH_3^+ . Higher vibrational levels of this (*A*) state of NH_3^+ lie above a number of other dissociation limits. The limit corresponding to



lies 6.66 eV above the ground state of NH_3^+ , the limit



lies 7.68 eV above ground state NH_3^+ and the limit



lies 8.12 eV above the ground state of NH_3^+ . It is clear that the (*A*) state of NH_3^+ may fragment to give either H_3^+ , NH^+ or H^+ , depending on the vibrational excitation of the NH_3^+ ion. We assume that any ion lying in a vibronic state which is directly above a particular dissociation asymptote will fragment to those products. This assumption has been shown to hold in PEPICO studies of CO_2 , H_2O and H_2S .^{23,24,29}

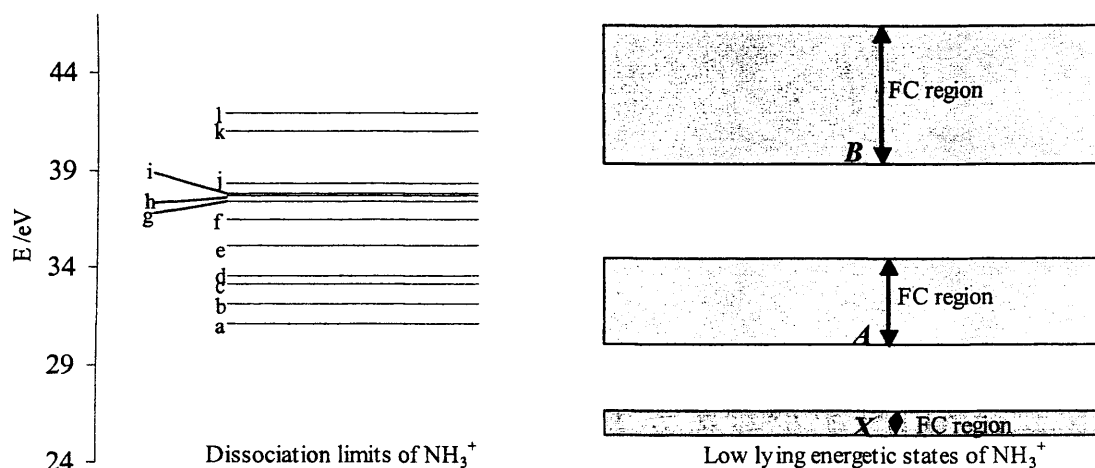


Figure 7.2 Energies of the first three electronic states of NH_3 (right hand side). The upper and lower limit of each electronic state is the Franck-Condon region for forming that particular state of NH_3^+ . The left hand side of the diagram shows the positions of the dissociation limits for fragmentation of NH_3^+ . The dissociation limits are as follows: a) $\text{NH}_2^+ + \text{H}$. b) $\text{N} + \text{H}_3^+$. c) $\text{NH}^+ + \text{H}_2$. d) $\text{NH}_2 + \text{H}^+$. e) $\text{NH} + \text{H}_2^+$. f) $\text{N} + \text{H}^+ + \text{H}_2$. g) $\text{NH}^+ + 2\text{H}$. h) $\text{N}^+ + \text{H} + \text{H}_2$. i) $\text{NH} + \text{H}^+ + \text{H}$. j) $\text{N} + \text{H} + \text{H}_2^+$. k) $\text{N} + \text{H}^+ + 2\text{H}$. l) $\text{N}^+ + 3\text{H}$. The energy scale is based on the heats of formation of the proposed fragments

The equilibrium geometry of the second excited (B) state of NH_3^+ lies 13.8 eV above the equilibrium geometry of the (X) state of NH_3^+ . The available HeII photoelectron spectrum (where $h\nu = 40.8$ eV) of NH_3^{26} does not show the entire (B) state of NH_3^+ as it does not cover binding energies higher than 27 eV. As a result, the Franck-Condon region for this transition between NH_3 and NH_3^+ (B) is not known. However, as only lower vibrational levels of the (B) state of NH_3^+ fall within our Landau-Zener reaction window, knowledge of the full Franck-Condon region is not required. As a rough guide, in figure 7.2, the Franck-Condon region for the B state of NH_3^+ has been estimated from the shape of the peak in the photoelectron spectrum, assuming that the signals are symmetrical. Lower vibrational levels of this second (B) electronic state of NH_3^+ lie above the dissociation limit



which falls 12.87 eV above the vibronic ground state of NH_3^+ . However, another dissociation limit,



lies at 12.20 eV above the ground state of NH_3^+ . Higher vibrational levels of the (B) state of NH_3^+ also lie above the dissociation limits



at 15.57 eV above the (X) state of NH_3^+ and



at 16.50 eV above the (X) state of NH_3^+ . Therefore, vibronic levels of NH_3^+ in its (B) state lying above these dissociation limits will dissociate to yield these products.

Reaction exothermicities for forming product ions in their various electronic states are calculated using excitation energies derived from photoelectron spectra.²⁶ These reaction exothermicities coupled with knowledge of the stability of each electronic state of our product ions allow the prediction of which ion signals, arising as a result of electron transfer, should be present within our mass spectra. These predictions are shown in table 7.3.

Electronic state of Ar^+ product	Electronic state of NH_3^+ product					
	X ($\rightarrow\text{NH}_3^+$)		A ($\rightarrow\text{NH}_3^+, \text{NH}_2^+, \text{NH}^+$)		B ($\rightarrow\text{NH}^+, \text{N}^+, \text{H}^+$)	
	$\Delta H/\text{eV}$	σ	$\Delta H/\text{eV}$	σ	$\Delta H/\text{eV}$	σ
^2P	17.43	0	12.91	0	3.62	26.4
^2S	3.95	17.8	-0.57	0	-9.86	0
^4D	1.03	0	-3.49	0	-12.79	0

Table 7.3a Electron transfer reactions from Ar^{2+} in its ^3P state

Electronic state of Ar^+ product	Electronic state of NH_3^+ product					
	X ($\rightarrow\text{NH}_3^+$)		A ($\rightarrow\text{NH}_3^+, \text{NH}_2^+, \text{NH}^+$)		B ($\rightarrow\text{NH}^+, \text{N}^+, \text{H}^+$)	
	$\Delta H/\text{eV}$	σ	$\Delta H/\text{eV}$	σ	$\Delta H/\text{eV}$	σ
^2P	19.17	0	14.65	0	5.36	1.1
^2S	5.69	0.65	1.17	0	-8.12	0
^4D	2.76	19.8	-1.76	0	-11.05	0

Table 7.3b Electron transfer reactions from Ar^{2+} in its ^1D state.

Electronic state of Ar ⁺ product	Electronic state of NH ₃ ⁺ product					
	X (→NH ₃ ⁺)		A (→NH ₃ ⁺ , NH ₂ ⁺ , NH ⁺)		B (→NH ⁺ , N ⁺ , H ⁺)	
	ΔH/eV	σ	ΔH/eV	σ	ΔH/eV	σ
² P	21.56	0	17.04	0	7.74	0
² S	8.08	0	3.56	28.34	-5.74	0
⁴ D	5.15	1.65	0.63	0	-8.66	0

Table 7.3c Electron transfer reactions from Ar²⁺ in its ¹S state.

Table 7.3 Exothermicities and calculated cross sections for forming Ar⁺ and NH₃⁺ from Ar²⁺ + NH₃ in various electronic states. Also shown are predicted fragmentation pathways of NH₃⁺. Table a) is for electron transfer reactions from Ar²⁺ in its ³P state, Table b) is for Ar²⁺ (¹D) and Table c) is for Ar²⁺ (¹S). It should be noted that the transition resulting in Ar⁺ in the ⁴D state is not allowed.

From table 7.3 (a), it is clear that, following the electron transfer, Ar⁺ [²P] should be formed with NH₃⁺ [*B*] and Ar⁺ [²S] with NH₃⁺ [*X*]. From the information outlined above on the stability of each state of NH₃⁺, it is clear that we should observe NH₃⁺ ions from the (*X*) state of NH₃⁺. As mentioned above, the (*B*) state of NH₃⁺ lies directly above the asymptote NH₃⁺ → N + H + H₂⁺. However, slightly below this dissociation limit, there lie the dissociation limits NH₃⁺ → NH⁺ + 2H and NH₃⁺ → N⁺ + H + H₂. As we observe only NH⁺, NH₂⁺ and N⁺ fragments in the mass spectrum, it is reasonable to suppose that some dynamical restrictions to NH₃⁺ → N + H + H₂⁺ may cause only the NH₃⁺ → NH⁺ + 2H and NH₃⁺ → N⁺ + H + H₂ fragmentation pathways to be favoured. Indeed, these dynamical restrictions may even possibly account for the formation of NH₂⁺, the dissociation asymptote for which lies 8.15 eV below the (*B*) state of NH₃⁺, although such processes involving parent ions of small molecules fragmenting to products, the asymptote for which lies below many other dissociation asymptotes, has not been observed before. However, larger molecular ions may dissociate statistically to lower asymptotes. In short, fragments of the (*B*) state of NH₃⁺ make contributions to the ion yields of N⁺, NH⁺

and perhaps NH_2^+ although, as shown below, these ions do not come exclusively from this NH_3 (*B*) state.

The Landau-Zener reaction window model for reactions of the ^3P state of Ar^{2+} may clearly account for the presence of NH_3^+ , and NH^+ in the mass spectrum. In addition to the above rational, the presence of NH_2^+ in the mass spectrum may be accounted for by considering the other electronic states of Ar^{2+} which are present within the dication beam. It is certainly reasonable to assume that the predominant electronic state of Ar^{2+} present in the beam is the ground state (^3P). This has been shown to be the case for Ne^{2+} where the majority of the Ne^{2+} ions are in the ^3P state with about 30% being in the ^1D state.³⁰⁻³² This ratio is consistent with the statistical ratios of the degeneracy of the spin orbit states (9:5:1) used in other studies. These excited states of Ar^{2+} , ^1D and ^1S , lie 1.74 eV and 4.12 eV respectively above this ground electronic (^3P) state. The exothermicity for forming Ar^+ (^2S) with NH_3^+ (*A*) from Ar^{2+} (^1S) and NH_3 falls within the reaction window of exothermicities. As mentioned, higher vibrational levels of the (*A*) state of NH_3^+ will dissociate to yield NH_2^+ . Thus, the formation of Ar^+ from the (^1S) state of Ar^{2+} may well qualitatively account for the presence of NH_2^+ observed in the mass spectrum. Obviously there are higher lying states of Ar^{2+} but these lie much higher in energy and are not thought to be present in the dication beam in large enough quantities to be significant.

In short, we can see from Table 7.3, that reactions involving Ar^{2+} (^3P) will form NH_3^+ (*X*) which is stable, and NH_3^+ (*B*) which will form NH^+ and N^+ . NH_2^+ probably arises as a result of electron transfer reactions involving Ar^{2+} (^1S) forming NH_3^+ (*A*).

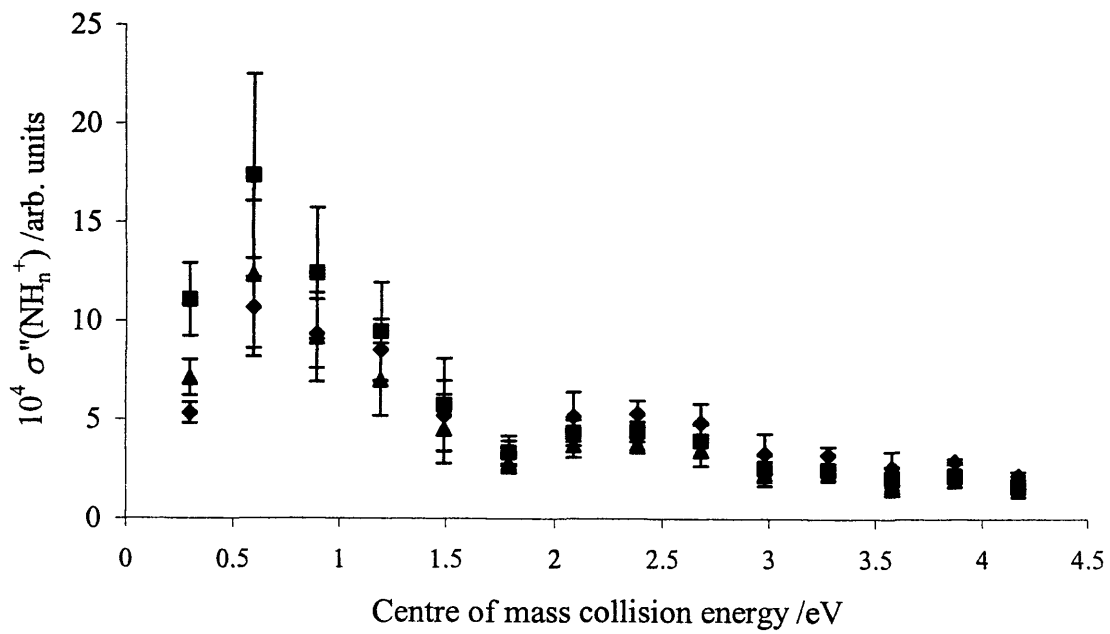


Figure 7.4 The variation in integral cross section σ'' for forming NH^+ (\blacktriangle), NH_2^+ (\blacksquare) and NH_3^+ (\blacklozenge) for collisions between Ar^{2+} and NH_3

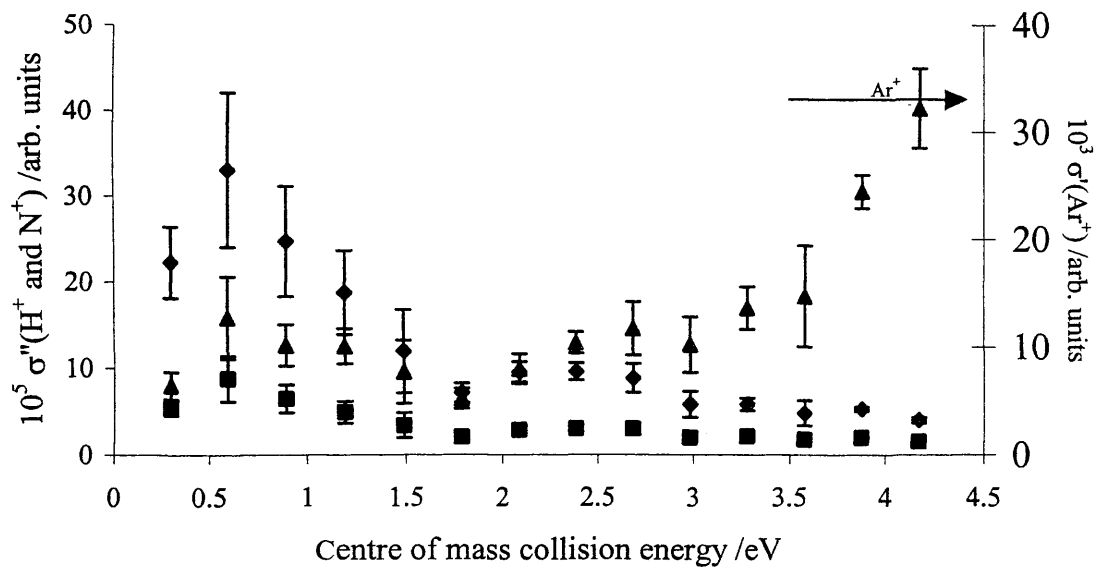


Figure 7.5 The variation in integral cross section, σ'' and σ' , with collision energy for forming H^+ (\blacklozenge), N^+ (\blacksquare) and Ar^+ (\blacktriangle) for collisions between Ar^{2+} and NH_3

The variation in the integral cross sections with collision energy are given in figures 7.4 and 7.5. The plots in figures 7.4 and 7.5 show that the cross sections for all of

these electron transfer reactions although showing some variation over the range of collision energies studied, are of the same order of magnitude across the whole energy range. This energy independence has often been shown to be the case in previous studies of this nature.^{21,33} It should be noted that the cross sections for forming the electron transfer products appear to increase at low collision energies in the case of the monocations derived from the neutral (NH_n^+) and towards higher collision energies in the case of the monocation derived from the dication (Ar^+). This variation in the corrected data with collision energy may be an artefact attributed to the magnitude of the ion's velocity across the source region of the TOFMS. Following an electron transfer reaction, Ar^+ , being forward scattered in both the centre of mass frame and the laboratory frame over the range of energies studied, will have the greatest velocity following high energy collision; that is collision energies of 14 eV in the laboratory frame. Conversely, NH_3^+ and its fragments are backward scattered in the centre of mass frame, and the laboratory frame, at the energies studied. Only at laboratory collision energies above about 35 eV, do our calculations show that NH_3^+ and its fragments will be forward scattered in the laboratory frame. This backward scattering of NH_n^+ in the laboratory frame, at the energies studied here (<14 eV), means that NH_3^+ and its fragments will have their highest laboratory velocities (backwards) at low collision energies. We calculate that NH_n^+ will have a laboratory velocity, backward towards the ionisation source, of 5300 ms^{-1} at a laboratory collision energy of 2 eV. This velocity falls to 1700 ms^{-1} at a laboratory collision energy of 14 eV. In comparison, we calculate Ar^+ to possess a laboratory velocity, in the direction of the dication beam, of 5800 ms^{-1} at a laboratory collision energy of 2 eV. This velocity rises to 8900 ms^{-1} at 14 eV. In both cases, when the rise in the data with collision energy occurs, the ion is travelling with

higher velocity across the source region of the TOFMS. At these higher velocities, the portion of the source region which is imaged onto the detector, that is the effective region of detection, is much smaller than when the ion is at low laboratory velocities. As a result, at these high product ion laboratory velocities, the amount by which the observed ion intensities are corrected is greater. We assume in our model, that the product ions are perfectly forward or backwards scattered following a collision and that the kinetic energy release of the two monocations following the collision is 7 eV. However, these assumptions may be an oversimplification. If a product ion is not perfectly forward or backward scattered, as assumed in our model, the velocity in the direction perpendicular to the axis of the TOFMS may be less than anticipated. If the velocity of an ion across the source region of the TOFMS is indeed less than we calculate, then the length of the source region imaged onto the detector may be larger than our model predicts. If this is the case, and, at higher ion velocities, we are underestimating the length of the source region imaged onto the detector, then the cross sections we extract from the raw data may be overestimated at higher ion velocities. That is, high energy collisions for ions derived from the dication and low energy collisions for ions derived from the neutral collision partner. In summary, the cross section, although not completely independent of collision energy, does not vary greatly. In the past, this method of extracting integral reaction cross sections from our data has only been carried out for the monocations derived from the reactant dication.²¹ The monocations derived from the neutral, being backward scattered in both the centre of mass frame and the laboratory frame, are much less energetic compared to ions derived from the neutral. Our method for extracting the integral reaction cross sections for these slow, backward scattered ions may not be as robust as for ions derived from the reactant dication. As for ions

derived from the reactant dication, the integral reaction cross section is independent of collision energy for slower collisions up to about 3.5 eV (Fig 7.5) in agreement with other work.³⁴

7.3 Bond forming reactions, results and discussion

The ions ArN^+ and ArNH^+ we observe, corresponding to $m/z = 54$ and 55 , respectively, clearly come from bond-forming chemical reactions. Representative mass spectra, as a function of collision energy, are shown in Figure 7.6.

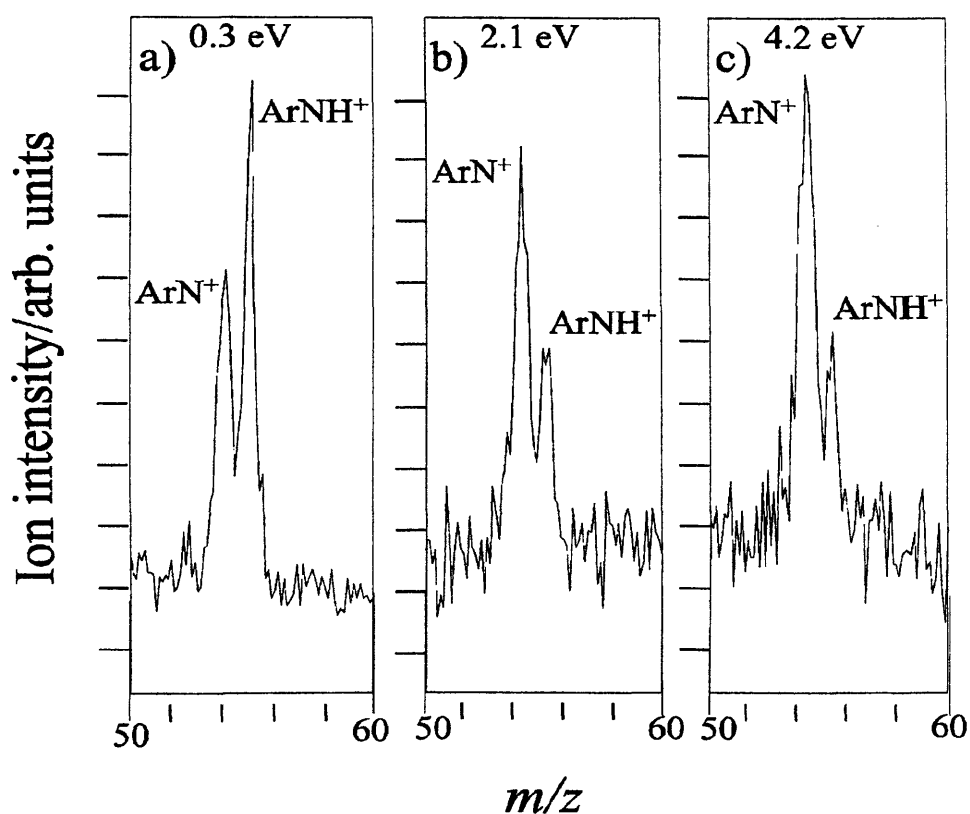


Figure 7.6 Mass spectra at (a) 0.3, (b) 2.1, and (c) 4.2 eV collision energy in the center-of-mass frame showing the signals corresponding to ArN^+ and ArNH^+ detected following collisions of Ar^{2+} with NH_3 . The spectra clearly show that the ratio of ArN^+ to ArNH^+ increases with increasing collision energy. Processing the intensities of the ArN^+ and ArNH^+ ions in these spectra indicates that, as the mass spectra show, the sum of the reactive cross sections for forming these product ions is constant, within experimental error, over this range of collision energies.

As is often the case, the cross sections for forming these new adduct ions are small as compared with those of the electron-transfer reactions observed in the same

collision system. For example, the total signal arising from ArN^+ and ArNH^+ is only approximately 1% of the signal arising from the electron-transfer product Ar^+ .

As has been discussed previously in this thesis, we must always consider the possibility that mass discriminating effects operate in our TOFMS apparatus. However, as shown below, we are confident that such effects do not significantly affect the relative detection efficiency of ArN^+ and ArNH^+ in the present experiments. As described above, mass discrimination between different product ions can arise in our apparatus as a result of the differing kinetic energies that these ions can possess perpendicular to the axis of the TOFMS. A significant velocity component transverse to the axis of the TOFMS may result in ions striking the walls of the drift tube and not reaching the detector. Ions with different transverse kinetic energies will not travel the same transverse distance as they fly down the TOFMS. Thus, there is the possibility of varying fractions of the product ions being detected, a different detection efficiency for ions of different mass. To estimate any variations in detection efficiency for the product ions, we can calculate the length of the source region from which ions reach the detector, for a given transverse kinetic energy of the ion. To estimate the transverse kinetic energy of the product ions of dication reactions, we use the fact that the kinetic energy release for these reactions is dominated by electrostatic repulsion, giving an energy release of approximately 7 eV, and these reactions are experimentally observed to involve forward scattering.³³⁻

³⁶ When we correct our mass spectral data in the above manner, to allow for any transverse ion losses, we produce relative ion intensities in good agreement with other measurements in the literature.²¹ However, for the detection of ArN^+ and ArNH^+ , because the ions have very similar masses, the relative discrimination between these ions is small. For example, given the mechanistic conclusions

presented below, we consider the ArN^+ and ArNH^+ to be formed via a charge separating dissociation of ArNH_3^{2+} to $\text{ArNH}_2^+ + \text{H}^+$, with the ArNH_2^+ subsequently dissociating sequentially to yield ArNH^+ and eventually ArN^+ . For this mechanism, we calculate that our detection efficiencies as a function of center-of-mass kinetic energy are the same (within 3%) for ArN^+ and ArNH^+ . Hence, we conclude that our relative detection efficiency of ArN^+ and ArNH^+ is the same within experimental error over the experimental range of collision energies we employ. Identical conclusions have been reached before for the relative detection efficiency in our apparatus of product ions with similar masses, resulting in experimental data which agree well with those in the literature.³⁷

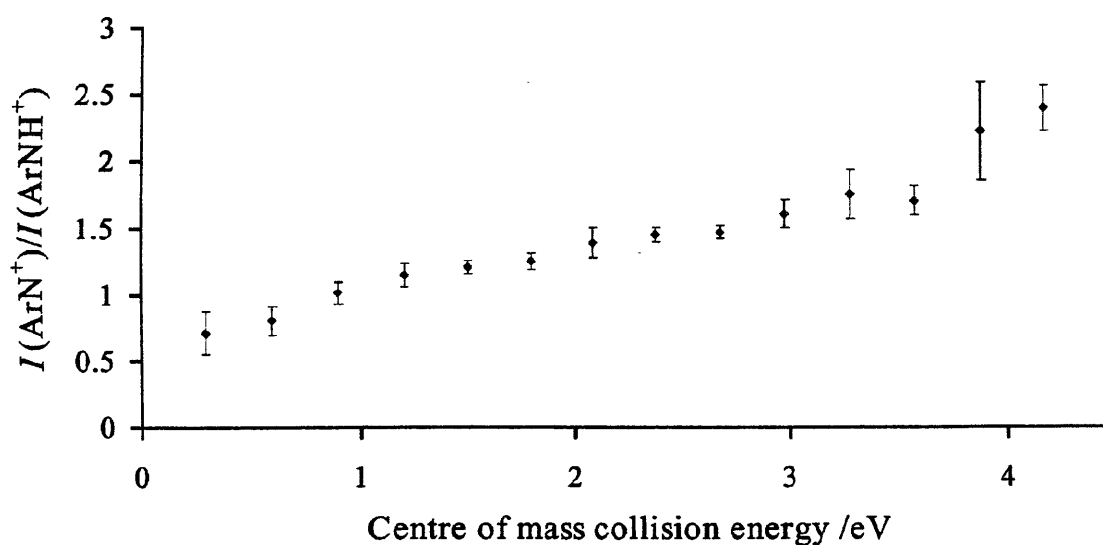


Figure 7.7 A plot of $I(\text{ArN}^+)/I(\text{ArNH}^+)$ versus center of mass collision energy. $I(\text{ArN}^+)/I(\text{ArNH}^+)$ clearly increases with collision energy.

Hence, we consider the ratio of intensities $I[\text{ArN}^+]/I[\text{ArNH}^+]$, which we derive from our mass spectra to be representative of the ratio of the cross sections of the reactive processes forming these ions. Figure 7.7 shows the ratio of the bond-forming product ion intensities, $I[\text{ArN}^+]/I[\text{ArNH}^+]$, as a function of collision energy. The figure clearly shows that $I[\text{ArN}^+]/I[\text{ArNH}^+]$ increases with increasing collision energy.

Figure 7.7 demonstrates that an increase in the ArN^+ ion yield is accompanied by a corresponding decrease in the ArNH^+ ion yield. This variation is consistent with ArN^+ being formed via the dissociation of ArNH^+ .

7.3.1 Computational results

Figure 7.8 shows the stationary points calculated along the PES of the reaction of Ar^{2+} with NH_3 to produce ArNH^+ and ArN^+ .³⁸ The mechanism first involves the formation of the Ar-N bond to give ArNH_3^{2+} , the global minimum for the pathway. This is followed by loss of a proton from the complex via transition state 1 with an activation energy of 5.74 eV to give $\text{ArNH}_2^+ + \text{H}^+$. An H atom then dissociates from ArNH_2^+ to leave $\text{ArNH}^+ + \text{H}$. The last remaining H atom can also dissociate from ArNH^+ , leaving $^3\text{ArN}^+$ and an H atom in their ground states. The final products are, hence, $^3\text{ArN}^+ + \text{H}^+ + 2\text{H}$. For each stationary point, geometric parameters and symmetries, calculated by Lambert and co-workers³⁸, are given in Table 7.9.

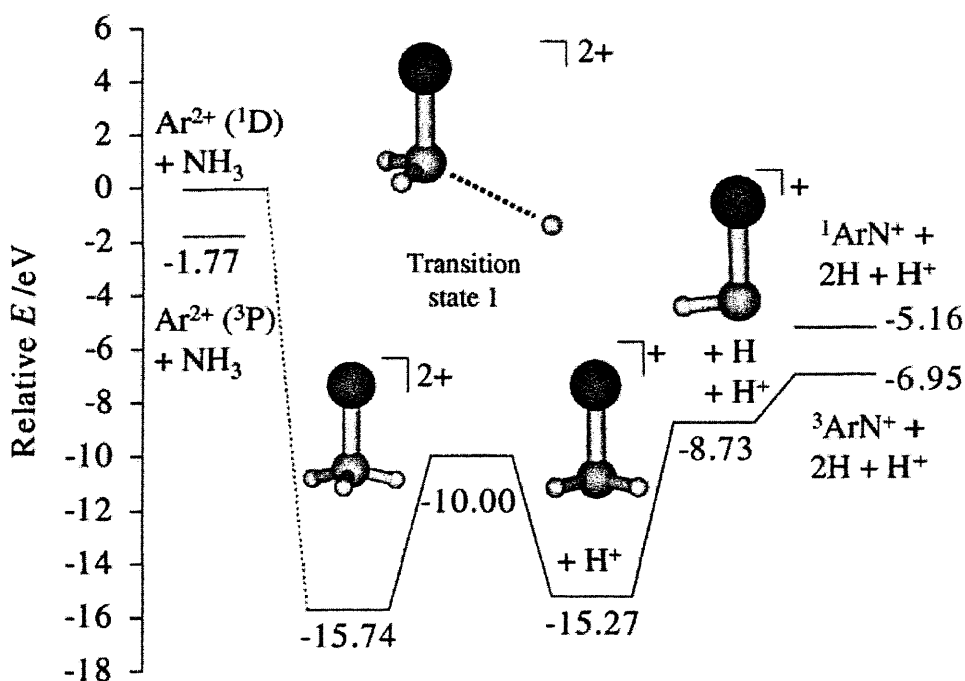


Figure 7.8 The calculated stationary points on the potential energy surface for the reaction $^1\text{Ar}^{2+} + \text{NH}_3 \rightarrow \text{ArN}^+ + \text{H}^+ + 2\text{H}$

The calculated mechanism shown in Figure 7.8 confirms that ArNH^+ and ArN^+ are formed from the same reactive channel, as indicated by the experimental results. It is interesting to note that the bond-forming dication complex ArNH_3^{2+} is found to be stable with respect to dissociation to $\text{Ar}^+ + \text{NH}_3^+$ only when formed in the singlet state; attempts to converge a geometry optimization to a stable triplet structure were unsuccessful. Such an effect is not surprising when one considers that the lowest energy electronic configuration of the triplet ArNH_3^{2+} complex involves the promotion of an electron from a bonding to an antibonding orbital, lowering the Ar-N bond order and increasing the total energy of the complex. Therefore, it appears that only singlet states of Ar^{2+} , not the ground triplet state, contribute to bond-forming reactivity in this system.

Structure	Ar-N	N-H	Ar-N-H	H-N-H
$^1\text{NH}_3$		1.022 [3]		105.1° [3]
$^1\text{ArNH}_3^{2+}$	1.817	1.056 [3]	105.0° [3]	113.6° [3]
Transition state 1 (singlet)	1.863	1.042 [2], 2.811	98.61° [2], 118.9°	115.3° [3], 107.6°
Transition state 2 (singlet)	1.825	1.056 [2], 2.522	99.87°, 126.1°	134.1°
$^1\text{ArNH}_2^+$	1.951	1.044 [2]	95.80° [2]	104.6°
$^2\text{ArNH}_2^{2+}$	1.737	1.065 [2]	114.1° [2]	132.0°
$^2\text{ArNH}^+$	1.911	1.059	96.05°	
$^3\text{ArN}^+$	1.886			
$^1\text{ArN}^+$	1.841			

Table 7.9 Geometric parameters of CASSCF-optimized structures on the singlet potential energy surface for $\text{Ar}^{2+} + \text{NH}_3 \rightarrow ^3\text{ArN}^+ + \text{H}^+ + 2\text{H}$ (See Figures 7.8 and 7.12). All bond distances are in angstroms. The number of degenerate bond lengths and angles are given in square brackets. No symmetry constraints were imposed during the calculations

As can be seen in Figure 7.8, breaking an N-H bond in the ArNH_2^+ ion requires an excitation of 6.54 eV, and breaking the N-H bond in the ArNH^+ complex requires an additional 1.78 eV. The reactants lie at an energy of 15.27 eV above the $\text{ArNH}_2^+ + \text{H}^+$ asymptote; therefore, every reactive event in principle begins with enough energy

to reach completion and form ArN^+ . However, such an analysis neglects the energy removed from the system, in the form of kinetic energy, during the charge separating dissociation of ArNH_3^{2+} to form ArNH_2^+ and H^+ . The measured kinetic energy release distributions for such processes are typically centered around 6-8 eV, with a width of several eV.^{33,34,39} The loss of such large amounts of energy significantly reduces the internal energy content of the ArNH_2^+ ion. Specifically, for collisions at a centre-of-mass energy of 0 eV, the charge-separating dissociation will reduce the internal energy contents of the ArNH_2^+ ions to a range of values from about -6 to -8 eV on the energy scale in Figure 7.8. Only those ArNH_2^+ ions that are formed with an internal energy of 6.95 eV or greater will proceed to the product asymptote ${}^3\text{ArN}^+ + \text{H}^+ + 2\text{H}$, while those ArNH_2^+ ions formed with less than -6.95 eV will only go as far as the $\text{ArNH}^+ + \text{H}^+ + \text{H}$ asymptote. With increasing collision energy, the residual internal energy of ArNH_2^+ will be higher, increasing the probability of complete dissociation to ArN^+ . Thus, increasing the collision energy increases the yield of ArN^+ and correspondingly decreases the yield of ArNH^+ , reproducing the behavior that we observe experimentally. Such sequential dissociations have been observed before for similar endothermic fragmentation steps in the bond-forming reactions between rare gas ions and molecules.⁴⁰⁻⁴²

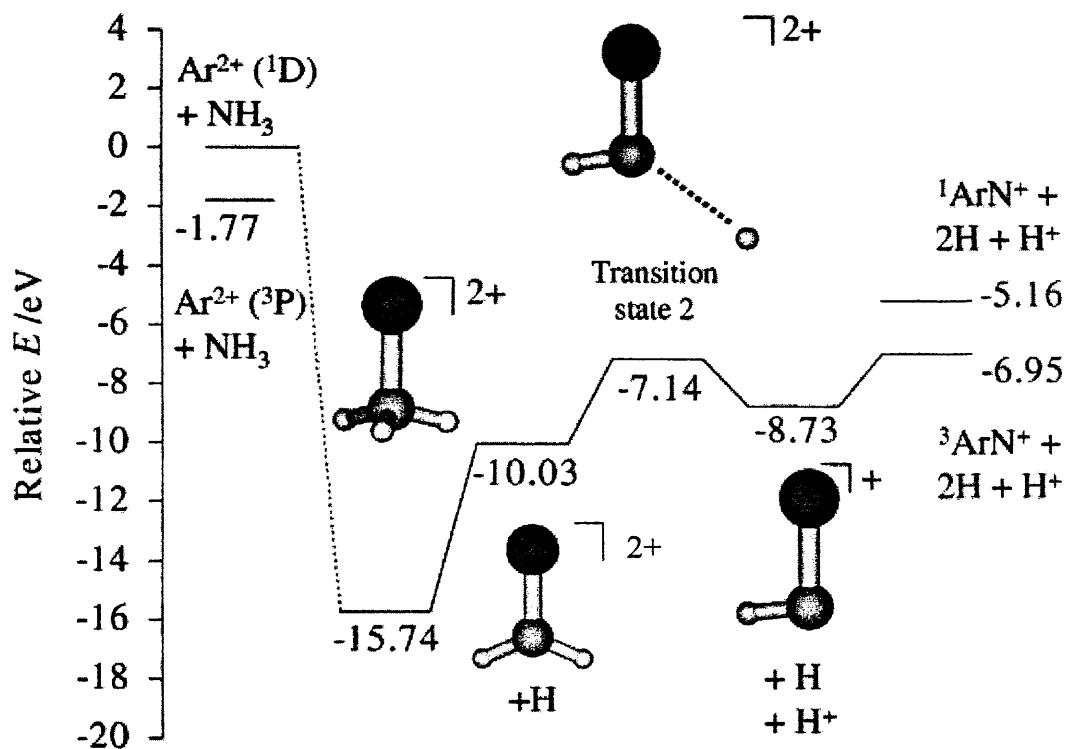


Figure 7.10 A schematic representation of the stationary points on the potential energy surface of an alternate pathway for the reaction ${}^1\text{Ar}^{2+} + \text{NH}_3 \rightarrow {}^3\text{ArN}^+ + \text{H}^+ + 2\text{H}$, in which the adduct decomposes via neutral loss, not charge separation.

Lambert *et al.*³⁸ also considered an alternative pathway to the formation of ArN^+ and ArNH^+ that involves neutral loss in the dissociation of ArNH_3^{2+} rather than charge separation. The stationary points along this alternative pathway are shown in Figure 7.10.³⁸ The geometric parameters of ArNH_2^{2+} and transition state 2 are given in Table 7.9. As can be seen in Figure 7.10, the neutral loss pathway is also consistent with the observed experimental collision energy dependencies of the formation of the ArNH^+ and ArN^+ ions. Assuming again 0 eV collision energy, the reactants will always have sufficient energy to form ArNH^+ , because the amount of internal energy of the ArNH_2^{2+} ion lost to the H atom in the neutral loss step should be small, less than 1 eV. However, the kinetic energy release of the charge separation of ArNH_2^{2+} to ArNH^+ and H^+ will reduce the internal energy of ArNH^+ to approximately -6 to -8 eV (in Figure 7.10). As described above, in this situation again the probability of the ArNH^+ ion having enough internal energy to fragment to ArN^+ and H will increase

with increasing collision energy. This would also result in the experimentally observed increase in the ArN^+ ion yield with a corresponding decrease in the ArNH^+ ion yield with increasing collision energy. In trying to decide which pathway is operating to form ArNH^+ , we expect the pathway in which charge separation occurs first to be kinetically favored, as its rate-limiting transition state lies 2.86 eV lower in energy than that of the neutral loss pathway. In addition, we would expect a small dication such as ArNH_3^{2+} to favour decay via initial charge separation to achieve the 5.24 eV stabilization of the $\text{ArNH}_2^+ + \text{H}^+$ state relative to the $\text{ArNH}_2^{2+} + \text{H}$ state. Indeed, the vast majority of dications derived from small molecules predominantly decay via charge separation rather than neutral loss.^{33,34,43,44} Pathways such as the one shown in Figure 7.10, in which neutral loss occurs in the first step, may be of importance in larger systems where there is greater stabilization of the dipositive charge.

7.4 Conclusions

Crossed-beam collision experiments were performed between Ar^{2+} and NH_3 . Electron transfer reactivity has been rationalized using the Landau-Zener reaction window algorithm. A previously unobserved bond-forming reaction channel, which leads to the formation of the molecular ions ArNH^+ and ArN^+ , was detected. We believe this to be the first report of the formation of a triatomic molecular ion following a bond-forming reaction between a rare gas dication and a neutral. The product ion intensity $I[\text{ArNH}^+]$ was found to decrease with increasing collision energy, with a corresponding increase in the $I[\text{ArN}^+]$ product ion intensity, indicating that ArN^+ is formed by the dissociation of ArNH^+ . The potential energy surface of the reaction, calculated quantum chemically, is found to be in agreement with the

sequential mechanism suggested by the experimental results. These calculations reveal a reaction mechanism in which an ArNH_3^{2+} complex is formed, and then loses a proton followed by two H atoms in three endothermic steps. An alternative mechanism in which the proton loss occurs following an initial H atom loss was also determined. It is expected that the pathway in which charge separation occurs first will be favored, because 2.86 eV less energy is required to overcome the rate-limiting transition state relative to H atom loss.

Using our experimental apparatus it is difficult to determine integral reaction cross sections for ions derived from the neutral as they are backward scattered in both the laboratory frame and the centre of mass frame and so are travelling much slower in the laboratory frame.

7.5 References

- 1 E. Y. Kamber, D. Mathur and J. B. Hasted, *J. Phys. B-Atom. Molec. Opt. Phys.* **15** (1982) 263-273
- 2 E. Y. Kamber, D. Mathur and J. B. Hasted, *J. Phys. B-Atom. Molec. Opt. Phys.* **15** (1982) 2051-2059
- 3 K. B. McAfee and R. S. Hozack, *Phys. Rev. A.* **32** (1985) 810-814
- 4 B. Hird and S. P. Ali, *J. Phys. B-Atom. Molec. Opt. Phys.* **14** (1981) 267-280
- 5 R. Tonkyn and J. C. Weisshaar, *J. Am. Chem. Soc.* **108** (1986) 7128-7130
- 6 A. Ulrich, R. Gernhauser, W. Krotz, J. Wieser and D. E. Murnick, *Phys. Rev. A.* **50** (1994) 1931-1934
- 7 D. Burns, W. R. Thompson, J. B. Greenwood, R. W. McCullough, J. Geddes and H. B. Gilbody, *J. Phys. B-Atom. Molec. Opt. Phys.* **30** (1997) 4559-4568
- 8 V. H. S. Kwong and Z. Fang, *Phys. Rev. Lett.* **71** (1993) 4127-4129
- 9 Z. Fang and V. H. S. Kwong, *Phys. Rev. A.* **55** (1997) 55
- 10 L. Avaldi, G. Dawber, N. Gulley, H. Rojas, G. C. King, R. Hall, M. Stuhec and M. Zitnik, *J. Phys. B-Atom. Molec. Opt. Phys.* **30** (1997) 5197-5212
- 11 L. S. Yang, D. A. Church, S. G. Tu and J. Jin, *Phys. Rev. A.* **50** (1994) 177-185
- 12 E. Y. Kamber, E. J. Quintana and E. Pollack, *J. Phys. B-Atom. Molec. Opt. Phys.* **26** (1993) 113-120
- 13 B. Hird and S. P. Ali, *J. Phys. B-Atom. Molec. Phys.* **14** (1981) 267-280
- 14 P. Tosi, W. Y. Lu, R. Correale and D. Bassi, *Chem. Phys. Lett.* **310** (1999) 180-182
- 15 R. I. Hall, K. Ellis, A. McConkey, G. Dawber, L. Avaldi, M. A. Macdonald and G. C. King, *J. Phys. B-Atom. Molec. Opt. Phys.* **25** (1992) 377-388
- 16 E. Eremina, X. Liu, H. Rottke, W. Sandner, A. Dreischuh, F. Lindner, F. Grasbon, G. G. Paulus, H. Walther, R. Moshhammer, B. Feuerstein and J. Ullrich, *J. Phys. B-Atom. Molec. Opt. Phys.* **36** (2003) 3269-3280
- 17 Y. Morioka, H. Masuda, Y. Lu, K. Tanaka and T. Hayaishi, *J. Phys. B-Atom. Molec. Opt. Phys.* **25** (1992) 5343-5352
- 18 R. Rejoub, B. G. Lindsay and R. F. Stebbings, *Phys. Rev. A.* **65** (2002) Art. 042713

- 19 S. N. Chatterjee and B. N. Roy, *J. Phys. B-Atom. Molec. Opt. Phys.* **20** (1987) 2291-2297
- 20 D. Ascenzi, P. Franceschi, P. Tosi, D. Bassi, M. Kaczorowska and J. N. Harvey, *J. Chem. Phys.* **118** (2003) 2159-2163
- 21 D. Kearney and S. D. Price, *Phys. Chem. Chem. Phys.* **5** (2003) 1575-1583
- 22 N. Tafadar, N. Kaltsoyannis and S. D. Price, *Int J. Mass Spectrom.* **192** (1999) 205-214
- 23 J. H. D. Eland, *Chem. Phys.* **11** (1975) 41-47
- 24 J. H. D. Eland, *Int. J. Mass Spectrom. Ion Phys.* **31** (1979) 161-173
- 25 Y. Song, X. M. Qian, K. C. Lau and C. Y. Ng, *J. Chem. Phys.* **115** (2001) 2582
- 26 D. Evardsson, P. Baltzer, L. Karlsson, B. Wannberg, D. M. P. Holland, D. A. Shaw and E. E. Rennie, *J. Phys. B-Atom. Molec. Opt. Phys.* **32** (1999) 2583-2609
- 27 S. G. Lias, J. E. Bartmess, J. F. Liebman, J. L. Holmes, R. D. Levin and W. G. Mallard, *J. Phys. Chem. Ref. Data.* **17 S1** (1988) 1-861
- 28 S. G. Lias, R. D. Levin and S. A. Kafafi, *NIST Chemistry WebBook, NIST Standard Reference Database Number 69* (<http://webbook.nist.gov>), (1998)
- 29 J. H. D. Eland and J. Berkowitz, *J. Chem. Phys.* **67** (1977) 2782
- 30 A. A. Viggiano, F. C. Fehsenfeld, H. Villinger, E. Alge and W. Lindinger, *Int. J. Mass Spectrom. Ion. Proc.* **39** (1981) 1
- 31 B. A. Huber and H. J. Kahlert, *J. Phys. B-Atom. Mol. Phys.* **17** (1984) L69
- 32 A. Brazuk and H. Winter, *J. Phys. B: At. Mol. Phys.* **15** (1982) 2233
- 33 L. Mrazek, J. Zabka, Z. Dolejsek, J. Hrusak and Z. Herman, *J. Phys. Chem. A.* **104** (2000) 7294-7303
- 34 Z. Herman, J. Zabka, Z. Dolejsek and M. Farnik, *Int. J. Mass Spectrom.* **192** (1999) 191-203
- 35 Z. Herman, P. Jonathan, A. G. Brenton and J. H. Beynon, *Chem. Phys. Lett.* **141** (1987) 433-442
- 36 Z. Herman, *Int. Rev. Phys. Chem.* **15** (1996) 299-324
- 37 K. A. Newson and S. D. Price, *Chem. Phys. Lett.* **269** (1997) 93-98

- 38 N. Lambert, D. Kearney, N. Kaltsoyannis and S. D. Price, *J. Am. Chem. Soc.* **126** (2004) 3658-3663
- 39 Z. Dolejšek, M. Farnik and Z. Herman, *Chem. Phys. Lett.* **235** (1995) 99-104
- 40 K. M. Ervin and P. B. Armentrout, *J. Chem. Phys.* **86** (1987) 6240-6250
- 41 K. M. Ervin and P. B. Armentrout, *J. Chem. Phys.* **90** (1989) 118-126
- 42 K. M. Ervin and P. B. Armentrout, *J. Chem. Phys.* **84** (1986) 6750-6760
- 43 M. Larsson, *Com. At. Mol. Phys.* **29** (1993) 39
- 44 D. M. Curtis and J. H. D. Eland, *Int. J. Mass Spectrom. Ion Processes.* **63** (1985) 241-264

Appendix.

Evaluation of an ion's flight time in a two field mass spectrometer¹

A time of flight mass spectrometer (TOFMS) is able to determine the mass to charge ration (m/z) of an ion by measuring the time taken to travel a known distance, after having been accelerated by an electric field.

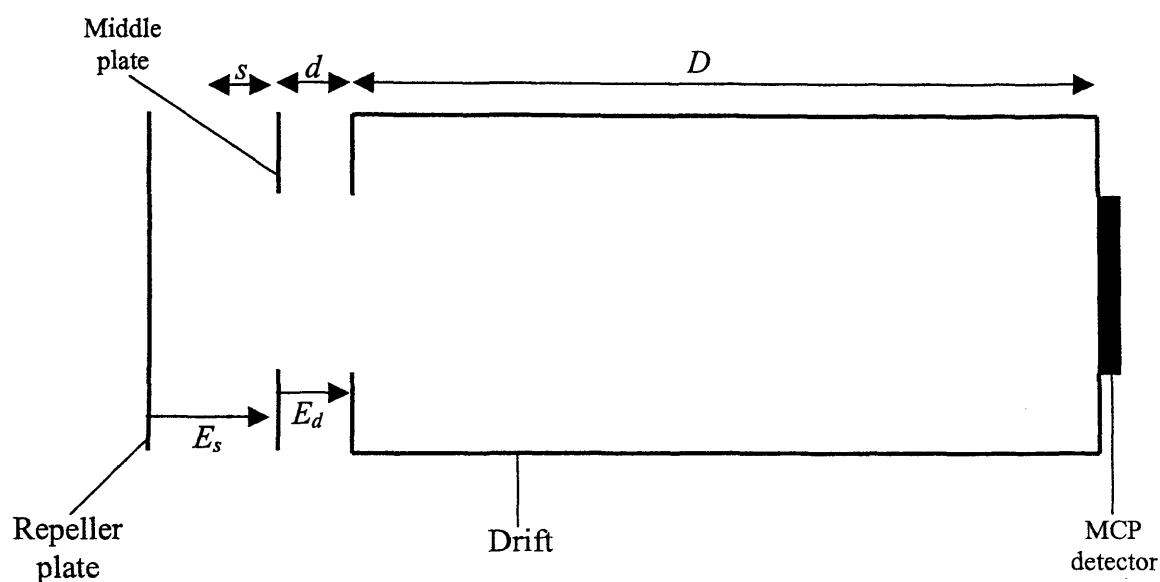


Figure A.1. A schematic diagram of the time of flight mass spectrometer used for the experiments described in this thesis.

This appendix will show that the flight time t of an ion of mass m through a known distance, is given by

$$t = k\sqrt{m} + c \quad (\text{A.1})$$

where k and c are constants relating to the dimensions of the TOFMS and the electronic timing

Figure A.1 shows a schematic representation of the mass spectrometer used for the experiments described in this thesis.

The energy U gained by an ion of charge q as it moves through an electric field E over a distance s is given by

$$U = qsE \quad (\text{A.2})$$

From Figure A.1, the final energy gained by an ion in the spectrometer is

$$U = U_0qsE_s + qdE_d \quad (\text{A.3})$$

where U_0 is the ions initial energy. The time of flight of an ion is the sum of the times taken to travel the distances s , d and D

$$t = t_s + t_d + t_D \quad (\text{A.4})$$

t_s , the time taken to travel from the ionisation point to the middle plate is given by

$$t_s = \frac{v_s - v_0}{a} \quad (\text{A.5})$$

where v_0 is the initial velocity of the ion and a is the acceleration experienced by the ion in the electric field E_s . v_s is the velocity of the ion after being accelerated through a distance s and is given by

$$v_s = v_0^2 + 2as \quad (\text{A.6})$$

Combining equations A.5 and A.6 gives

$$t_s = \frac{\sqrt{v^2 + 2as} \pm v_0}{a} \quad (\text{A.7})$$

The $\pm v_0$ term arises as a result of the fact that some ions will be formed with initial velocities towards the detector (+) and some will be formed with initial velocities moving away from the detector (-).

An ion's initial kinetic energy is given by

$$v_0 = \left(\frac{2U_0}{m} \right) \quad (\text{A.8})$$

Substituting equation A.8 into equation A.7 gives

$$t_s = \left[\left(\frac{2U_0}{m} + \frac{2qE_s}{m} \right)^{1/2} \pm \left(\frac{2U_0}{m} \right)^{1/2} \right] \frac{1}{a} \quad (\text{A.9})$$

An ion's acceleration may be expressed in terms of its mass m , its charge q and the applied electric field E

$$F = ma \quad (\text{A.10})$$

and

$$F = qe \quad (\text{A.11})$$

therefore

$$a = \frac{qE}{m} \quad (\text{A.12})$$

Combining equations A.9 and A.12 gives

$$t_s = \left[\left(\frac{2U_0}{m} + \frac{2qE_s}{m} \right)^{1/2} \pm \left(\frac{2U_0}{m} \right)^{1/2} \right] \frac{m}{qE_s} \quad (\text{A.13})$$

This simplifies to

$$t_s = \frac{(2m)^{1/2}}{qE_s} \left[(U_0 + qsE_s)^{1/2} \pm U_0^{1/2} \right] \quad (\text{A.14})$$

The time t_d for an ion to travel the distance d is

$$t_d = \frac{v_d - v_s}{a} \quad (\text{A.15})$$

where v_d is the velocity of the ion after being accelerated through a distance d and a is the acceleration of the ion as it passes through the electric field E_d . v_d is given by

$$v_d^2 = v_s^2 + 2ad = v_s^2 + \frac{2qdE_d}{m} \quad (\text{A.16})$$

By substituting equations A.6 and A.16 into equation A.16, we get

$$t_d = \left[v_s^2 + \frac{2qdE_d}{m} \right]^{1/2} \frac{m}{qE_d} - \left[v_0^2 + \frac{2qsE_s}{m} \right]^{1/2} \frac{m}{qE_d} \quad (\text{A.17})$$

Again, substituting equations A.6 and A.8 gives

$$t_d = \frac{(2m)^{1/2}}{qE_d} [U_0 + qsE_s + qdE_d]^{1/2} - \frac{(2m)^{1/2}}{qE_d} [U_0 + qsE_s]^{1/2} \quad (\text{A.18})$$

Simplifying

$$t_d = \frac{(2m)^{1/2}}{qE_d} \left[U^{1/2} - (U_0 + qsE_s)^{1/2} \right] \quad (\text{A.19})$$

The drift tube has no accelerating potential so the ion will travel along, in this region, at constant velocity v_d . The time taken to travel the length of the drift tube t_D is

$$t_D = \frac{D}{v_d} = \frac{D}{\left[v_s^2 + \frac{2qdE_d}{m} \right]^{1/2}} \quad (\text{A.20})$$

Substituting equations A.6 and A.8 into equation A.20 gives

$$t_D = \frac{D}{\left[\left(\frac{2}{m} \right) U_0 + qsE_s + qdE_d \right]^{1/2}} \quad (\text{A.21})$$

which may be simplified to

$$t_D = \frac{(2m)^{1/2} D}{2U^{1/2}} \quad (\text{A.22})$$

Therefore, the total flight time t , in seconds, of an ion is given by

$$t = (2m)^{1/2} \left[\frac{\left[(U_0 + qsE_s)^{1/2} \pm U_0^{1/2} \right]}{qE_s} + \frac{\left[U^{1/2} - (U_0 + qsE_s)^{1/2} \right]}{qE_d} + \frac{D}{2U^{1/2}} \right] \quad (\text{A.23})$$

It is clear from equation A.23, that the time of flight t of an ion is proportional to \sqrt{m} .

As the electric fields, dimensions and timing electronics of the TOFMS are constant, equation A.23 may be abbreviated to

$$t = k\sqrt{m} + c \quad (\text{A.1})$$

The constants k and c may be evaluated by solving two equations, relating to two ions of different masses and flight times, simultaneously.

References

- 1 W. C. Wiley and I. H. McLaren, *Rev. Sci. Inst.* **26** (1955) 1150

Appendix.

Evaluation of an ion's flight time in a two field mass spectrometer¹

A time of flight mass spectrometer (TOFMS) is able to determine the mass to charge ration (m/z) of an ion by measuring the time taken to travel a known distance, after having been accelerated by an electric field.

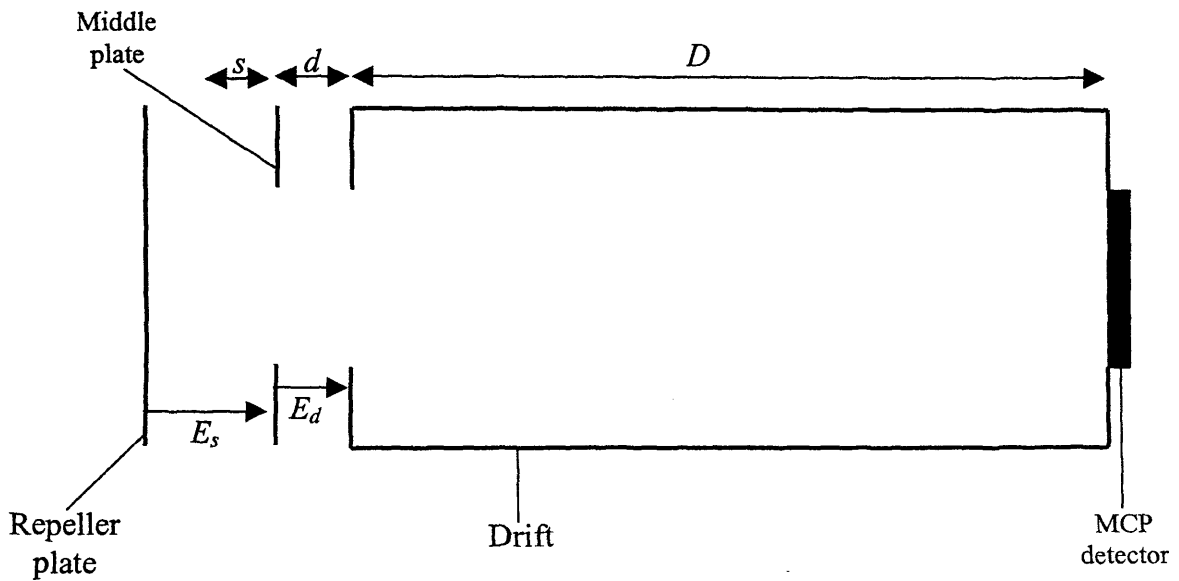


Figure A.1. A schematic diagram of the time of flight mass spectrometer used for the experiments described in this thesis.

This appendix will show that the flight time t of an ion of mass m through a known distance, is given by

$$t = k\sqrt{m} + c \quad (\text{A.1})$$

where k and c are constants relating to the dimensions of the TOFMS and the electronic timing

Figure A.1 shows a schematic representation of the mass spectrometer used for the experiments described in this thesis.

The energy U gained by an ion of charge q as it moves through an electric field E over a distance s is given by

$$U = qsE \quad (\text{A.2})$$

From Figure A.1, the final energy gained by an ion in the spectrometer is

$$U = U_0 + qsE_s + qdE_d \quad (\text{A.3})$$

where U_0 is the ions initial energy. The time of flight of an ion is the sum of the times taken to travel the distances s , d and D

$$t = t_s + t_d + t_D \quad (\text{A.4})$$

t_s , the time taken to travel from the ionisation point to the middle plate is given by

$$t_s = \frac{v_s - v_0}{a} \quad (\text{A.5})$$

where v_0 is the initial velocity of the ion and a is the acceleration experienced by the ion in the electric field E_s . v_s is the velocity of the ion after being accelerated through a distance s and is given by

$$v_s^2 = v_0^2 + 2as \quad (\text{A.6})$$

Combining equations A.5 and A.6 gives

$$t_s = \frac{\sqrt{v_0^2 + 2as} \pm v_0}{a} \quad (\text{A.7})$$

The $\pm v_0$ term arises as a result of the fact that some ions will be formed with initial velocities towards the detector (+) and some will be formed with initial velocities moving away from the detector (-).

An ion's initial kinetic energy is given by

$$v_0 = \left(\frac{2U_0}{m} \right)^{1/2} \quad (\text{A.8})$$

Substituting equation A.8 into equation A.7 gives

$$t_s = \left[\left(\frac{2U_0}{m} + \frac{2qE_s s}{m} \right)^{1/2} \pm \left(\frac{2U_0}{m} \right)^{1/2} \right] \frac{1}{a} \quad (\text{A.9})$$

An ion's acceleration may be expressed in terms of its mass m , its charge q and the applied electric field E

$$F = ma \quad (\text{A.10})$$

and

$$F = qe \quad (\text{A.11})$$

therefore

$$a = \frac{qE}{m} \quad (\text{A.12})$$

Combining equations A.9 and A.12 gives

$$t_s = \left[\left(\frac{2U_0}{m} + \frac{2qE_s}{m} \right)^{1/2} \pm \left(\frac{2U_0}{m} \right)^{1/2} \right] \frac{m}{qE_s} \quad (\text{A.13})$$

This simplifies to

$$t_s = \frac{(2m)^{1/2}}{qE_s} \left[(U_0 + qsE_s)^{1/2} \pm U_0^{1/2} \right] \quad (\text{A.14})$$

The time t_d for an ion to travel the distance d is

$$t_d = \frac{v_d - v_s}{a} \quad (\text{A.15})$$

where v_d is the velocity of the ion after being accelerated through a distance d and a is the acceleration of the ion as it passes through the electric field E_d . v_d is given by

$$v_d^2 = v_s^2 + 2ad = v_s^2 + \frac{2qdE_d}{m} \quad (\text{A.16})$$

By substituting equations A.6 and A.16 into equation A.16, we get

$$t_d = \left[v_s^2 + \frac{2qdE_d}{m} \right]^{1/2} \frac{m}{qE_d} - \left[v_0^2 + \frac{2qsE_s}{m} \right]^{1/2} \frac{m}{qE_d} \quad (\text{A.17})$$

Again, substituting equations A.6 and A.8 gives

$$t_d = \frac{(2m)^{1/2}}{qE_d} [U_0 + qsE_s + qdE_d]^{1/2} - \frac{(2m)^{1/2}}{qE_d} [U_0 + qsE_s]^{1/2} \quad (\text{A.18})$$

Simplifying

$$t_d = \frac{(2m)^{1/2}}{qE_d} \left[U^{1/2} - (U_0 + qsE_s)^{1/2} \right] \quad (\text{A.19})$$

The drift tube has no accelerating potential so the ion will travel along, in this region, at constant velocity v_d . The time taken to travel the length of the drift tube t_D is

$$t_D = \frac{D}{v_d} = \frac{D}{\left[v_s^2 + \frac{2qdE_d}{m} \right]^{1/2}} \quad (\text{A.20})$$

Substituting equations A.6 and A.8 into equation A.20 gives

$$t_D = \frac{D}{\left[\left(\frac{2}{m} \right) U_0 + qsE_s + qdE_d \right]^{1/2}} \quad (\text{A.21})$$

which may be simplified to

$$t_D = \frac{(2m)^{1/2} D}{2U^{1/2}} \quad (\text{A.22})$$

Therefore, the total flight time t , in seconds, of an ion is given by

$$t = (2m)^{1/2} \left[\frac{[(U_0 + qsE_s)^{1/2} \pm U_0^{1/2}]}{qE_s} + \frac{[U^{1/2} - (U_0 + qsE_s)^{1/2}]}{qE_d} + \frac{D}{2U^{1/2}} \right] \quad (\text{A.23})$$

It is clear from equation A.23, that the time of flight t of an ion is proportional to \sqrt{m} .

As the electric fields, dimensions and timing electronics of the TOFMS are constant, equation A.23 may be abbreviated to

$$t = k\sqrt{m} + c \quad (\text{A.1})$$

The constants k and c may be evaluated by solving two equations, relating to two ions of different masses and flight times, simultaneously.

References

- 1 W. C. Wiley and I. H. McLaren, *Rev. Sci. Inst.* **26** (1955) 1150